Pinched Flow Fractionation – Teknologi and Applikation

Vig, Asger Laurberg

Publication date:
2010

Document Version
Publisher's PDF, also known as Version of record

DTU Nanotech
Department of Micro- and Nanotechnology

Ph.D. Thesis

Pinched Flow Fractionation - Technology and Application

Asger Laurberg Vig

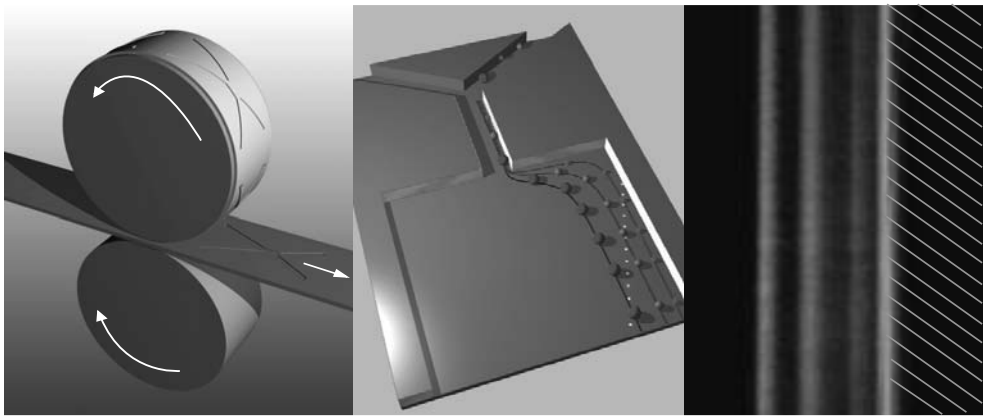

Supervisor: Anders Kristensen

Department of Micro- and Nanotechnology
Technical University of Denmark

February 9, 2010

Abstract

This Ph.D. thesis considers the three major development aspects for lab-on-a-chip (LOC) systems: 1) fabrication, 2) sample treatment and handling and 3) detection. Of particular interest is a microfluidic size separation technique called pinched flow fractionation (PFF). Pinched flow fractionation is a simple but effective approach for separation analysis. In addition, PFF is a continuous process that can be readily combined with a multitude of other continuous processes available into full LOC systems.

The PFF devices are, in most cases, imprinted by nanoimprint lithography into a cyclo olifin copolymer (COC) called Topas®, which leads to cheap fabrication and easy integration with other wafer scale LOC components. An extreme high-volume fabrication technique relying on roll-to-roll (rtr) methods is developed and used to fabricate 360 functional PFF devices per hour at a unit cost of 0.5 Euro.

Micrometer scale PFF devices are characterized theoretically and experimentally by separating eight different sized polystyrene microspheres ranging from 0.26 µm to 2.5 µm in radius. The separation resolution of the samples with a standard deviation of 5 % in size is measured as low as 100 nm. Pinched flow fractionation is also applied for genotyping of a human DNA sample. The separation in PFF is additionally enhanced by a small channel modification that is still compatible with the rtr fabrication technique. An enhancement in separation of up to 70 % and in resolution of up to 25 % is measured using the same type of sample as in the basic PFF characterization but with the small channel modification. Further, a nanometer-scale PFF device is designed to achieve LOC-based single protein separation. This device is characterized via polystyrene nanospheres with radii of 22 nm and 50 mn, and the channel surfaces are functionalized to prevent protein immobilization.

Integration of an optofluidic microscope (OFM) in the PFF layout is demonstrated for 3 dimensional optical detection of separated microspheres. The resolution of the detection is $\leq$0.92 µm in width and 1.4 µm in height. In addition, this integrated device is also used for particle velocimetry with a resolution of 4 % of the measured velocity.

A windowless microfluidic platform based on capillary burst valves for time-resolved high intensity x-ray studies is also developed. Sample refreshment rates up to 54 kHz is measured and later doubled by a tapered device design. The functionality of the platform is demonstrated with microsphere suspensions, protein samples and a photoactive platinum compound. In addition, the system is tested successfully under realistic operation conditions at the time-resolved x-ray beamline ID09b at the synchrotron facility at ESRF in Grenoble. Pinched flow fractionation has not yet been integrated into the platform for separation prior to the x-ray measurements, but is an obvious extension of the work presented in the thesis.

Dansk Resumé

Denne Ph.D. afhandling omhandler de tre udviklingsaspekter inden for lab-on-a-chip (LOC) systemer: 1) fabrikation, 2) transport samt behandling af prøve og 3) detektion ved brug af en mikrofluid sorteringsteknik ved navn pinched flow fraktionation (PFF) som modelsystem. Sortering via PFF er en kontinuerlig process, som derfor kan kombineres med andre kontinuerlige processer i et samlet LOC analyse system. Derudover kan PFF også bruges selvstændigt til separation og analyse.

Pinched flow fractionation komponenter er i de fleste tilfælde i denne afhandling fabrikeret ved brug af nanoimprint lithografi i overfladen af en cyclo olefin copolymer ved navn Topas®. Derved kan disse komponenter laves billigt og nemt integreres med andre wafer-skala komponenter. Desuden er en høj-volumen fabrikationsteknik baseret på rulle-til-rulle (rtr) metoder blevet udviklet og brugt til at fabrikere 360 funktionelle PFF komponenter i timen til en enhedspris på 0,5 Euro.

Mikrometer skala PFF komponenter er blevet karakteriseret teoretisk og eksperimentielt, sidstnævnte med 8 forskellige størrelser polystyren mikrokugler med en radius fra 0,26 µm til 2,5 µm. Sorteringsopløsningen for mikrokugleprøver med en standardafvigelse på 5 % af størrelsen blev målt ned til 100 nm. Pinched flow fractionation er blevet demonstreret til at gen-bestemme menneskelige DNA prøver. Separationen i PFF blev desuden forstørret ved en mindre modifikation af komponentlayoutet, hvilken stadig er kompatibel med rtr fabrikation. En forstørrelse af separationen op til 70 % og af opløsningen på op til 25 % blev målt ved brug af samme mikrokugleprøver som i de basale PFF målinger. En nanoskala PFF komponent blev også designet for at opnå separation af enkelte proteiner. Denne komponent er blevet karakteriseret med polystyrene nanokugler med en radius på 22 nm og 50 nm, og overfladerne i komponenten er blevet funktionaliseret for at undgå immobilisering af proteiner.

Et optofluidic microscope (OFM) er blevet integreret i PFF komponenten og brugt til demonstration af 3 dimensional optisk positionering af separeret mikrokugler. Detektionsopløsningen i bredden af kanalen blev målt til $\leq$0.92 µm og 1,4 µm i højden. Derudover er komponenten også blevet brugt til hastighedsbestemmelse af partikler med en opløsning på 4 % af den målte hastighed.

En vinduefrit mikrofluid platform baseret på capillary burst valves til tid-opløste studier med høj-intensitet røntgen stråler er blevet udviklet. Prøvefornyelsesrater på op til 54 kHz er blevet målt og fordoblet via et indsnævret komponentdesign. Funktionaliteten af den mikrofluide platform er demonstreret med suspensioner af polystyren mikrokugler, protein prøver og en photoaktiv platin-holdig forbindelse. Derudover er platformen testet under realistiske operationsbetingelser ved den tidsopløst røntgenstrålelinje ID09b ved synkrotronen på ESRF i Grenoble. Integrering af PFF i platformen er en indlysende udvidelse af det arbejde, som er præsenteret i afhandlingen.

Preface

This thesis is written as a partial fulfillment of the requirements to obtain the Philosophiae Doctor (Ph.D.) degree at the Technical University of Denmark (DTU). The work has been carried out at the Department of Micro and Nanotechnology (DTU Nanotech) in the period from the 15th of December 2006 to the 9th of February 2010. The project was financed by a DTU stipend and was a part of the Optofluidic group in the Nanoscience engineering division at DTU Nanotech.

The project was supervised by professor Anders Kristensen, whom I gratefully acknowledge for his enthusiasm and energetic guidance. Anders always finds time for a discussion and I have learned a lot concerning good leadership and about the importance of networking. In addition, Anders is a very pleasant person to work with and gladly combines physics with social events and private conversations. I fully thank him for his supervision.

Since I joined the Optofluidic group, Anders has gained a professorship and the group has doubled in size with many new international students and researchers. I have enjoyed the dynamic and friendly atmosphere in the group. I thank all past and present group members for being good friends and colleagues. Especially, I would like to thank Rodolphe Marie and Fredrik Person for good collaboration and many fruitful discussions.

I would also like to thank several other people from DTU Nanotech from whom I have gained a lot of expertice. Fridolin Okkels for invaluable help with modeling in COMSOL Multiphysics, Henrik Flyvbjerg for theoretical discussions and Lena Poulsen and Martin Dufva for help with handling of biological samples such as human DNA and proteins.

Throughout a subproject concerning high volume fabrication of polymer-based lab-on-a-chip devices by roll-to-roll methods, I have collaborated with Tapio Mäkelä, VTT Espoo, and Vito Lambertini, Centro Ricerche Fiat S.C.p.A. Both Tapio and Vito have been very flexible and fast working and I thank them for their collaboration. Especially, I would like to thank Tapio for his hospitality during my stay at Åbo Akademi and VTT Espoo.

At the annual meeting of the danish physical society 2008, I meet Kristoffer Haldrup, and a very good collaboration started, concerning development of a windowless microfluidic platform for time-resolved high intensity x-ray measurements. In the spring of 2009 Kristoffer Haldrup and Martin Meedom Nielsen introduced me to the synchrotron facility at ESRF in Grenoble, where the microfluidic platform was tested. I thank both Kristoffer and Martin for their collaboration.

Finally, I thank my wife Heidi for her great support and my wonderful daughter Lærke, who was born in December 2009 and motivated me to write the thesis in good time.

Asger Laurberg Vig
9 February 2010.

Contents

List of Figures

List of Tables

Abbreviations and Symbols

Abbreviation	Description
AR	aspect ratio
aRNA	amplified ribonucleic acid
CA	cellulose acetate
CBV	capillary burst valve
CCD	charge coupled device
COC	cyclic-olefin copolymer
DNA	deoxyribonucleic acid
DRIE	deep reactive ion etching
EBL	electron beam lithography
EMCCD	electron multiplying charge coupled device
EPFF	enhanced pinched flow fractionation
HBB	hemoglobin beta
LOC	lab-on-a-chip
μTAS	micro total analysis systems
NA	numerical aperture
NIL	nanoimprint lithography
NS	Navier-Stokes equation
OFM	optofluidic microscopy
PCR	polymerase chain reaction
PFF	pinched flow fractionation
PIV	particle image velocimetry
PLL-g-PEG	poly(L-lysine)-g-poly(ethylene glycol)
PMMA	poly(methyl methacrylate)
POC	point of care
PS	polystyrene
PtPOP	Tetrakis-μ-pyrophosphitodiplatinate(II)
RG	reverse gravure
RNA	ribonucleic acid
rtr	roll-to-roll
SDS	sodium dodecyl sulfate
SEM	scanning electron microscopy
SEF	Separation enhancement factor
SNP	single nucleotide polymorphisms
SSC	sodium citrate
TEC	temperature expansion coefficient
UV	ultraviolet
XFEL	x-ray free electron laser

Symbols	Description	Unit
$\mathbf{r}$	Position vector	m
x, y, z	Position coordinates	m
w	width	m
H	Hight	m
h	Thickness	m
L	Length	m
r	Radius	m
A	Area	m^2
t	Time	s
υ	Velocity	m/s
ρ	Density	kg/m^3
$\mathbf{F}$	Force	N
$\mathbf{f}$	Force per volume	N/m^3
$\mathbf{f}_l$	Non dimensional lift coefficient	
p	Pressure	Pa
n	Refractive index	
n	Number count	
R	Resolution	m
R	Hydraulic resistance	Pa s/m^3
σ	Standard deviation	m
D	Diffusion coefficient	m^2/s
k_B	Boltzmann constant	1.38 10^{-23}J/°K
T	Temperature	°K
η	Viscosity	Pa s
$\dot{\gamma}$	Shear rate	s^{-1}
M	Molecular weight	kg/mol
γ	Surface tension	J/m^2
Q	Flow rate	m^3/s

Symbols in Tables

Symbols	Description	Unit	Table
r or $\langle r \rangle$	Radius	m	2.1
$\sigma_{\mathbf{r}}$ or $\sigma(r)$	Standard deviation in radius	m	2.2
w	Width of a microchannel	m	2.1
$\mathbf{y'}$	Center distance of the microspheres from the channel wall in the broadening segment in pinched flow fractionation devices	m	2.3
$\sigma_{\mathbf{y'}}(\sigma_{\mathbf{r}})$	Calculated standard deviation of $\mathbf{y'}$ resulting from $\sigma_{\mathbf{r}}$	m	2.2
$\sigma_{\mathbf{diff}}$	Calculated diffusion of separated microspheres in pinched flow fractionation	m	2.2
$\delta \mathbf{r_{d,h}}$	Calculated upper detection limit excluding diffusion	m	2.2
$\sigma_{\mathbf{y',exp}}$	Experimentally found standard deviation of $\mathbf{y'}$	m	2.3
$\delta \mathbf{r_{d,exp}}$	Measured detection resolution in r	m	2.3
$\delta \mathbf{r_{d,cal}}$	Calculated detection resolution in r	m	2.3
$\mathbf{y'_{EPFF}}$	Center distance of the microspheres from the channel wall in the broadening segment in pinched flow fractionation devices	m	4.1
$\sigma_{\mathbf{y'_{EPFF}}}$	Experimentally found standard deviation of $\mathbf{y'_{EPFF}}$	m	4.1
$\mathbf{F}_l$	Lift force	N	2.1
$\mathbf{f}_l$	Non dimensional lift coefficient		2.1
$\mathbf{s}_{lift}$	Migration of microspheres in the pinch segment caused by $\mathbf{F}_l$	m	2.1
$\mathbf{\Delta y'}$	Change in $\mathbf{y'}$ caused by lift forces	m	2.1

Chapter 1

Introduction

Imagine portable, cheap and easy-to-use analysis systems that can be used by medical doctors in remote areas to test for given diseases, or for research studies of the behavior of rare sample e.g. structural changes in DNA and proteins. These motivations drive the development of micro total analysis systems (μTAS), also denoted Lab-On-a-Chip (LOC) systems. The potential impact, in terms of technology perspectives and scientific research, has made these systems one of the fastest growing interdisciplinary research fields during the last several decades.

In the beginning of the 1980s, the concept of an automated total chemical analysis system (TAS) including operations in analytical chemistry, such as transport of sample, chemical reactions, separation and detection, was introduced [1]. However, the idea did not get much attention until the early 1990s, when the concept of miniaturized TAS (μTAS) was suggested by Manz and coworkers [2, 3]. The basic idea is similar to that of TAS but by miniaturization, pretreatment of sample is brought closer to the detection area, and several advantages follow:

- *Consumption of sample* - The consumption of the sample is significantly reduced because of the smaller dimensions. This is in many biological and chemical cases important because of rare and/or expensive samples. One example is blood analysis from premature children. They only have a total blood volume in the order of a few hundred mL. Blood samples must not exceed 2 % of this volume and the maximum volume is therefore on the order of 2-4 mL.

- *Price* - μTAS can be mass produced by tools from polymer industries or the integrated circuit industry, bringing down the unit cost. In addition, expensive laboratory equipment can be integrated in the μTAS, resulting in even more cost-efficient systems compared to commercial laboratories. One example is flow cytometry equipment from Luminex [4] e.g. for detection of single nucleotide polymorphisms (SNP). Their systems cost in the range of 120 kEuro, whereas the μTAS system for SNP detection presented in this thesis can be sold, with a profit, for about 10 kEuro — reducing instrument cost by more than a factor 10.

- *Process time* - Sample handling in miniaturized systems results in shorter transport distances - thereby less analysis time. In addition, the smaller dimensions reduce analysis times in diffusion-dependent systems further. One example of a reduction in analysis time is cancer screening. As a tumor evolves, cancer cells

start to circulate in the blood. In an early state these cells are detectable and diagnosis is possible. However, per 5 mL blood there are only 2-3 cancer cells. Current diagnostics in medical laboratories are very time consuming — limiting the possible numbers of diagnoses [5]. The process time in μTAS is lowered, typically by a factor of 10 to 100 [6].

- *Portable* - As the size of μTAS are in the range of cm^2 and have functionalities of bulky equipment integrated, these analysis systems are portable. Combined with low cost, the systems realize point-of-care (POC) analysis.

The ideas of Manz were originally for analytical chemistry but were soon adopted in other scientific disciplines, thereby extending μTAS to the LOC concept and including components beyond those of analytical chemistry. For the remainder of this thesis all miniaturized systems are denoted as LOC. The principle of LOC is to integrate all the functions of a macro-scale test laboratory into a system of a few square centimeters.

1.1 Important aspects in lab on a chip development

With the pioneering paper of Manz et al. approaching its 20th anniversary, the field of LOC is becoming mature, and a large variety of fabrication methods, unit operations (sample transport and treatment), detection methods and applications have been demonstrated. However, the social and commercial impact is still limited. The main criteria that LOC must live up to in terms of commercial interest is low price, short analysis time, reliability and stability. In addition, in the case of existing methods, LOC must be better in at least one of these issues. Presently, the success of LOC largely relies on rapid and cheap prototyping methods but also coherent solutions in which all aspects of LOC development — fabrication, sample transport and treatment as well as detection (illustrated in Fig. 1.1) — are chosen and optimized in accordance with each other.

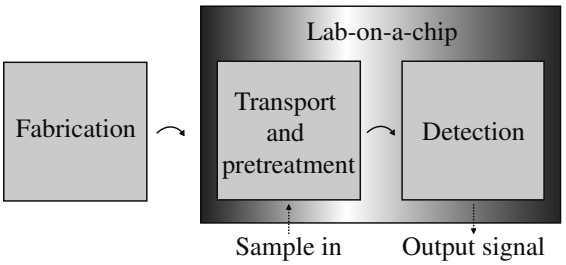

Figure 1.1: Important aspects in development of a lab-on-a-chip.

This thesis represents a technological and application study of the central issues of lab-on-a-chip (LOC) development, as illustrated in Fig. 1.1, using a microfluidic separation technique called pinched flow fractionation as model system. In the following three sections, an introduction to the state-of-the-art literature within each of the three LOC development aspects, with an emphasis on work related to this study, is presented. Each section ends in a short introduction to the approaches chosen in the thesis. The work of this thesis also involve the development of a windowless microfluidic platform

for time-resolved high intensity x-ray studies. Accordingly, a literature survey on this topic is also included. Concluding the introduction, an overall aim and outline of the thesis is presented.

1.2 LOC fabrication methods

In the first years of LOC, most devices were made in silicon, quartz and glass, mainly because the tool box for micro-scale structures available in the semiconductor industry was highly optimized for these materials. In addition, mass production in this industry realized cheap solutions compared to the conventional macro-scale analysis systems. A comprehensive review of planar processing methods for silicon, quartz and glass microfluidic structures is given in [7]. As the LOC community evolved it became clear that most applications demand single-use devices in order to minimize the risk of sample contamination. With single-use devices, the initially used materials and matching fabrication techniques are too expensive for applications such as POC diagnostics. Polymer materials and the matching fabrication processes have proved to be well suited for this challenge. As an example, the total cost of the polymer devices presented in Chap. 3 is 0.5 Euro, whereas the cost of similar devices in silicon is approximately 50 euro for a production of 60 units. In addition, most biological and chemical laboratories use polymer items, such as pipette tips and Eppendorf tubes, so the potential users are familiar with the material and a large variety of surface chemistry solutions have been developed. Consequently, a variety of polymer fabrication methods have been developed the last 10 years, allowing the LOC field to experience a large progress and is also the foundation of a real commercial breakthrough. The existing polymer fabrication methods are introduced shortly in the following text and summarized in Table 1.1. For a comprehensive discussion of the techniques mentioned above the reviews [8, 9, 10] are recommended.

The commercial success of the polymer industry in the macroscopic world, is mainly due to the so called replication techniques, in which the structures of a mold is transferred to a substrate material. Five of these have been adapted for LOC and are listed in the first rows of Table 1.1. The most established and promising candidates of the replication techniques for LOC, commercial-wise, are micro-injection (μ-injection) molding [11, 12, 13, 14, 15], hot embossing [16] and injection compression molding [8, 17]. Injection molding is the most widespread fabrication method for polymers in the macroworld and enables very fast processing. The cycle time of μ-injection molding is typically on the order of seconds to minutes. However, because of expensive machinery and tools, the work within microfluidic structures is still rather limited compared to its success in the macroworld. Due to difficulties in mold filling during fabrication [18], high aspect ratio as well as nanometer sized structures are not trivial to fabricate with this technique. Hot embossing, in nano-scale dimensions denoted nanoimprint, is much more widespread in the LOC community, because of relatively low machine and tool cost. Furthermore, structures down to 5 nm have been demonstrated without any trouble [19]. However, aside from one example of an imprint cycle time of 20 s [20], hot embossing usually has cycles times in the minute to hour range.

Injection compression molding, used for CD and DVD production, is a combination of the basic principles in hot embossing and injection molding, combining the replication accuracy of hot embossing and the high volume fabrication capacity of in-

jection molding. The main disadvantage of compression injection molding is the fixed CD/DVD format of existing machinery. The technique has been used to fabricate centrifugal microfluidic systems with significant success [21].

The two remaining replication techniques are casting [22, 23, 24] and micro-thermoforming (μ-thermoforming) [25, 26]. Casting is a slow process but is very cheap. Furthermore, there is close to no entry expenses and it therefore takes the honor of the still increasing world-wide academic interest in LOC. μ-thermoforming on the other hand, is, as injection molding, a high volume fabrication method but has a poor replication accuracy for high aspect ratios and sharp edges. However, it is suitable for round structuring of pre-structured films.

Process	**Type**	**Materials**	**Fab. vol.**	**Tool cost**	**Res.**	**AR**
Hot embossing/ nanoimprint	Parallel	Termoplastics Thermosets	Med (Cycle time: min)	Low	5 nm	>3
μ-injection molding	Parallel	Termoplastics Thermosets	Med–high (Cycle time: s–min)	High	30 nm	∼1
Injection compression molding	Parallel	Termoplastics Thermosets	Very high (Cycle time: s)	High	25 nm	∼1
μ-thermoforming	Parallel	Termoplastics	Med–high (Cycle time: s–min)	High	150 μm	∼1
Casting	Parallel	Elastomers	Low (Fab time: hours)	Very low	10 nm	>1
Photolithography	Parallel	Photo-definable polymers	Med–high (Fab time: s–min)	High	<1 μm	>18
Laser ablation	Serial	Most polymers	Low	Low	<1 μm	<600

Table 1.1: Existing fabrication process for polymer materials and corresponding details of type, relevant materials, fabrication volume (Fab. vol.), tool cost, resolution (Res.) and aspect ratio (AR). All relevant references are given in the text.

The last two techniques in Table 1.1, photolithography [27, 28, 29] and laser ablation [30, 31, 32, 33], are applicable for photo-definable polymers. Photolithography, usually with SU-8 as the UV-sensitive polymer, has been used since the mid 1990s for microfluidic devices. The resolution of this technique is limited by the wavelength of the exposure light, the sensitivity of the polymer and the polymer thickness (Chap. 5.5.5.3 in [34]). In most photolithography systems ($\lambda = 365\,\text{nm}$) the resolution is approximately 1 μm. This technique gained most attention in the early years of LOC. As cheaper and more flexible alternatives appear, the interest in photolithography is decreasing. However, the technique only requires standard UV-lithography setups, which are available in most cleanrooms and will therefore probably not disappear completely.

Laser ablation is a serial process and therefore not suitable to large scale production. Another issue with laser ablation is the fact that the intense laser beam used to define the structures changes the surface chemistry and leads to variations in the performance of devices. However, laser ablation is the most flexible candidate of the methods stated in Table 1.1 in regards to design flexibility and is capable of extreme high aspect ratios (< 600). Laser ablation is therefore an attractive rapid prototyping method for many research applications.

1.2.1 Roll-to-roll imprinting

An alternative to the existing polymer fabrication methods summarized in Table 1.1 is roll-to-roll (rtr) imprinting. The idea of rtr imprinting is originally adapted from the continuous process used by the newspaper industry in which production volume is extremely high (> 1000 news papers/hour). Holographic printing, e.g. on money bills, is another example. This means that rtr, compared with any of the more established fabrication methods listed in Table 1.1, is a very well qualified candidate for polymer fabrication due to its potential for extreme high production enabled by the continuous process approach. This is why thermal rtr imprinting is chosen as the high-volume fabrication technique in the thesis. The basic thermal rtr system for fabrication of LOC platforms is illustrated in Fig. 1.2. A film of a thermoplastic material is continuously fed in between two rolls, the imprint roll and the backside roll, which are pressed together. In addition, the imprint roll, which has a structured surface or a stamp attached to it is heated up to or above the glass transition temperature of the polymer film. Utilizing this principle a fabrication volume of 360 devices/hour has been demonstrated in this thesis. This is a high production volume as compared to state-of-the-art production volumes by μ-injection molding and hot-embossing of 100-200 devices/hour [12, 20]. This is especially so, as thermal rtr imprinting has the potential for much higher production volumes, by simply up-scaling the research rtr machine used in this study. This setup is described in detail in Chap. 3. In addition, thermal rtr imprinting can be combined with continuous rtr lamination, to seal the imprinted channels, with an insignificant extension of the fabrication time.

Thermal rtr imprint has been utilized for structuring conducting polymers [35] and optical devices [36]. In both cases the structures range in width and length from nanometers up to millimeters, with imprint depths up to 1 μm. In the microfluidic devices of this thesis, the channel structures are usually deeper than 1 μm. Due to recovery of the imprinted structures, which arise from the short imprint time, deep channels represents one of the most challenging aspects of thermal rtr imprint. A few examples of thermal rtr imprinting of micrometer scale structures, which are more than 1 μm deep, have been published. Ishizawa et al. [37] demonstrated in 2008 thermal rtr imprinting of dots with a diameter of 10 μm, a depth of 8 μm and a pitch of 20 μm. In addition, Ng et al. [38] demonstrated in 2009 thermal rtr imprinting of channel structures up to 30 μm in depth and 50 μm to 100 μm in width. Here sealing of the channels was carried out manually and not integrated in the rtr production line.

Thermal rtr imprinting of functional microfluidic devices has not yet been demonstrated. In this thesis the technique is optimized for microfluidic devices and combined with other rtr methods (e.g. sealing of the imprinted channels) for continuous fabrication.

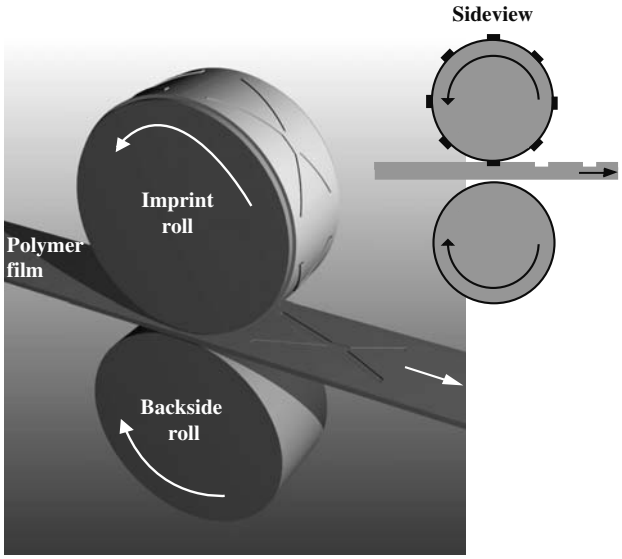

Figure 1.2: The principle of thermal roll-to-roll imprinting. A thermoplastic film is fed between a heated imprint roll with a structured surface and a flat backside roll at room temperature. The two rolls are pressed together during the process, replicating the roll structures in the polymer film.

1.3 Sample transportation and pretreatment

An enormous amount of research work has been invested into developing unit operations for sample transportation and pretreatment prior to detection and analysis. Today, the variety of available operations, spanning micropumping [39, 40], valving [41], mixing [42, 43], metering [44], concentration [45] and separation [46], can be used to solve most tasks in LOC. Separation, playing a central role in many biological and chemical systems, is chosen as the unit LOC operation in the thesis. The following literature survey focuses on this topic.

Fluidic based separation techniques can be divided into two groups: batch separation and continuous separation. In batch separation a small volume (typically sub-nanoliters) is handled at one time and sample particles are separated in the flow direction. Examples are: field flow fractionation (FFF) [47, 48, 49], hydrodynamic chromatography [50] and electrophoresis [51, 52]. These are all established techniques in analytical chemistry and have been demonstrated for various samples such as carbon nanotubes, DNA, proteins and cells. However, these are all relying on stochastic mechanisms, giving an upper limit to the separation velocity, and are therefore relatively slow (separation time: min – hours). Furthermore, their batch operation nature carries challenges when combining them with up- or down-stream continuous flow processes. For LOC separation, continuous separation techniques are in most cases better suited.

In continuous separation, separation typically occurs perpendicular to the flow, and originates from the interaction of a laminar flow and obstacles in a flow channel or from external forces. A review of most of the on-chip continuous separation techniques is

given in [46]. These are divided in two categories: those with external forces and those without external forces. Examples for which an external force is applied include free-flow electrophoresis used for proteins and amino acids [53]; magnetophoresis used for magnetic particles and cells [54]; dielectrophoresis used for micro particles and cells [55]; acoustophoresis used for micro particles, blood and cells [56] and optical lattices used for micro particles and cells [57]. However, although, the additional forces add separation parameters, and therefore a large variety of separated samples, they also add complexity to chip design, fabrication and data readout mechanisms.

The separation technique used in this thesis is in the category where no external forces are added. Such separation techniques are more simple in regards to fabrication and control units, and — to the authors expectation — will succeed in a broader sense as commercial POC device. The current published on-chip continuous separation techniques that do not use external forces, as well as their applications, are summarized in Table 1.2.

Method	**Separation parameter**	**Sample/Size**	**Ref.**
Hydrodynamic filtration	Size	PS microspheres / 1 µm–3 µm	[58, 59]
Spiral separation	Size	PS microspheres / 1.9 µm–20 µm	[60, 61]
Cascade Squeeze separation	Size	PS microspheres/5 µm–20 µm Yeast cells / 3 µm–5 µm	[62] [62]
Entropic trap array	Size	DNA / 2.322 kbp - 23.13 kbp	[63]
Repulsion array	Charge to size ratio	DNA / 50 bp–766 bp Proteins / 49 kDa–340 kDa	[63] [63]
Cross flow	Size	Blood / 2 µm–10 µm	[64, 65]
Deterministic lateral displacement	size	PS microspheres / 0.6 µm–22 µm Chromosomes / 61 kpb–158 kbp Blood / 2 µm–10 µm Antibody / PE-anti CD41	[66, 67] [68, 69] [70, 71]
Bifurcation	Size, shape	PS microspheres / 16 µm Blood / 2 µm–10 µm	[72] [73]
Brownian ratchet	Size	DNA/48.5 kbp - 167 kbp	[74, 75, 76, 77]
Hydrophoretic filtration	Size	PS microspheres / 1 µm–20 µm Blood / 2 µm–10 µm Cells / 11 µm–22 µm	[78, 79] [80, 81] [82]
Diffusive filter	Size	Blood / 2 µm–10 µm	[83]

Table 1.2: Existing on-chip continuous flow separation methods which only rely on laminar flow in microchannel and no external forces.

Besides deterministic lateral displacement (DLD), the continuous separation techniques in Table 1.2 are either specialized for sorting cells or macromolecules and typically use size as the separation parameter. However, separation using repulsion array and bifurcation techniques also rely on charge and shape respectively. The highest separation resolution of these techniques, reported with DLD, is currently 10 nm [66].

A drawback to all of these separation techniques is that, with respect to a high volume production, they take up a relatively large area in micro-scale perspectives. This issue is further described in the following section.

1.3.1 Pinched flow fractionation

Pinched flow fractionation (PFF) is an alternative continuous separation technique. The principle of PFF is illustrated in Fig. 1.3. A sample containing particles is introduced via a sample inlet channel into a narrow channel called the pinch segment. The particles are aligned (pinched) against a wall in the pinch segment, regardless of size, using the fluid flow from a buffer inlet channel. As the particles move into a wider channel, the broadening segment, the distance from the channel wall to the center-of-mass of the particles is amplified and the particles are separated according to size.

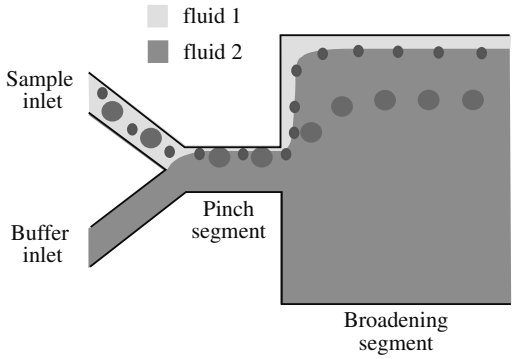

Figure 1.3: The principle of pinched flow fractionation. Particles suspended in a fluid are introduced via a sample inlet channel into the pinch segment. The particles are aligned (pinched) against a wall in the pinch segment, regardless of size, using the fluid flow from a buffer inlet channel. As the particles move into a wider channel, the broadening segment, different sized particles will follow different streamlines and are separated according to size.

Pinched flow fractionation differs from most of the on-chip continuous separation techniques of Table 1.2 in the size of the channel for which separation occurs. The active part of a PFF device, the region containing the pinch segment and the transition to the broader segment, takes up an area typically 400 µm by 400 µm. The channel areas in the techniques presented in Table 1.2 typically span from mm^2 to cm^2 in size. The relatively small area of PFF implies two important advantages. First, PFF can be integrated into a complete analysis system not exceeding a total size of cm^2 and thereby adhere to the design goals of LOC systems. Second, the yield of production scales with the fabricated area. Pinched flow fractionation is therefore less exposed to fabrication errors. In addition, PFF facilitates a simple device design which is compatible with large scale production methods such as thermal rtr imprinting.

Pinched flow fractionation was first introduced in 2004 by Yamada et al. [84]. In their work polystyrene microspheres with a diameter of 15 µm were separated from 30 µm polystyrene microspheres [84]. Yamada suggested a linear relation between the particle radius and position in the broadening segment, assuming that all channels

were much larger in width than in height. This model is further described in Chap. 2. Beside presenting the idea of PFF, illustrated in Fig. 1.3, the authors also presented a slightly modified layout. This was still relying on the same idea, but instead of a broadening segment the pinch segment ended out in five equally large outlet channels, as shown in Fig. 1.4(a). This basically corresponds to an increase in the width of the broadening segment compared to the original design, thereby increasing the separation resolution. Two more sophisticated suggestions on how to increase the separation resolution were published in 2005 by Takagi et al. [85] and in 2006 by Sai et al. [86]. Both studies rely on a device layout where the pinch segment ends out in a branch of outlet channels. By modifying the flow resistance in one or more of the outlet channels, the flow sheets in which particles are present can be distributed between more outlet channels, increasing the separation resolution. Takagi et al. achieved this in a purely geometrical way. Here one of the outlet channels, the drain channel (Branch B), out of 13 outlet channels was designed to have a much smaller hydraulic resistance. In this way 80 % of the fluid would exit through this channel. The idea, illustrated in Fig. 1.4(b), was proven by separation of polystyrene microspheres with a diameter of 1.0 µm, 2.1 µm, 3.0 µm and 5.0 µm as well as separation of erythrocytes from blood. Sai et al. made a more flexible but also more complex solution. They incorporated micro valves in one or two of 5 outlet channels as shown in Fig. 1.4(c). By applying pressure to the valves, the channel floor would expand, thereby decreasing the cross-sectional area of the channel and increasing the hydraulic resistance. The flow rate in the channels equipped with a valve could thereby be varied. The increased separation resolution was proven by separation of 0.5 µm and 0.86 µm polystyrene microspheres — the first step towards nano-scale separation in this type of micro-scale device.

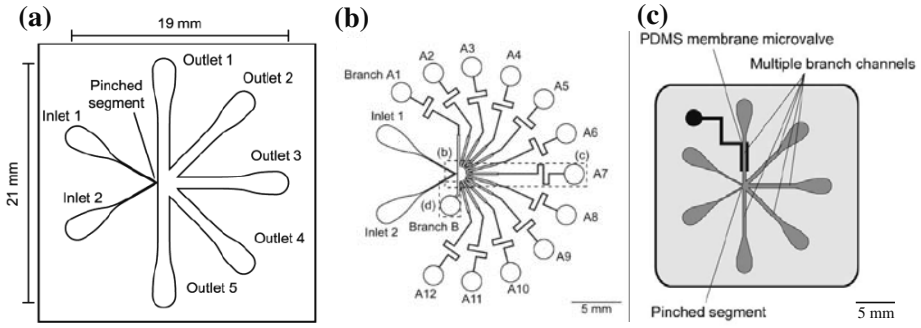

Figure 1.4: Alternative pinched flow fractionation layouts for enhancement of the separation resolution. a) Approach from 2004 published by Yamada et al. [84]. The pinch segment ends out in a branch of outlet channels corresponding to an increase in the width of the broadening segment. b) In 2005 Tagaki et al. [85] included a drain outlet channel, branch B in the figure, where 80 % of the fluid ended. The flow sheets in the rest of the fluid thereby spread out further. c) A similar approach to a) was publish in 2006 by Sai et al [86]. Here control valves were added at one or two of the outlet channels, enabling tunability of the hydraulic resistance.

In 2008 Maenaka et al. demonstrated size-dependent sorting of oil emulsion droplets [87] in water. The separation resolution in the basic PFF layout has been theoretically addressed using the model suggested by Yamada, with an experimental measured res-

olution of 1.8 µm reported by Jain et al. [88]. This relatively poor resolution mainly originates from rough channel sidewalls. Finally, a later theoretical description of PFF devices with rectangular cross-sectional channels was suggested by Andersen et al in 2009 [89] where the experimental results by Takagi et al. [85] were compared with the theory. This model is further described in Chap. 2. In all literature concerning PFF, fluid flow is controlled by syringe pumps at the inlet channels.

In this thesis, PFF is characterized by separation of up to 8 different sizes, a factor of two more than previous results in the literature. In addition, the separation resolution in devices with sidewall roughness below 15 nm is found experimentally. Both separation and resolution of the devices are enhanced by a small modification to the channel layout that is compatible with the thermal rtr fabrication. This would not be possible using the above mentioned suggestions for separation enhancement. Finally, the flow control setup is simplified to only include vacuum at the outlets by a design that utilizes asymmetric inlet channels. The measurement setup is subsequently more simple and user-friendly.

1.4 Detection and analysis

Several macroscopic readout methods have been combined with microfluidic systems. The most frequently used are: optical detection [90, 91], electrochemical detection [92] and thermal lens detection [93]. Unconventional methods, in regards to LOC, such as mass spectroscopy and nuclear magnetic resonance [94] have also been demonstrated. As defined earlier, the ultimate goal of LOC for POC is to integrate complete analysis systems into cheap and portable microdevices that are only a few square centimeters in size. In this perspective a conventional macroscopic detection system is not an option.

There are numerous studies concerning the integration of detection systems in microfluidic devices. These systems can be categorized into two groups: surface sensitive detections and bulk detections. Cantilever based [95] and refractive index sensors [96] are examples of surface detection methods. Here, sample particles are immobilized on or an analyte is brought into proximity to a surface, which are then detected. In microfluidics, cantilever based sensors are usually operated in the so-called stress mode [95]. An immobilized sample causes the cantilever to bend and the induced stress is measured. In that way cantilevers are able to detect changes in pH [97], the formation of self-assembled monolayers [98], DNA hybridization [99, 100], antibody - antigen interactions [99] and adsorption of bacteria [101]. Refractive index-based sensors rely on a change in the optical properties at or near the surface (within 100 nm - 200 nm). Some of these are surface plasmon resonators, which e.g. have been used for detection of proteins [80]; photonic crystal lasers, used for cell growth observation [102]; and ring resonators, used for detection of proteins [103]. Although, the two surface detection methods above can be label free, have high sensitive and have been demonstrated in a large variety of applications, they do not offer any spatial information. In applications where the sample is moving during detection, such as in microfluidic separation (e.g. PFF), on-chip detection methods with spatial resolution, referred to as bulk detection above, are needed. Such on-chip continuous detection methods for LOC separation are summarized in Table 1.3.

On-chip electrochemical and optical detection are the most published continuous

Detection method	**Detection capability**	**Sample/Sensitivity**	**Ref**
Electrochemical	Flow direction	proteins / 0.1 ppm	[104]
		hormones / fM	[105]
		RNA / 0.01 µM	[106]
Optical	Flow direction	DNA / 75 pg/ml	[107]
		yeast / single cell	[108]
		fluorescein / 25 nM	[109]
		Caffein / 60 µg/ml	[110]
Magnetic	Flow direction	microspheres / 2 µm	[111]
	Height of channel	Protein / 27 pg/ml	[111]
	Velocity	SNP / single particle	[112]
		Blood/single cell	[112]
Thermal lens	Flow direction	Ni(II) ions / 6.3 nM	[113]
	3D imaging (1 µm resolution)	Carbaryl pesticide / 70 nM	[114]
		Cytochrome-C / 10 zM	[115]

Table 1.3: On-chip continuous detection methods for lab-on-a-chip separation.

detection methods for microfluid systems. In electrochemical detection, the electric response between two electrodes, usually placed at the bottom and top of the channel, is measured. This method, while label-free, is restricted to samples which respond to an electric signal, and also require integrated electrodes in the microchip design — adding complexity to the fabrication process. An important reason for the success of optical detection is its minimal disturbance of the sample analyte, so long as they are not susceptible to photochemical decomposition. However, besides chemiluminescence, optical detection often involves labeling of the sample. Furthermore, a considerable drawback of on-chip electrochemical and optical detection schemes is their lack of spatial resolution. Only separation with regards to the flow direction can be measured. Thermal lens detection is another optical detection scheme, where absorbed laser light results in heating of the sample which causes expansion, thereby changing the refractive index and the focus depth of transmitted light. This change can be monitored. Yet while the detection is label-free, it can be destructive to some biological systems. On-chip thermal lenses have been demonstrated for imaging of cell growth in microfluidic channels with a spatial resolution of 1 µm [115]. In this work the measuring spot is 1 µm in size and is moved over the sample, thereby creating an image. Thermal lens microscopy is therefore not suitable for systems with fast dynamics, and is mostly used for detection in the flow direction as with the two other techniques already mentioned. Magnetic detection is the only detection method in Table 1.3 which has a spatial resolution in several dimensions at velocities up to cm/s and can be used for particle image velocimetry (PIV) [112]. However; one important drawback of the technique is integration of electrodes which can significantly complicate the fabrication process.

1.4.1 Optofluidic microscope

In PFF, particles are separated along the width axis of the channel (see Fig. 1.3) and therefore an applicable detection method must have a spatial resolution in that direction. In addition, the detection method should be compatible with rtr imprinting without adding major complexity to the fabrication process. One such detection tech-

nique is the optofluidic microscope (OFM) [116], which is a rather newly established technique including more simple fabrication and detection than any of the established techniques in Table 1.3. The OFM consist of an opaque film patterned with apertures arranged in a line which is tilted relative to the flow direction of an above lying microfluidic channel. Time-resolved transmission of light through the apertures as well as knowledge of the laminar flow velocity is used to reconstruct the image of a passing object, at a resolution defined by the dimensions of the aperture array. An image of the original OFM, by Heng et al. [116], placed under a 30 µm wide channel, is shown in Fig. 1.5(a). The apertures were 600 nm in diameter and the measured resolution limit was 490 ± 40 nm. This OFM device was demonstrated in combination with a conventional microscope, which was used as a relay. A similar device was used in 2008 by Cui et al. [117] to image Caenorhabditis elegans and cells with a resolution below 1 µm. In this work, the OFM was fabricated directly on top of a CCD detector, realizing a compact and portable imaging unit. The largest challenge with OFM is the tumbling of sample objects. Images of tumbling particles, which can be up to 45 % of the total, are discarded. Finally, a grid-based OFM, illustrated in Fig. 1.5(b), with apertures of 100 nm in diameter was demonstrated by Heng et al. [118]. They measured a resolution down to 110 nm and because of the grid arrangement of the apertures, the tumbling issue was reduced.

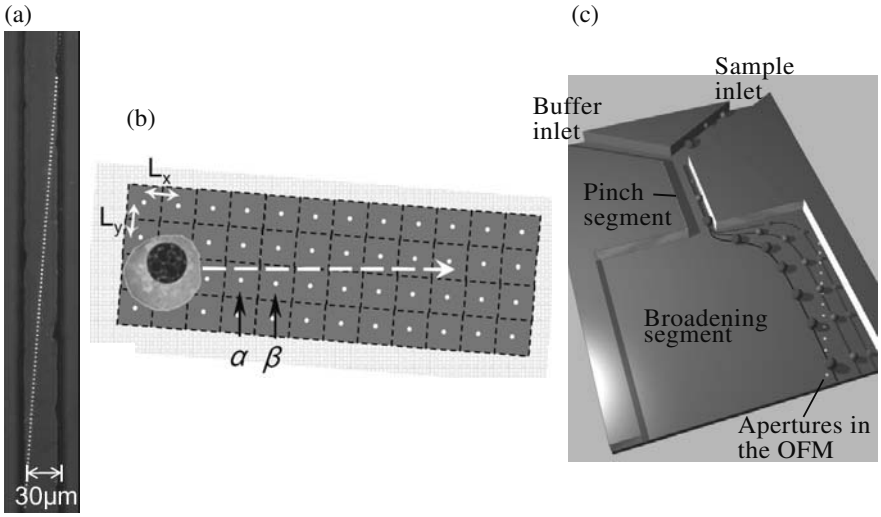

Figure 1.5: (a) The first published optofluidic microscope (OFM), placed underneath a 30 µm wide channel. Reprint from [116]. (b) A schematic drawing of a grid-based OFM and an object moving across the grid in the direction of the sample flow. Reprint from [118]. (c) The principle of an optofluidic microscope in a pinched flow fractionation device. Apertures in a opaque film are placed underneath the broadening segment as illustrated in the figure.

In this thesis the OFM is integrated into a PFF device, positioned under the so-called broadening segment, as illustrated in Fig. 1.5(c). Combining the OFM with PFF enables compact and cheap 3-dimensional detection. Furthermore, tumbling is insignificant in the broadening segment of PFF and usually spherical particles are separated. By choosing the OFM technology as a positioning readout in PFF, tumbling is no longer an issue, which is a clear advantage compared to earlier demonstrations of the

OFM. The opaque film patterned with apertures added complexity to the fabrication, but nevertheless is compatible with the rtr method. A rtr fabricated PFF device with integrated OFM has not been addressed in this thesis and is left for future research.

1.4.2 Windowless x-ray microfluidic platform

LOC systems do not only imply perspectives in cheap POC analysis. Broadly, LOC systems open a large range of possibilities in all research fields where the amount of sample is limited, the volume of the sample must be well controlled and there is a need for pre- or post-treatment in regards to the sample to be analyzed. A part of this thesis involves a study related to the research field of time-resolved high intensity x-ray studies, which spans from fundamental chemistry [119, 120] on the 100 femtosecond time-scale to conformation changes in solvated proteins on the microsecond scale [121]. The necessary spatial (atomic) and time resolution (100 fs) sets up several requirements to the measuring system. The thickness of the sample must be very well controlled and preferably $< 100\,\mu m$ in thickness, there must be as little curvature of the sample interface as possible, as few interfaces as possible in the beam path and a high sample refresh rate. Furthermore, some applications also require vacuum. Several approaches for sample suspended in fluids have been taken to deal with these issues and are summarized in the three following categories.

- *Capillaries* - The liquid sample is circulated through a capillary passing the x-ray beam. The flow stability is high but data retrieval can be complicated due to refractions from interfaces and absorption in the capillary [121].

- *Free-films* - A liquid sheet of a few mm in length is produced by passing the sample through a rectangular nozzle with a width of $100\,\mu m$ to $500\,\mu m$ at flow velocities of $1\,m/s$ to $5\,m/s$. Free-films of liquid sample have been used extensively for time-resolved x-ray studies for more than one decade [122, 123, 124]. However, one of the challenges in this technique is its lack of stability of the film thickness which is critical for high-quality data.

- *Free micro-jet/droplet streams* - The technique with the fastest flow velocity (up to $\sim$100 m/s). For the case of micrometer-sized jets the sample consumption is rather high ($\sim$100 mL/h) [125], which can be reduced a factor 10 by modifying the nozzle, such that the laminar jet is transferred into equally spaced monodisperse droplets [126]. The mono-dispersity of a droplet stream has not yet been characterized. One of the critical issues with this technique is the curved interface of the jet/droplets and the high sample consumption.

The capability of the three approaches described above is summarized in Table 1.4.

In contrast, a microfluidic chip-based system, has a stability as potentially high as the capillary-based approach, non-curved interfaces as the free-film approach, high velocities as the free-films and free micro-jet/droplet stream approach and much lower sample consumption compared to any of the previously mentioned techniques. In addition, a microchip-based platform can have the functionalities of LOC added, e.g. for separation by PFF or in-situ optical characterization. By direct access to the sample, diffraction of the x-rays is minimized and there is no absorption in intermediate layers — all together realizing a better resolution. Finally, the liquid can be restricted

Technique	Time resolution	Thickness stability	Curved sample interface	Vacuum exposure	Sample consumption
Capillaries	ns	High	Yes	Protected	Low
Free-films	ps	Low	No	Yes	Low
Free jets/droplets	ps	High	Yes	Yes	High

Table 1.4: Techniques for time-resolved x-ray measurements with a sample suspended in a fluid.

to flow in microfluidic channels, rather than out in open windows, by using capillary burst valves [116].

In this thesis a chip-based approach for time-resolved x-ray studies of fluidic sample based on CBVs has been developed. The proposed design is illustrated in Fig. 1.6. and will be further described in Chap. 8.

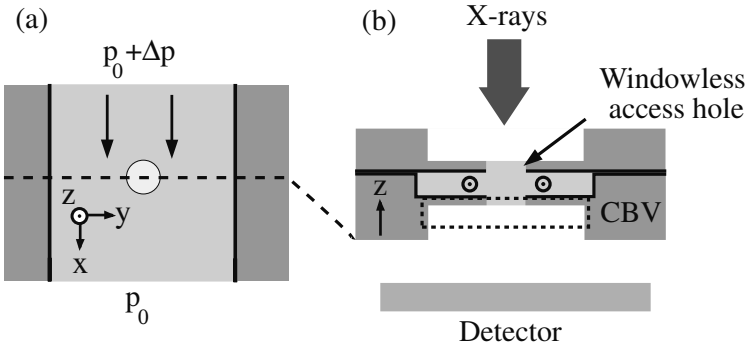

Figure 1.6: The principle of the window-less microfluidic platform relying on capillary burst valves (CBVs) for time-resolved x-ray studies. (a) An open channel with a CBV located in the center of the channel. (b) Cross-sectional view of a sealed device with two CBVs in the top and the bottom of a channel working as the x-ray access hole. After the x-rays have interacted with the sample in the device they are collected by a detector on the backside of the device.

1.5 Aim of the thesis

The aim of the thesis is to:

- Develop a commercial attractable LOC component based on micro-scale PFF, with a reproducible outcome.
  - Which can be designed to be user-friendly, and thereby not limited to experts
  - Which can be fabricated at low cost and high volume by thermal rtr imprinting

- Which by a small modification in the basic layout enable enhancement of the separation and separation resolution, and still be compatible with rtr fabrication
- Which has 3 dimensional detection integrated into the device by an optofluidic microscope
- Which has applicable functionalities demonstrated by detection of single nucleotide polymorphisms
- Which can be down-scaled into the nanometer regime for separation of single proteins

• Develop a LOC platform to be used for time-resolved high intensity x-ray studies.

1.6 Topics and outline of the thesis

To give the reader an overview of the sub-projects in this thesis in relation to the aspects of LOC development illustrated in Fig. 1.1, a diagram is shown in Fig. 1.7. Each of the sub-projects are related to parts of the aim, and involve state-of-the-art research and development. Most of the work has been published or are in the process of. A list of publications is appended in Appendix A.

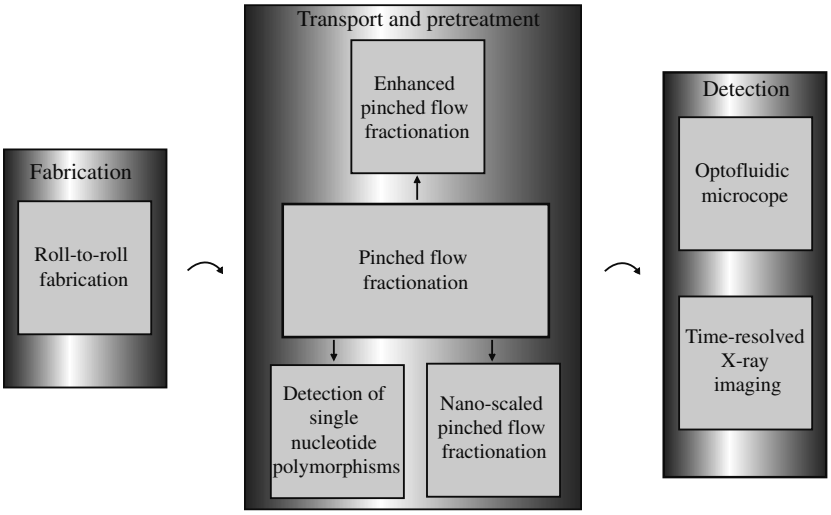

Figure 1.7: Overview of the sub-projects of this thesis in relation to the aspects of LOC development illustrated in Fig. 1.1.

The structure of this thesis is related to the schematic illustration in Fig. 1.7. Starting with the microfluidic separation technique used throughout the work — Pinched flow fractionation — a description of the theoretical formulation, separation measurements and an user-friendly device layout is presented. Afterwards, the fabrication methods are presented, with emphasis on nanoimprint lithography (NIL) and a high volume fabrication scheme for microfluidic LOC structures, based on thermal rtr methods. This is followed by a presentation of an enhancement method of the separation in

PFF, integration of PFF with an optofluidic microscope, detection of single nucleotide polymorphisms in PFF devices and down-scaling of the devices for single protein separation. Development of a windowless microfluidic platform for time-resolved high intensity x-ray studies is described in the end of the thesis before the entire body of the work is concluded and an outlook is presented. Below is a list of the chapters and their content.

- *Chapter 2: Pinched flow fractionation*
  Pinched flow fractionation is characterized theoretically and experimentally. The resolution of separation is introduced, calculated and measured. Finally, a user-friendly device design is presented.

- *Chapter 3: Fabrication of micro- and nanofluidic devices*
  All fabrication processes used in this work are introduced, where the main technique, nanoimprint lithography, as well as the fabrication method relying on rtr are described in detail.

- *Chapter 4: Enhancing the separation in pinched flow fractionation*
  A new technique to enhance separation in PFF with a slightly reduced channel area, feasible with roll-to-roll fabrication, is demonstrated.

- *Chapter 5: Optofluidic microscope for detection in pinched flow fractionation*
  A compact detection unit for detection of separated particles in PFF, relying on integration of an optofluidic microscope, is described.

- *Chapter 6: Detection of Single Nucleotide Polymorphisms — an application of PFF*
  Pinched flow fractionation is demonstrated as a microsphere-based array for detection of single nucleotide polymorphisms from a human genomic sample.

- *Chapter 7: Nano-scaled separation*
  The first steps towards a sub 100 nm PFF-based separation device is introduced and the channels are functionalized with a protein repellent coating.

- *Chapter 8: Microfluidic platform for time-resolved high intensity x-ray measurements*
  A windowless microfluidic platform based on capillary burst valves is fabricated, characterized and demonstrated for time-resolved x-ray measurement. The capability of protein and wet chemistry handling for the system is also described.

- *Chapter 9: Conclusions and outlook*
  All work is concluded upon and a short outlook is given.

Chapter 2

Pinched Flow Fractionation

Pinched Flow Fractionation (PFF) is a continuous size-dependent fluidic separation technique relying on laminar flow in micrometer or nanometer-size channels. One powerful aspect of PFF in terms of fluidic LOC components is that it works without any applied external fields. Furthermore, since PFF is a continuous process it is applicable both in regards to separation on one hand, and in diagnosis combined with other up- or down-stream continuous processes on the other.

The principle of PFF is described in the beginning of the chapter. After a short summary of the theoretical microfluidic concepts, necessary for calculating the fluidic flow in PFF, analytical and numerical models for the flow in the pinch and the broadening segment, are introduced. The numerical model is developed during the thesis and is published in [127]. These models do not take particles in the system into account — simply because such a description involves complex particle interactions with channel walls and perturbation of the flow, which is beyond the scope of this thesis. However, a qualitative discussion on the effect of particles with references to literature is included. Afterwards, the separation resolution and the limitations in PFF are discussed, and PFF is experimentally evaluated with the separation results compared to the theoretical models. Finally, a user-friendly PFF device only relying on vacuum at the outlets is described. A part of the experimental section, concerning the device layout and separation of polydisperse samples with high solid concentration, is published in [128].

2.1 The principle of pinched flow fractionation

The principle of PFF is illustrated in Fig. 2.1. Two inlet channels, the sample inlet and the buffer inlet, merge together in one narrow channel, the pinch segment, which ends out in a much broader channel, the broadening segment. A sample containing particles is introduced via the sample inlet channel into the pinch segment. The sample particles are aligned (pinched) against a wall in the pinch segment, regardless of size, using the fluid flow from the buffer inlet channel. A particle is pinched when the width of the sample fluid is smaller than the radius of the particle. As the particles move into the broadening segment, the distance from the channel wall to the center-of-mass of the particles is amplified, and the particles are separated according to size. The distance from the channel wall to the center of the particles in the broadening segment is denoted y'. The two main requirements for PFF to work are laminar flow and a

difference in size of the particles to be separated. The particles are assumed to follow a streamline corresponding to their center position when they are pinched to the channel wall of the pinching segment. In the case of non-spherical particles, it is the smallest dimension which defines the separation. This is experimentally demonstrated with red blood cells in [85].

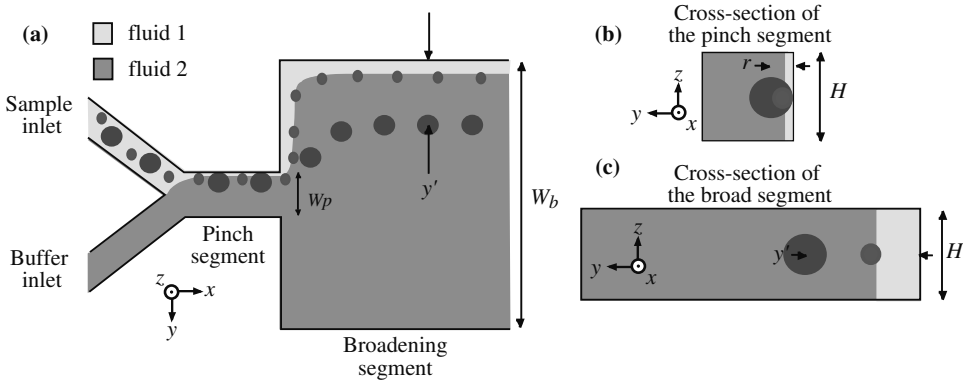

Figure 2.1: (a) The principle of pinched flow fractionation (PFF). Two fluidic inlet channels, the sample inlet and the buffer inlet, merge together in one narrow channel, the pinch segment, which ends out in a much broader channel, the broadening segment. Fluid from the buffer inlet is used to focus the fluid and align the particles from the bead inlet against a channel wall in the pinch segment. When the particles enter the broadening segment, different sized particles will follow different streamlines in the fluid and separate accordingly. (b+c) Cross-sectional view of the pinch situation for the smallest spheres.

Important design parameters are illustrated in Fig. 2.1. These are the width of the pinch segment, w_p, the width of the broadening segment, w_b, and the channel height, H. Especially, w_p and w_b are important parameters regarding separation. H is more relevant in clogging issues, discussed later in Sec. 2.4.4.

2.2 Flow calculations in pinched flow fractionation

Fluids constitute the active element in most LOC systems as well as in PFF, and it is therefore the theoretical concepts of microfluidic dynamics that are needed to calculate the flow parameters in PFF. The governing equations of microfluidic are the Navier-Stokes equation, see Eqn. 2.1, and the continuity equation, see Eqn. 2.2.

$$\rho\left[\partial_t \upsilon(\mathbf{r},t) + (\upsilon(\mathbf{r},t)\cdot\nabla)\upsilon(\mathbf{r},t)\right] = \sum_j \mathbf{f}_j \tag{2.1}$$

$$\partial_t \rho = -\nabla\cdot(\rho\upsilon(\mathbf{r},t)) \tag{2.2}$$

Here ρ is the density of the fluid, ∂_t is the partial derivative with respect to time, $\upsilon(\mathbf{r},t)$ is the velocity of the fluid at position $\mathbf{r}$ and time t and $\mathbf{f}_j$ is the body forces acting on the system per unit volume. Navier-Stokes (N.S.) equation is in the form given here describing incompressible fluids, which is a reasonable assumption for most microfluidic systems and pertains to the work in this thesis.

A comprehensive derivation and description of the equations is given elsewhere [129]. The N.S. equation and the continuity equation are used in the calculation of the following models. A special case of the two equations is commonly applicable in pressure driven microfluidic systems, namely steady state solutions of laminar flows. Here the two equations are simplified to:

$$0 = -\nabla p + \eta \nabla^2 \upsilon(\mathbf{r}, t) \tag{2.3}$$

$$\nabla \cdot \upsilon(\mathbf{r}, t) = 0 \tag{2.4}$$

The N.S. equation is in this case denoted the time-independent linear Stoke equation.

2.2.1 Analytical models

In this section two analytical models are presented. Here, particles are assumed not to perturb the fluid flow, not to interact with the channel wall and their center of mass to follow specific streamlines in a laminar flow. The assumption of laminar flow is verified in Sec. 2.2.2. The continuity equation, also denoted as mass conservation is used to describe a correspondence between the fluid flow per time (flow rate) in the pinch segment and in the broadening segment. The flow rate passing in the pinch segment, Q_p, from the aligning wall to a specific point, r, must equal a corresponding flow rate in the broadening segment, Q_b, from the channel wall to a specific point, y'. This is written in Eqn. 2.5 and the situation illustrated in Fig. 2.1(b) and 2.1(c).

$$Q_p(r) = Q_b(y') \tag{2.5}$$

The flow rate is given by a spatial integration over the channel segment of the velocity field in the fluid, $v_x(y, z)$, written as in Eqn. 2.6.

$$Q(\delta) = \int_0^H dz \int_0^\delta dy \; v_x(y, z) \tag{2.6}$$

Here z and y is the direction in regards to the height and the width of the channel, H is the channel height and δ is a specific point in the channel. In the case of Eqn. 2.5, δ equals r in the pinch segment and y' in the broadening segment.

As the particles are assumed not to perturb the flow, or interact with the channel wall and are aligned perfectly up against the channel wall in the pinch segment (under pinch conditions), the r variable in Eqn. 2.5 can be set equal to the radius of the particles. The velocity field in the fluid, necessary for these calculations, is found from the N.S. equation.

In the pioneering paper by Yamada and co-workers [84], a simple model to describe PFF was suggested. Here, the velocity field was assumed constant. Using the above procedure, the distance from the center of a spherical particle to the channel wall in the broadening segment, y', was calculated to be linear dependent on the radius of the particle, r, see Eqn. 2.7.

$$y'(r) = \frac{w_b}{w_p} r \tag{2.7}$$

For a pressure driven flow, which is mostly the case for PFF, Eqn. 2.7 describes a system with a large width, w, to height, H, ratio in the pinch and broadening segment

($w_p >> H$ and $w_b >> H$). However, this ratio is rarely the case for PFF studies. The velocity field in the x-direction (see Fig. 2.1), $v_x(y,z)$, in rectangular channels where $w > H$, can be calculated from the time-independent linear Stoke equation. This is derived in [129] and the solution is written in Eqn. 2.8.

$$v_x(y,z) = \frac{4H^2\Delta p}{\pi^3 \eta L} \sum_{n,odd}^{\infty} \frac{1}{n^3} \left[1 - \frac{cosh\left(n\pi \frac{y}{H}\right)}{cosh\left(n\pi \frac{w}{2H}\right)} \right] sin\left(n\pi \frac{z}{H}\right) \tag{2.8}$$

Here Δp is the pressure difference between the entrance and exit of the channel, η is the viscosity of the fluid, L is the length of the channel and n is an odd integer.

For channels with square cross-section, which is approximately the case for the pinch segment in this thesis ($H = 12.5\,\mu m$ and $w_p = 11.7\,\mu m$), there does not exist any analytical solutions to the time-independent linear Stokes equation. However, the error using Eqn. 2.8 is "only" 13 %, and already at an aspect ratio of one half, $w = 2H$, the error is down to 0.2 %. Therefore, as a first approximation, the velocity field in Eqn. 2.8 is used in both the pinch and broadening segment. y' as a function of r is then calculated combining Eqn. 2.5, 2.6 and 2.8 (n=3). This approach is published by Andersen et al. [89]. The solution to this model and the more simple solution of Yamada is plotted and compared to experimental data in Sec. 2.4.

2.2.2 A numerical model

As observed and discussed by Jain et al. [88], the linear model for PFF, Eqn. 2.7, overestimates the distance between particles and the wall in the broadening segment by up to 60 %. Data from this thesis for polydisperse samples with particle concentrations up to 0.05 % weight per volume buffer liquid (% w/v) and monodisperse samples with solid concentrations up to 1.0 % w/v (see Sec. 2.4) are consistent with Jains observations. The more advanced analytical model, introduced in Sec. 2.2.1, is compared with measured values in Sec 2.4, and is seen to be more accurate for measurements with the above mentioned sample types, compared to the linear model, but does however underestimate the measured values.

None of the analytical models describe the measured y'-values very well and a semi-3D numerical calculation of the flow in PFF is therefore presented. However, there is still the assumption that the particles do not perturb the fluid flow or interact with the channel walls. The only particle effect that is taken into account is a corner effect at the interface between the pinch segment and the broadening segment as illustrated in Fig. 2.2. At this point the streamlines in the fluid are forced closer to the wall compared to their position in the pinch segment. Particles will therefore be forced to follow streamlines further into the fluid, and thereby end farther away from the wall in the broadening segment, than when the particle position in the interior of the pinch segment is considered as in the analytical models.

COMSOL Multiphysics [130] is used to perform the numerical calculation. The basic numerical method used in COMSOL is the finite-element method (FEM). FEM is perhaps not the obvious choice for numerical fluid simulation in general where turbulence occurs, but for low Reynold numbers, which is mostly the case in microfluidics, FEM is very good. A more comprehensive description of the FEM and the above mentioned issue is given in [129]. A 2D drawing of the PFF devices seen from above

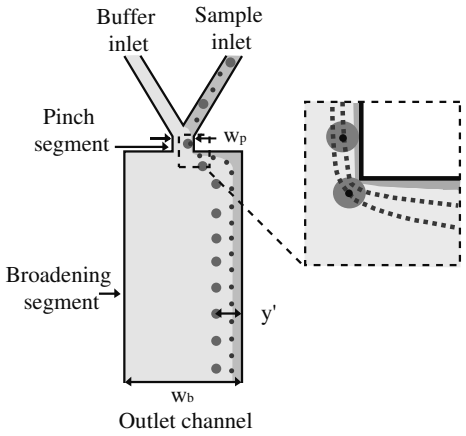

Figure 2.2: Illustration of the so-called corner effect. Particles are not able to follow the initial streamline as it passes the corner — connecting the pinch and broadening segment.

as in Fig. 2.1(a) is drawn in COMSOL. The steady-state N.S. equation is applied to all sub-domains (the internal regions of the device), no-slip boundary conditions are added to all channel walls and the flow rate in the two inlet channels is set to the same value as used in the measurements, $5\,\mu L/hr$ and $600\,\mu L/hr$ in the sample and buffer inlet channels, respectively. The real PFF devices also have a finite height of $12.5\,\mu m$ in this study. To compensate for the hydraulic resistance from the bottom and top surface of the channels a volume force, $\mathbf{F} = -a * v_x(y)$, is introduced in the opposite direction of the velocity field, $v_x(y)$, according to lubrication theory [129]. Here, $a = 12\eta/H^2$, where η is the viscosity of the buffer and H is the height of the channels. The finite height of the device is thereby taken into account by the model, which is therefore denoted as semi-3D. The numerical solution is compared to the two analytical solutions and the measured values in Sec. 2.4.

Besides calculating y' in PFF, the semi-3D numerical model can be utilized to evaluate the flow regime for whether it is laminar or turbulent. However, at turbulent flow which has a high Reynolds number COMSOL does not converge towards a solution and can therefore not be used. In laminar flow, in which diffusion is neglected (will be discussed later), each fluid particle follows a fixed path known as a streamline. Two different fluid particles with the exact same initial conditions will follow the same streamline and end in the same exit position. In turbulent flow the inertia forces dominates viscous forces and the streamlines fluctuate erratically. In this regime two fluid particles with same initial conditions will no longer end in the same exit position. In general, the flow is considered laminar if $Re < 2300$ and turbulent if $Re > 2300$. In the regime at which Re is between 1 and 2300 the flow undergoes a continuous transition from laminar to turbulent. It is first when $Re < 1$ that the flow is said to be extremely laminar. This regime is where the earlier mentioned time-independent linear Stokes equation is valid [131]. To illustrate the transition regime, three different flow velocities in the pinched flow fractionation layout are simulated and the results are plotted in Fig. 2.3. In each situation the ratio of the flow rate in the two inlet

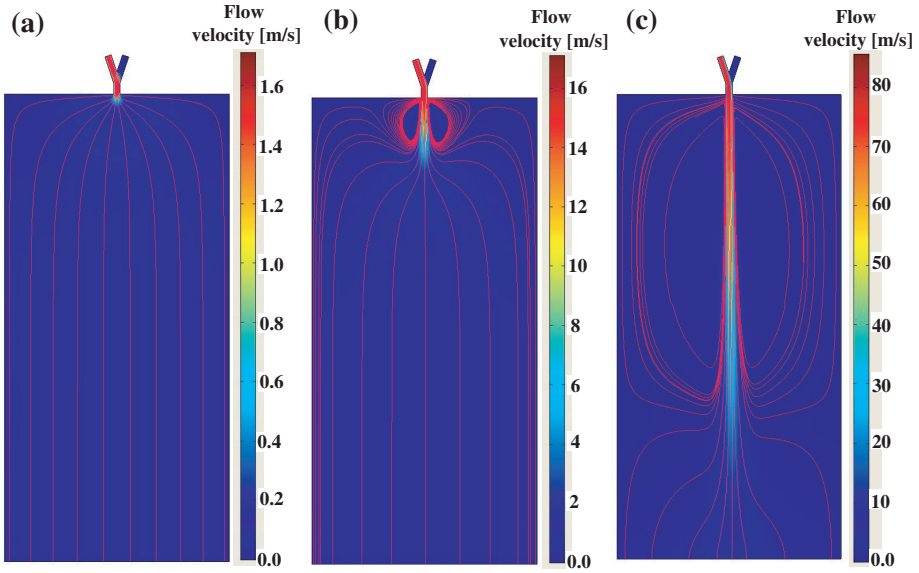

Figure 2.3: Flow simulations of the active part in pinched flow fractionation. The three figures illustrate streamlines in the fluid at different flow velocities. (a) is the same velocities as used in the measurements. Re is in this case up to 6. In (b) the velocities are a factor 10 larger than in the measurements. Re is in this case up to 58. And finally in (c) the velocities are a factor 50 larger than in the measurements. Re is in this case up to 650. Water at 20 °C was used as the liquid in the simulations.

channels is kept constant at a ratio sufficient to accomplish pinched flow. The flow rates in Fig. 2.3(a) are the same as in the basic PFF separation measurements (further described in Sec. 2.4), namely 5 $\mu L/hr$ and 600 $\mu L/hr$ in the sample inlet and buffer inlet respectively. The resulting Re number is up to 5.7 in the pinch segment and much smaller than 1 in the broadening segment. The flow rates are increased by a factor of 10 and 50 in Fig. 2.3(b) and 2.3(c) respectively, resulting in Re numbers up to 58 and 648. As a result of the increasing flow rates, tumbling at the sharp corners in the transition between the pinch and broadening segment occurs. Even though most of the streamlines pass the tumble zones and spread out afterwards, some streamlines also enter the tumble zones and so do small particles. As particles add up in this region, the flow pattern changes and finally destroys the functionality of the device.

2.2.3 Particles in the system

Even though the interest for suspensions in microfluidic systems has increased hand-in-hand with microfluidics, migration of particles across streamlines in these systems has only been studied within the last several years. The number of publications are therefore limited and the responsible mechanisms are not fully understood. The current publications for this work can be divided in two groups. One dealing with high concentration suspensions and low Reynolds Numbers ($\ll 1$) and a second dealing with low concentration suspensions and large Reynolds numbers (> 1). Two recent publications, one from each group, including experimental and theoretical work, are

reviewed in this section in order to answer whether pinched particles are influenced into migrating across streamlines during separation in PFF devices.

In the first paper by Yapici et al. [132] the migration of hard spheres in high concentration suspensions (solid volume fraction $> 10\,\%$ w/v), is calculated for low Reynolds numbers ($\mathrm{Re} \ll 1$) by conservation of mass, energy and momentum in the system. In this calculation, the interaction between spheres is included and found to be dominant over their migration across streamlines in a Poiseuille flow. The main conclusion is that they migrate towards the center of the channel due to a combination of interactions between particles and shear minimization in the system. In the second paper by Di Carlo et al. [133] the migration of particles of diameter $d = 2r$ in square channels of width, w, equal to $40\,\mu$m is calculated using COMSOL Multiphysics. In their work the solid concentration is kept low, to avoid interactions between particles, and the ratio $2r/w$ is kept above 0.1 with minimum sphere diameters of $5\,\mu$m. Furthermore, flow rates corresponding to Reynold numbers of 2 to 80 are used, so inertia in the fluid is therefore of considerable importance, contrary to the study by Yapici. Di Carlo et al. conclude that the particles aligned to a wall are influenced by an effective lift force pointing away from the channel wall towards the center. However, the equilibrium is not in the center of the channel as described by Yapaci but displaced towards the wall, which can be explained by two contributing factors. One caused by the wall pointing towards the channel center line and a second caused by the shear gradient present in the curved velocity profile of the poiseuille flow pointing towards the channel wall. The equilibrium position depends on the ratio $2r/w$.

The channel structure and flow velocity examined by Di Carlo is in the same range as the dimensions of the pinch segment and velocity in the pinch segment for the PFF characterization presented in this chapter. In addition, the microspheres used in this thesis for separation have radii ranging from $0.26\,\mu$m to $2.5\,\mu$m. Here the ratio, $2r/w$, ranges from 0.04 to 0.43 ($w = 11.7\,\mu$m), which are in the same range as in the study by Di Carlo. In the following, the effect of the lift force, F_{lift}, on the 8 different microsphere sizes relevant in this study, is therefore evaluated on the basis of the article by Di Carlo. The flow conditions in the basic PFF measurements, described in Sec. 2.4, are used in these calculations. For all microsphere sizes used in the PFF studies F_{lift} is given by:

$$F_{lift} = f_l \frac{64 \rho U_m^2 r^6}{w^4} \tag{2.9}$$

Here f_l is a non-dimensional lift coefficient calculated in [133], ρ is the particle mass density (polystyrene: ρ=1050 kg/m^3) and U_m is the maximum velocity in the pinch segment (1.7 m/s).

The distance that a microsphere migrates, s_{lift}, because of the lift force, can be calculated from basic motion resulted by a constant force as given by:

$$s_{lift} = \frac{3 F_{lift} t_p^2}{8 \pi \rho r^3} \tag{2.10}$$

Here t_p is the time the particle spends in the pinch segment. In the basic PFF measurements this is on average 12 µs.

In Table 2.1 s_{lift} in the pinch segment and the resulting change in y', $\Delta y'$, is calculated. The last column in the table is the corresponding percentage of the numerically

calculated y'. As seen from the table, the effect of the lift force on the separated par-

Radius [μm]	**2r/w**	$\mathbf{f_l}$	$\mathbf{F_{lift}}$ [N]	$\mathbf{s_{lift}}$ [μm]	$\mathbf{\Delta y'}$ [μm]	$\mathbf{\frac{\Delta y'}{y'}100}$ [%]
0.26	0.04	0.016	$5.12*10^{-17}$	0.00003	∼0	∼0
0.50	0.09	0.072	$1.17*10^{-14}$	0.0011	∼0	∼0
0.75	0.13	0.188	$3.47*10^{-13}$	0.0093	0.14	1
1.05	0.18	0.320	$4.44*10^{-12}$	0.044	0.72	4
1.25	0.21	0.412	$1.63*10^{-11}$	0.095	1.74	8
1.5	0.26	0.524	$6.19*10^{-11}$	0.208	3.97	14
2.0	0.34	0.350	$2.3*10^{-10}$	0.330	7.18	17
2.5	0.43	0.182	$4.61*10^{-10}$	0.335	8.11	13

Table 2.1: Result of the lift force, F_{lift}, on the separated polystyrene microsphere sizes relevant in this study, with flow conditions as in the basic PFF measurements. Here r is the microsphere radius, w is the channel width, f_l is a non-dimensional lift coefficient calculated in [133], s_{lift} is the resulting migration in the pinch segment, $\Delta y'$ is the effected change in position in the broadening segment and the last column is the corresponding percentage of the expected y' calculated by the numerical model.

ticles in PFF become detectable for radii $\geq$ 0.75 μm and should have a large effect on the larger particles. The lift force could explain lower calculated values compared to measurements in the earlier introduced models, which does not take effect of particles into consideration. The lift forces will be used when evaluating the comparison between measurements and the above described models.

2.3 Separation resolution

The most important indicator of success in separation is its resolution, R. The resolution in separation related processes, R_s, of particles which have a Gaussian distribution in the separation direction, can be defined as in Eqn. 2.11 ([47], p. 101-105).

$$R_s = \frac{\delta y'}{2(\sigma_1 + \sigma_2)} \tag{2.11}$$

Here $\delta y'$ is the distance between the average position of two differently sized particles and σ_1 and σ_2 is the standard deviation in position of the particle sizes.

For complete separation R_s must be at least unity, so the minimum separation distance $\delta y'_s$ is given in Eqn. 2.12.

$$\delta y'_s = 2(\sigma_1 + \sigma_2) \tag{2.12}$$

If the separation of particles only have to be detectable and not completely physically separated, the resolution, R_d, is given in Eqn. 2.13.

$$R_d = \frac{\delta y'}{\sigma_1 + \sigma_2} \tag{2.13}$$

For detectable separation R_d must be at least unity, so the minimum distance $\delta y'_d$ is given in Eqn. 2.12.

$$\delta y'_d = \sigma_1 + \sigma_2 \tag{2.14}$$

In this study two factors contribute to σ_1 and σ_2 and are thereby responsible for limitations in the resolution. These are: 1) Brownian diffusion, σ_{diff}, which is by nature present for any set of particles and 2) size distribution, σ_r, which is specific to the sample. In general there is also a contribution from roughness of the channel wall in the PFF device. In this study the roughness of the wall is 15 nm both in the plane of the wall and perpendicular to it (described in Chap. 3). The radius of the smallest microspheres in the later characterization is 260 nm, and therefore the effect of the wall roughness on the microspheres is negligible.

The diffusion consists of two contributions. 1) Diffusion in the pinch segment after pinching, $\sigma_{diff,p}$, which is amplified as the spheres move into the broadening segment. 2) Diffusion in the broadening segment from the beginning of the broadening segment to the measuring point, $\sigma_{diff,b}$. Amplification of diffusion in the expansion region of the broadening segment is neglected. The error of this approximation depends on the flow velocity and particle size, because diffusion during the streamline expansion is enhanced by the same factor as the microspheres are separated. During the expansion in the first approximately 20 µm of the broadening segment the average velocity is 0.4 m/s (found with COMSOL) in the basic PFF measurements. This corresponds to a diffusion of approximately 9 nm, resulting in 0.16 µm after expansion for the smallest microspheres applied ($r = 0.26$ µm). As a consequence, this approximation will result in a small underestimation of σ_{diff}, which is negligible when $r \geq 1.05$µm.

The total contribution to σ_1^2 and σ_2^2 can be written as a sum of the variance of the diffusion in the pinch segment, $(\sigma_{y'}(\sigma_{diff,p}))^2$, the particle size distribution, $(\sigma_{y'}(\sigma_r))^2$, and diffusion in the broadening segment, $\sigma_{diff,b}^2$, as given in Eqn. 2.15

$$\sigma = \sqrt{(\sigma_{y'}(\sigma_{diff,p}))^2 + (\sigma_{y'}(\sigma_r))^2 + \sigma_{diff,b}^2} \tag{2.15}$$

If sizes with small separation in y' are considered, their standard deviation will be similar in size and an average value, σ_{av}, can be used. In this case, introducing Eqn 2.15 into Eqn 2.14, the detection resolution of separated microspheres, $\delta y'$, is given in Eqn. 2.16.

$$\delta y' = 2\sqrt{(\sigma_{y'}(\sigma_{diff,p}))^2 + (\sigma_{y'}(\sigma_r))^2 + \sigma_{diff,b}^2} \tag{2.16}$$

To get a quantitative idea of the consequences of Eqn. 2.16 on the detection limit in size, δr_d, of separated particles in PFF, the linear analytical model, Eqn. 2.7, can be combined with Eqn. 2.16, and the result is given in Eqn. 2.17.

$$\delta r = 2\sqrt{\sigma_{diff,p}^2 + \sigma_r^2 + \left(\frac{\sigma_{diff,b}}{\frac{w_b}{w_p}}\right)^2} \tag{2.17}$$

According to the linear analytical model δr, will decrease (higher resolution) with increasing width ratio between the broadening and the pinch segment, w_b/w_p. This is the idea behind enhanced PFF (EPFF), described in Chap. 4.

The highest detectable resolution, $\delta r_{d,h}$ is defined as the case of no size distribution in the sample. This value is calculated in the next section and the expected resolution, including the size distribution of the used sample, is calculated in Sec. 2.4 and compared to the measured resolution.

2.3.1 Limitations to the resolution

The size distribution of the polystyrene (PS) microspheres used throughout this thesis is Gaussian, centered around the nominal radius, with a standard deviation, σ_r, of 5 % of the nominal radius [134]. Particles are separated in PFF according to how close they can get to the channel wall in the pinch segment, which to a good approximation is given by their radius. Therefore, the distance y' of a Gaussian size-distributed particle sample will also be Gaussian. In addition, diffusion in the system causes the separated particles to change their streamline. Diffusion is a random process, equal in all directions, and is therefore expected to broaden the original Gaussian distribution. Even if the particles do not have a distribution in size, diffusion will cause the separated particles to have a Gaussian distribution around y'. Such Gaussian distribution in y' is observed in this thesis and reported in [88].

The Brownian diffusion length, σ_{diff}, in one dimension is given by $\sigma_{diff} = \sqrt{2Dt}$, where t is the diffusion time and D is the diffusion constant, given by the Einstein equation in Eqn. 2.18.

$$D = \frac{k_B T}{\gamma_0} \tag{2.18}$$

Here k_B is the Boltzmann constant, T is the temperature and γ_0, according to the Stokes equation, is given by $\gamma_0 = 6\pi\eta r$, where η is the viscosity of the fluid ($\approx 10^{-3}$ Pa s for water at room temperature) and r is the particle radius.

Radius [µm]	$\sigma_{\mathbf{r}}$ [µm]	$\sigma_{\mathbf{y'}}(\sigma_{\mathbf{r}})$ [µm]	$\sigma_{\mathbf{diff}}$ [µm]	$\delta\mathbf{r_{d,h}}$ [nm]
0.26	0.013	0.25	0.51	62
0.5	0.025	0.58	0.36	44
0.75	0.038	0.75	0.29	40
1.05	0.050	1.36	0.25	31
1.25	0.063	1.80	0.23	25
1.5	0.075	2.00	0.21	22
2.0	0.10	3.20	0.18	16
2.5	0.125	4.55	0.16	13

Table 2.2: Limitations to the separation resolution in the basic PFF measurements. The total flow rate in these measurements is 605 $\mu l/hr$. Channel dimensions are described in Sec. 2.4. The measuring position is half-way down the broadening segment, which is 5 mm from the pinch segment. σ_r is the standard deviation in size of the microspheres, $\sigma_{y'}(\sigma_r)$ is the standard deviation in y' resulting from σ_r, σ_{diff} is the total diffusion of the separated microspheres from the beginning of the pinch segment to the measuring point and $\delta r_{d,h}$ is the upper detection limit, defined for the case where there is no size distribution in the sample.

The effect on y' from the uncertainty in size, $\sigma_{y'}(\sigma_r)$, and the diffusion, σ_{diff} from pinching in the pinch segment to the measuring point, including both $\sigma_{diff,p}$ and $\sigma_{diff,b}$, are calculated using the experimental conditions of the basic PFF measurement and listed in Table 2.2. The effect on y' from the size distribution is calculated by the already presented numerical model. In addition, the highest detection limit in size, $\delta r_{d,h}$, of separated particles in the basic PFF measurement is calculated using the

numerical model and the calculated diffusion. These values are listed in Table 2.2.

As seen from Table 2.2, diffusion adds, in the case of the basic PFF measurements, a small contribution to the spreading of separated microspheres. However, for the smallest spheres it is comparable to the effect caused by the size distribution, and sets a lower limit to the resolution (given in Table 2.2, collum 4).

2.4 Experimental characterization

In this section the basic PFF device layout and the experimental measurement setup is described, followed by a presentation of the separation measurements.

2.4.1 Device layout

A single PFF design, with small variations at the outlet channels, has been used in several of the sub-projects dealing with PFF: characterization of PFF (this chapter) roll-to-roll imprinted PFF devices (Chap. 3), separation enhancement in PFF (Chap. 4), optofluidic microscope detection in PFF (Chap. 5) and DNA analysis utilizing PFF devices (Chap. 6). This specific design is denoted as basic PFF and is described here.

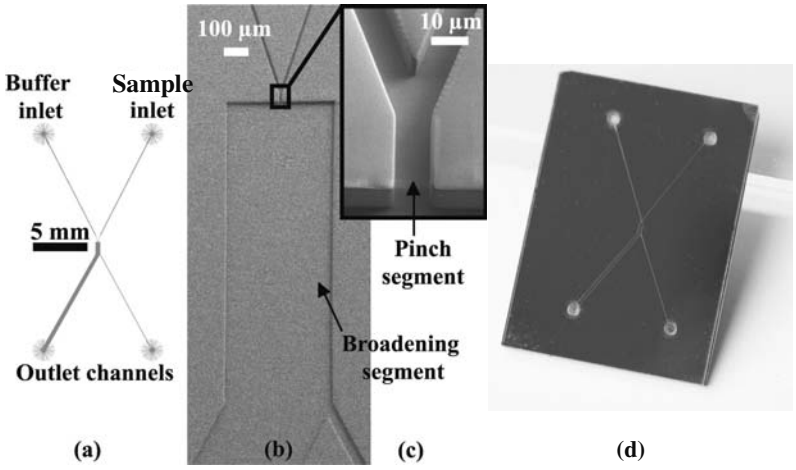

Figure 2.4: The pinched flow fractionation device. (a) Layout of the device. The device is 2 cm x 3 cm in size. (b) and (c) scanning electron microscopy (SEM) images of the imprinted pinched flow fractionation device. (c) is the pinch segment and is an enlargement of the box in (b). Vertical sidewalls are clearly seen. (d) A camera image of the device. The microfluidic channels all have a height of 12.5 µm.

The layout of the basic PFF device is shown in Fig. 2.4(a). It consists of two inlet channels that merge together in the pinch segment, with width and length equal to 11.7 µm and 20 µm respectively. The two inlet channels are similar and consist of two parts, starting from the inlet holes being 50 µm wide and 10 mm long, then narrowing down in width to 11.7 µm. The narrow part is 1000 µm long. The pinch segment ends out in the broadening segment, with width and length of 400 µm and 1000 µm respectively. For the roll-to-roll fabricated devices and the DNA analysis PFF device, the broadening segment ends in two asymmetric outlet channels, one narrow (47 µm in

width) and one wide (400 µm in width). Under pinched flow conditions, the particles with a radius smaller than 2.2 µm will be directed into the narrow outlet channel, and larger particles will end up in the wide outlet channel. The layout was used to separate different single nucleotide polymorphisms (SNPs) in the work with SNP detection by PFF. All channels are 12.5 µm high giving a total channel volume of 72 nL. In the OFM integrated PFF devices, the two outlet channels are both 400 µm wide.

2.4.2 Measurement setup

Separation in the PFF devices have been characterized utilizing the measurement setup shown in Fig. 2.5. The measurement setup consist of two parts: The fluorescence mi-

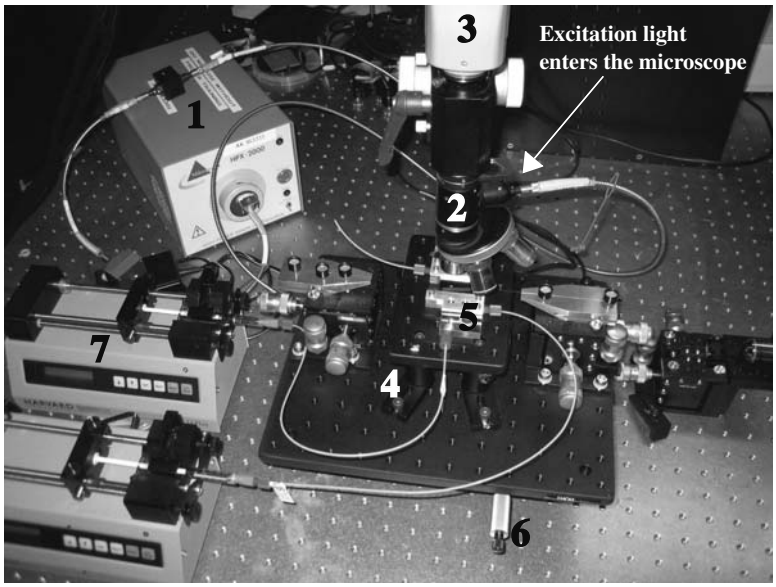

Figure 2.5: A photograph of the measurement setup. The labels in the picture correspond to: (1) 50 W excitation light source, (2) a microscope, (3) CCD camera, (4) a breadboard on which a device holder is fixed, (5) a device holder in which the PFF device is clamped, (6) two translational stages and (7) two syringe pumps.

croscope and a platform containing fluidic connections on which the device is clamped. In the following description the numbers in brackets refer to Fig. 2.5. The fluorescence microscope part consist of a 50 W excitation Neon light source (1) from Mikropack (HPX-2000), a custom made microscope from Opto Bedarf Gmbh with several objectives and excitation/emission filters (2), and one of two CCD-based cameras: 1) $\frac{1}{2}$-type Progressive Scan IT from the Sony Corporation or 2) DP253 from DeltaPix (3). The excitation light is guided from the light source by an optical fiber to the microscope. When it reaches the microscope it passes through an excitation filter, a 50/50 mirror and is focussed onto the PFF device by an objective. The emitted light from a fluorescent sample in the PFF device is collected by the objective, passed through the 50/50 mirror and an emission filter, before finally reaching the camera. The platform part consist of a breadboard on which a device holder is fixed (4), a device holder on which the device is clamped (5), and two translational stages to move the device

independently of the microscope (6). The fluidic part consist of two syringe pumps (7) from Harvard apparatus (11 plus) supplying the device holder via tubes with buffer and sample. In the basic PFF measurements the flowrate at the buffer inlet and the sample inlet are $600\,\mu L/hr$ and $5\,\mu L/hr$ respectively. At these flowrates, the average flow velocity in the broadening segment is 34 mm/s. The device is clamped on the device holder by four screws, to ensure tight connections to the inlet and outlet channels. Mounting the device without creating air bubbles in the system or breaking the device is both time consuming and troublesome, even after much practice. This has motivated a more user-friendly measurement setup described at the end of the chapter before the summary.

The measurement setup in Fig. 2.5 has also been used in the sub-projects: roll-to-roll imprinted PFF devices (Chap. 3), enhancement of separation in PFF (Chap. 4) and DNA analysis utilizing PFF devices (Chap. 6).

2.4.3 Separation measurements

Fluorescence labeled polystyrene (PS) microspheres ranging from 0.26 µm to 2.5 µm in radius were separated. The solid concentration ranged from 0.0001 % w/v to 1.0 % w/v. However, to avoid clogging, the solid concentration of microspheres with a radius of 2.0 µm and 2.5 µm did not exceed 0.5 % w/v.

The measurements revealed two different separation regimes depending on the number of different microspheres sizes in the system and the solid concentration. The two regimes are: 1) polydisperse sample with low solid concentration ($\leq$ 0.05 % w/v) and monodisperse sample with high solid concentration (up to 1.0 % w/v); and 2) polydisperse sample at high solid concentration ($\geq$ 0.1 % w/v). Examples of separation measurements are shown in Fig. 2.6.

The measured values of y' for all measurements as well as the predicted values of the earlier introduced models are plotted in Fig. 2.7, and the experimental values are summarized in Table 2.3. The numerical model was used to convert the measured standard deviation of the sphere positions, $\sigma_{y'}$, to a resolution of their radius, $\delta r_{d,exp}$.

As seen from Fig. 2.7, two separation regimes are clearly visible. At high concentration polydisperse sample the distance y' is larger, compared to monodisperse sample and low concentration polydisperse sample. The exact reason is still not understood. However, since y' is generally larger for polydisperse sample with high solid concentration, it is expected to be because of perturbation of the flow and thereby an interaction between the different microsphere sizes in the pinch segment. Even though the mechanisms in the pinch segment for these samples are highly complex, it is reproducible, and can therefore be used for separation applications. Throughout the study, the polydisperse sample at high concentration was only used to demonstrate the SNP detection application of PFF, otherwise polydisperse sample at low solid concentration as well as monodisperse sample was used in device characterization.

In general it is evident from Fig. 2.7, that the linear analytical model overestimates while the more advanced analytical model underestimates the experimental results. The numerical model gives a qualitatively good description of the low concentration measurements as well as monodisperse measurements. Yet, it is clear that the model

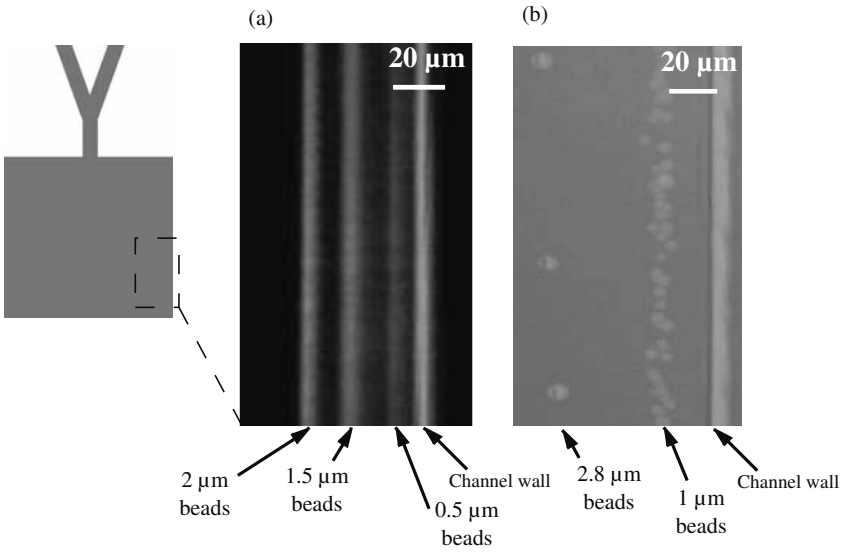

Figure 2.6: Examples of separation in pinched flow fractionation. (a) Separation of microspheres (beads) with a radius of 0.5 µm, 1.5 µm and 2.0 µm at a concentration of 0.01 % w/v. The readout frequency of the camera is low in this image, so the microspheres appear as lines. (b) Separation of microspheres with a radius of 1.0 µm and 2.8 µm at a total solid concentration of 0.01 % w/v. Here the readout frequency of the camera is high, so the microspheres are visible in their spherical shape.

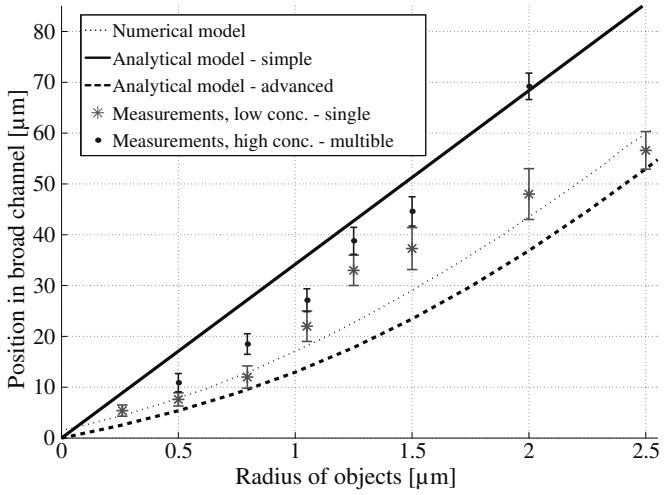

Figure 2.7: Separation measurements in pinched flow fractionation. As seen from the graph two separation regimes exists in PFF. One is for low solid concentration polydisperse sample ($\leq$ 0.05 % w/v) and high concentration monodisperse sample (up to 1 % w/v). The other regime is for high solid concentration polydisperse sample ($\geq$ 0.1 % w/v). In the graph, one numerical and two analytical models are also plotted.

	Low conc./monodisperse				**High conc. polydisperse**		
Radius [μm]	$\mathbf{y'}$ [μm]	$\sigma_{\mathbf{y',exp}}$ [μm]	$\delta\mathbf{r_{d,exp}}$ [μm]	$\delta\mathbf{r_{d,cal}}$ [μm]	$\mathbf{y'}$ [μm]	$\sigma_{\mathbf{y',exp}}$ [μm]	$\delta\mathbf{r_{d,exp}}$ [μm]
0.26	5.4	1.1	0.10	0.10	-	-	-
0.5	7.6	1.3	0.16	0.12	10.9	1.8	0.16
0.75	12.0	2.0	0.26	0.14	18.5	2.0	0.16
1.05	22.0	3.0	0.28	0.20	27.1	2.3	0.18
1.25	33.0	3.2	0.24	0.22	38.8	2.7	0.18
1.5	37.3	4.1	0.32	0.24	44.6	2.9	0.20
2.0	48.0	5.0	0.42	0.32	69.2	2.6	0.16
2.5	56.6	3.7	0.32	0.38	-	-	-

Table 2.3: Separation measurements in pinched flow fractionation for eight different microsphere sizes, ranging from 0.26 μm to 2.5 μm. y' is their center-distance from the channel wall in the broadening segment, $\sigma_{y',exp}$ is the standard deviation of the distance, $\delta r_{d,exp}$ is the measured resolution in the radius, r, and $\delta r_{d,cal}$ is the expected resolution in r. Two different separation regimes were found. In column two to four are measurements with low solid concentration polydisperse sample ($\leq 0.05\,\%$ w/v) or monodisperse sample up to $1.0\,\%$ w/v solid concentration; and in column six to eight are measurements with high solid concentration polydisperse sample ($\geq 0.1\,\%$ w/v).

is too simple to give a good quantitative description. According to the lift force calculation based on the article by Di Carlo et al. [133], the microspheres with radius $\geq 1.05\,\mu m$ should be affected measurably by the lift force. Furthermore the effect increases with increasing radius until the lift force saturates for $r = 2.5\,\mu m$, as seen in Table 2.1. In the measurements with low concentration or monodisperse sample in Fig. 2.7, this tendency is visible. Still, the calculated effect from the lift force does not fully account for the deviation between the numerical model and the measurements, indicating that another force is affecting the microspheres.

Another interesting observation is that measurements with polydisperse high solid concentration samples is better described by the linear model than compared with the two other models. One plausible explanation is that the velocity profile in the pinch segment is perturbed by the spheres towards a flat velocity profile. However, the explanation is most likely more complex. These measurements are indeed motivating for development of more sophisticated models, and could be the starting point of theoretical studies of flow in pinched flow fractionation and other microfluidic systems, in which particles are aligned against a wall.

The experimentally observed resolution in particle radius for low solid concentrations or monodisperse samples with a standard deviation in size of 5 % ranges from 100 nm (r=0.26 μm) to 420 nm (r=2.0 μm), as seen from Table 2.3. Compared to the theoretical expectations, also listed in the table, these are in general larger, up to approximately 50 %. This indicates that an effect besides the size distribution and diffusion is contributing to the broadening of the microsphere position, y'. The deviation follows the deviation between the numerical model and the measurements and is therefore expected to originate from the same effect(s). The lift force could be one of the reasons. The displacement caused by lift forces depends on the time a particle spends in the pinch segment squared, see Eqn. 2.10. So the hypothesis could be tested

by varying the length of the pinch segment and repeat the measurements. The resolution in size of polydisperse high solid concentration samples is approximately constant, 160 nm to 180 nm, and is in general smaller than for low concentrations or monodisperse samples. This is an advantage from a technological point of view. However, it emphasizes the need for more accurate theoretical models. Based on the measurements, a total number of 10 different sizes can be separated in monodisperse and low concentration polydisperse sample and a total number of 11 different sizes can be separated at high concentration polydisperse sample. In addition, it was not possible to separate particles with a radius smaller than 0.26 µm, corresponding to 2.2 % of the pinch segment.

2.4.4 Clogging issues

Clogging, mentioned earlier, is always an issue to be aware of when handling suspensions in microfluidic systems. Clogging is both dependent on solid concentration and particle size. Throughout this study, based on measurements with a solid concentration up to 1.0 % w/v, it was found that the risk of clogging is strongly reduced as long as the radius of the particles does not exceed 25 % of the smallest dimension of the channel. Furthermore, the solid concentration should not exceed 0.5 % w/v for microspheres, at which the ratio between their radius and the smallest dimension of the channel is larger than 0.15.

2.5 A user-friendly device layout

The PFF devices realize reproducible separation as already shown, but the current device and measurement setup require skilled users and are both time consuming and troublesome. The main reason is the mounting step of the device to the holder, where formation of air bubbles and tight clamping without breakage of the device are crucial. This has motivated the development of a user-friendly device and measurement setup where the two flow control units connected to the inlets are exchanged by vacuum, and applied to the outlets. Beside reducing the number of flow control units, a vacuum control system is easier and faster to use. The user only has to fix the device under the microscope e.g. by a vacuum holder, apply a few droplets of sample and buffer at the inlets, and afterwards place a suction disc at each outlet. This applies the vacuum with considerable less hassle. Such a device has been realized by designing the inlet channels to have different hydraulic resistances, ensuring a pinched flow condition when a vacuum is applied to the outlets.

The hydraulic resistance in a straight channel depends on the dimensions of the channel in an analogous way as with electric circuit theory. Different hydraulic resistances in the two inlets can thereby be accomplished by differing their geometries. In the measurements controlled by syringe pumps, the flow rate in the buffer inlet is 120 times larger than in the sample inlet. The ratio of the hydraulic resistances should therefore be 120 or larger to gain the same separation functionality. The large ratio of the flow rates can be accomplished by a short and wide buffer inlet channel and a narrow and long sample inlet channel. In this way a device was designed and fabricated in which the hydraulic resistance in the sample inlet was 135 times larger than that of the buffer inlet. The pinch and broadening segment was similar in dimensions to the previous presented PFF layout but in this case only had one outlet

channel. Separation of 1 µm, 3 µm and 4 µm was demonstrated, with similar results as presented in Table 2.3, for the basic PFF measurement setup. A measurement at the new vacuum driven PFF device only took a few minutes, which is approximately a factor 10 faster than the old system and its usage was demonstrated by untrained users. One drawback of such a vacuum driven PFF device is, however that it is more vulnerable to air bubbles in the system because it is apparently more difficult to suck out bubbles than to push them out. As long as the device materials facilitate wetting by capillary forces, this issue was observed to be only a minor problem.

2.6 Summary

In this chapter an introduction to the theory necessary for flow calculations in PFF is given. Two analytical models from literature, and one numerical model developed in this thesis, are presented. In all of them it is assumed that particles do not perturb the fluid flow or interact with the channel wall and that their center of mass will follow a specific streamline in a laminar flow. As seen from comparison with experimental data, the numerical model gives the best quantitative description. If particles are introduced into the system, the physical complexity is highly increased. According to Di Carlo et al. [133] a lift force will cause pinched microspheres in the pinch segment to migrate away from the channel wall and thereby have a measurable effect on spheres with a radius larger than 1.05 µm. This is observed from measurements with low solid concentration polydisperse sample where particles pass the pinch segment one at the time, or monodisperse sample up to 1 % w/v. It seems that for the largest particles something else in addition to the lift force comes into play. Measurements with high solid concentration (≥ 0.1 % w/v) polydisperse sample reveal another separation regime, where the microspheres where placed further from the wall in the broadening segment. For applications this is an advantage, however in a model perspective this regime is much more complex, motivating for a more in depth theoretical study. In literature, effects on separation from the solid concentration have not been studied. However, according to measurements presented in this chapter, the solid concentration is a significant aspect of the separation in PFF. Throughout the characterization measurements, up to 8 different sizes were separated, which is a factor of two more compared to previously published results of PFF. In addition, the separation was observed to be stable and reproducible.

The highest detection resolution of separation for samples with no distribution in size in the basic PFF measurements was calculated to range from 13 nm ($r = 2.5$µm) to 62 nm ($r = 0.26$µm). The measured resolution of low solid concentration polystyrene microspheres suspensions with a Gaussian size distribution and a standard deviation of 5 % was found to range from 100 nm (r = 0.26 µm) to 420 nm (r = 2.0 µm). The calculated resolution for the same sample and flow settings is up to 50 % smaller. Conclusively, samples with well defined size are necessary for a high resolution in PFF. Even though the highest theoretical resolution, $\delta r_{d,h}$, has not been realized, the values indicate that micro-scale PFF has the potential for nano-scale resolution. Using the proposed linear analytical model it is predicted that the separation resolution can be increased by increasing the ratio between the width of the broadening and the pinch segment (w_b/w_p). This is the motivation behind the work of an enhanced PFF layout presented in Chap. 4.

Finally, a chip design enabling a more simple and user friendly measuring setup in regards to flow control is presented. Here the hydraulic resistance in the inlet channels of PFF is designed so that particles are pinched and separated by applying vacuum at the outlets. This is an important step towards a PFF-based LOC device for POC applications.

Chapter 3

Fabrication of micro and nanofluidic devices

Many LOC systems are currently meeting the industrial requirements regarding stability, reliability and usability. However, a cheap and high volume fabrication method is one of the remaining bottlenecks to be addressed before the systems will experience a massive commercialization in price sensitive markets such as POC diagnostics. Today, the most promising candidates with respect to high volume and low price fabrication, are polymer replication techniques, which are summarized in Chap. 1, Table 1.1. Presently, the most promising commercially available candidates within microfluidic devices are hot embossing, in thin films denoted nanoimprint [135], and μ-injection molding [8]. Both techniques are well suited because: 1) they allow flexibility in the device material, 2) they enable all polymer devices, which makes the material cost low, and 3) the techniques have high pattern reproduction fidelity, which is important when fabricating microfluidic channels ranging from micrometers to millimeters in the same device layout. Nanoimprint, being wafer-based compared to μ-injection molding, enables easier integration with other wafer-based LOC units. In addition, nanoimprint is available in the cleanroom at DTU. Conclusively, nanoimprint lithography (NIL) is chosen as the central fabrication process.

In this chapter, all major fabrication techniques used throughout the thesis for stamp fabrication and in general for silicon and silicon dioxide devices are summarized. References to more comprehensive descriptions are also given. The emphasis of the chapter is on the main fabrication technique, NIL, where aspects such as stamp fabrication, materials and the imprint process are detailed — including the fabrication process of nanoimprinted pinched flow fractionation (PFF) devices. In the second half of the chapter an extreme high volume fabrication technique of polymer LOC devices using roll-to-roll (rtr) methods, developed in this thesis, is presented. Here PFF is used as a demonstrator LOC device.

3.1 Conventional fabrication techniques

Conventional cleanroom processes such as UV-lithography, dry etching, oxidation, metal deposition and electron beam lithography have been used in projects dealing with stamp fabrication, nano-scale PFF (nanoPFF), integration of an optofluidic mi-

Process name	Project name	Chap
UV-lithography	Stamp	3 – 6
	X-ray platfrom	8
Dry etch		
Reactive Ion Etch (RIE)	NanoPFF	7
Deep Reactive Ion Etch (DRIE)	Stamp	3 to 6
	X-ray platform	8
Oxidation	Stamp	3 – 6
	NanoPFF	7
Al deposition	OFMPFF	5
Electron beam lithography	NanoPFF	7
	OFMPFF	5
Powder blasting	Fluid access holes	All

Table 3.1: List of the main conventional cleanroom processes, projects in which they are applied and the relevant chapters.

croscope in PFF (OFMPFF) and microfluidic x-ray platforms. Process details, such as machines and parameters, are included in the relevant chapters describing each of the projects. In Table 3.1, the main fabrication processes are listed, along with the projects in which they have been used and the relevant chapters. For comprehensive descriptions of these processes, the reader is referred to [136, 137, 138].

Electron beam lithography (EBL) is a highly sophisticated process specialized for fabrication of sub-100 nm features. The resolution of EBL is limited by forward scattering of electrons in the electron-beam-sensitive resist and backward scattering in the substrate material. Both effects are known as proximity effects and are further described in [137]. However, in this thesis the smallest features fabricated by EBL are 480 nm in 450 nm films (nanoPFF), and slight broadening of the structures is not critical. Optimization, by implementing dose-experiments was therefore not necessary and standard e-beam settings were used.

3.2 Nanoimprint Lithography

The thermal nanoimprint lithograpy process is sketched in Fig. 3.1. A hard stamp is placed in contact with the moulding material (thermoplastic or thermosetting polymer), placed on top of a substrate (Fig. 3.1(a)). The temperature is raised to a temperature well above the glass transition temperature, T_g, and the stamp and substrate are then pressed together for sufficient time until the polymer has filled-up the stamp cavities (Fig. 3.1(b)). After cooling below T_g the stamp and substrate are demolded and the pattern of the stamp is transferred into the molding material, leaving a residual layer under the stamp protrusions (Fig. 3.1(c)). Nanoimprint lithography is a parallel fabrication process, which enables cheap and high volume production. As seen in Fig. 3.1, the process is carried out with flat surfaces and is therefore denoted planar thermal NIL in the following.

When fabricating micro- or nanofluidic structures, the residual layer homogeneity is not of interest as in regular NIL, where the imprinted structures are used as a mask

Figure 3.1: The principle of Nanoimprint Lithography (NIL). The pattern of a stamp is transferred into a molding material (thermoplastic or termosetting polymer) at elevated temperature and pressure.

for further processing. For fluidic features, it is important that the stamp is perfectly replicated and that the surface of the imprint is flat, enabling sealing of the channel structures in a later polymer-polymer bonding step.

3.2.1 Stamp fabrication

The success of nanoimprint largely relies on the quality of the stamp, as the imprinted structures are limited by its resolution. The stamp material must be rigid to avoid deformation of the protrusions at high pressure during the imprint and have a low thermal expansion coefficient (TEC) to ensure minimal effect on the stamp protrusion at the elevated temperatures during imprint. In planar NIL, stamps are most often made in silicon of silicon dioxide because of their mechanical properties and because of the large variety of fabrication tools available for these materials. However, elastomeric and metallic stamps have also been used [139]. In this thesis silicon is used as stamp material at planar imprinting. The TEC of silicon is approximately $2.6 \cdot 10^{-6}\,\mathrm{K}^{-1}$ [137], so for imprints 130 °C above the demolding temperature, as it is the case in this thesis, stamp features will expand 0.3 ‰.

Another crucial aspect of stamps for NIL are adhesion challenges. To be able to separate the stamp from the imprinted structures, the adhesion between the moulding material and stamp must be smaller than the adhesion between substrate and moulding material. The use of an intermediate antisticktion layer (ASL) on the stamp is commonly used to lower the surface energy of the stamp and thereby overcome the adhesion issue. Several approaches have been tried [139], but the most common ones are plasma deposited Teflon-like ASLs [140] and self-assembling ASLs [141]. Self-assembling ASL consisting of chlorosilane-based groups, such as F_{13}TCS [141] and OTS [142], have gained much attention in nanoimprint. These are covalent bonded in a monolayer (thickness $\sim 3\,\text{Å} - 22\,\text{Å}$) on silicon and silicon dioxide surfaces. Because of their covalently bonds and monolayer thickness, these materials have a high lifetime (> 1000 imprints) with an insignificant disturbance to the stamp features.

Stamp fabrication in this thesis
Throughout the work with planar nanoimprint the structures on the silicon stamp are defined by conventional UV-lithography. The pattern is then transferred into a 4" single polished (100) silicon wafer by deep reactive ion etch (DRIE) (machine: Inductively Coupled Plasma etcher from Surface Technology Systems), utilizing a slightly modified Bosch process [143], with parameters as listed in Table 3.2. This process gives vertical sidewalls with approximately 50 nm surface roughness, which

	Etch		Passivation	
Power	16 W		0 W	
	Flow(Sccm)	Tol.(%)	Flow(Sccm)	Tol.(%)
C_4F_8	0	5	120	75
SF_6	260	75	0	5
O_2	26	75	0	5

Table 3.2: Parameters used in the DRIE process step for PFF stamp fabrication.

is still not acceptable, since sidewalls with very low roughness are essential for the NIL process, to ensure release during de-molding. A thermal wet oxidation (1000 °C, 90 min) combined with a buffered hydrofluoric acid etch reduce any roughness's from the DRIE process to 15 nm. An example of a PFF stamp taken at the pinch segment is shown in Fig 3.2(a). This NIL stamp fabrication scheme is developed by Nilsson et. al [144]. Finally, the stamp is coated with a monolayer of heptadecafluoro-1,1,2,2-terrahydrodecyltrichlorosilane(FDTS) (machine: MVD 100 Molecular Vapor Deposition) working as an ASL. Stamps coated with this ASL have been used for above 100 imprints with no visible degradation. The stamp fabrication is described in more detail in [145].

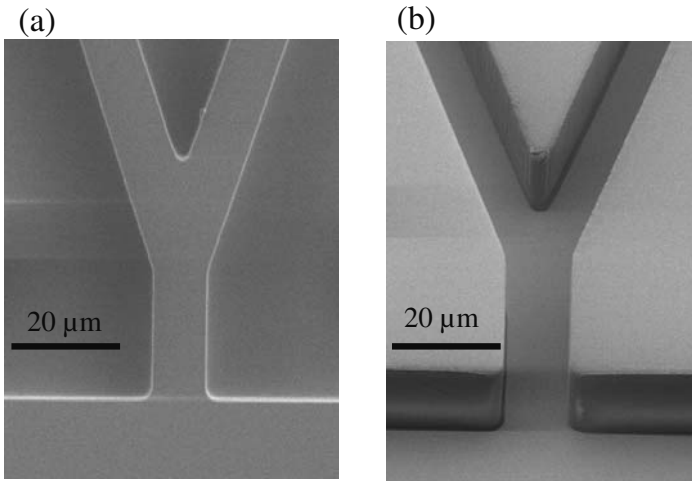

Figure 3.2: a) Silicon pinched flow fractionation stamp seen from above. b) A slightly tilted imprinted Topas® device. Both images are of the pinch segment.

3.2.2 Materials

In thermal NIL, thermosetting and thermoplastic materials are used as moulding layers. These polymer materials consist of long chains of monomers, typically based on a carbon backbone. A thermosetting polymer is viscous at room temperature and solidifies irreversibly at a specific elevated temperature. The mechanical properties of thermoplastics on the other hand, can be changed reversibly and are characterized by the glass transition temperature, T_g, and the melting temperature, T_m.

Two thermoplastics have been used: cellulose acetate (CA) for rtr imprint, which is described later, and a Topas® Grade 8007 based product called mr-I T85 from Micro Resist technology (GmbH, Berlin, Germany, www.microresist.de) for planar nanoimprint. Topas® is a cyclic olifin copolymer (COC), highly suitable for LOC applications, compared to conventional thermal nanoimprint polymers such as poly(methyl methacrylate) (PMMA). Topas® has a low water absorption ($< 0.01\%$), is chemically resistant to hydrolysis, acids and organic polar solvents [146] (all relevant in biological applications) and has a high optical transparency — including UV and visible light [146, 147]. In addition, it has a low surface energy (low adhesion to the stamp) and the glass transition temperature can be tuned, by varying the content percentage of the two copolymer constituents, norbornene and ethylene. This, together with the fact that Topas® is a thermoplast, makes it ideal for thermal NIL.

Below T_g, the carbon-based chains in a thermoplastic are entangled and even interconnected. The material, at this state is solid and fully elastic. As the temperature increases above T_g, Van der Walls interactions and entanglements of the chains are reduced. This enables large deformations of the polymer chains, yet in a viscoelastic rubber fashion. Imprinting slightly above T_g, causes a large stress build-up during the deformation process, resulting in recovery of the polymer after demoulding, so the imprinted structures do not have the shape of the stamp [139]. Consequently, the temperature is typically raised even further, up to above T_m. At this temperature the chains are able to move independently, and the polymer can be irreversibly deformed. An imprint temperature of 70°C to 80°C above the glass transition temperature is considered suitable.

For viscous liquids, as is the case for thermoplastic polymers under imprinting, the key parameter in regards to flow behavior is the viscosity. The viscosity mainly depends on the shear rate, $\dot{\gamma}$, temperature, T and molecular weight, M.

In the case of Topas® Grade 8007 it has been demonstrated that the viscosity as a function of shear rate can be described by the Carreau model [148], given in Eqn 3.1.

$$\eta(\dot{\gamma}) = \eta_0(1 + (\lambda\dot{\gamma})^2)^{(n-1)/2} \tag{3.1}$$

Here λ is a characteristic time and n is the power law index. These values are experimentally found in [148]: $n = 0.72$, η_0 is found to be $2.16 \cdot 10^4$ Pa s, $9.5 \cdot 10^3$ Pa s and $3.6 \cdot 10^3$ Pa s while λ is found to be 4.4 s, 1.8 s and 0.9 s at 170°C, 180°C and 200°C, respectively. η_0 is the zero shear viscosity, which is defined as:

$$\eta_0 = \lim_{\dot{\gamma}\to 0} \eta(\dot{\gamma}) \tag{3.2}$$

In general the viscosity dependence on temperature, T, of thermoplasts is given by the William-Landel-Ferry (WLF) equation as:

$$\eta_0(T) = \eta_0(T_0) \exp\left(\frac{-C_1(T - T_0)}{C_2 + T - T_0}\right) \tag{3.3}$$

Where the reference temperature, T_0, and viscosity, $\eta_0(T_0)$, are often set to the values of the glass transition temperature, C_1 and C_2 are constants which are specific for a given polymer. C_1 and C_2 can be found for mr-I T85 using the zero shear data from

[149] to be 16.66 and 85.79 K respectively.

Finally, the zero shear viscosity depends on molecular weight, M, as[139]:

$$\eta_0 \propto \begin{cases} M & M < M_c \\ M^{3.4\pm0.2} & M > M_c \end{cases} \tag{3.4}$$

Here M_c is a certain critical molecular weight, where polymer entanglement has little effect. M_c has has been measured for mr-I T85 to be 31.6 kg/mol [149].

The above equations, Eqn 3.1, 3.3 and 3.4, enable a description of the viscosity of mr-I T85 (Topas® Grade 8007), and thereby knowledge to predict flow behavior during imprint in the material. These equations can also be used for other thermoplastic materials.

3.2.3 The imprint process

The main challenges of thermal nanoimprint have to do with deformation and removal of moulding material during imprint. This sets up limitations to the imprint time and sizes of the stamp protrusions. Contrary to many other lithography techniques, large features in the 100 µm range are more problematic to produce than nano-scale features due to excess material flow. To get an estimate of the time it takes to imprint the stamp, a simple model, describing squeeze flow, for the viscous flow of a polymer melt during imprint is introduced here and derived in [150]. A stamp with rectangular cross-sectional protrusions of width w, height h_r and length L, is imprinted into a thermoplastic polymer layer of initial thickness h_0, as illustrated in Fig. 3.3.

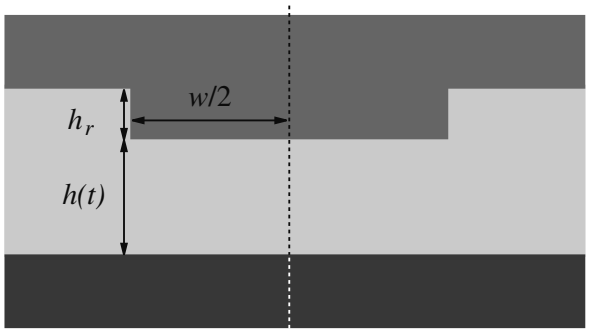

Figure 3.3: Model system describing the flow process during imprint of rectangular stamp protrusions. The cross-section of a stamp is shown in the figure.

To solve the Navier-Stokes equation (described in Chap. 2) analytically, which is the first step towards the solution, the following assumptions are made:

- The fluid is incompressible
- Body forces are neglected
- $L >> w >> h(t)$

- Quasi-stationary flows ($\eta(\dot{\gamma}_0) = \eta_0$)
- No-slip boundary conditions

The resulting 2-dimensional velocity field as a function of protrusion force, in between protrusion and substrate, is then integrated over space to find the imprint time, t_{imp}, as a function of the protrusion force, as given in Eqn. 3.5.

$$t_{imp} = \frac{\eta_0 L w^3}{2F}\left(\frac{1}{h(t)^2} - \frac{1}{h_0^2}\right) \tag{3.5}$$

Here $h(t)$ is the residual layer thickness and F is the imprint force under each stamp protrusion.

If effects such as stamp bending, resulting in uneven pressure at different protrusions are ignored, the imprint force of the entire stamp, F_{tot}, can be assumed evenly distributed and F is then estimated as in Eqn. 3.6.

$$F = F_{tot}\frac{A}{A_{tot}} \tag{3.6}$$

Here A is the area of the protrusion and A_{tot} is the area of the total number of protrusions.

If the total polymer volume before and after imprint is assumed constant, the residual layer thickness, when the stamp is fully imprinted, $h(t) = h_f$, where h_f is the final residual layer thickness, can be expressed as in Eqn. 3.7.

$$h_f = h_0 - h_r(1 - \nu) \tag{3.7}$$

Here $\nu = A/A_{stamp}$ is the protrusion coverage and A_{stamp} is the total area of the stamp.

The above equations can be used to estimate the imprint time it takes for a PFF stamp to be fully imprinted, $h(t) = h_f$, in mr-I T85. The imprint time of the broadening segment of the PFF devices is estimated in the following. These are 1.1 mm long ($L = 1.1\,\text{mm}$), 400 µm wide ($w = 400\,\mu\text{m}$) and 12.5 µm high ($h_r = 12.5\ \mu\text{m}$). The initial polymer thickness is 20 µm ($h_0 = 20\,\mu\text{m}$), the total area of the stamp protrusions is $12.04 \cdot 10^6\ \mu\text{m}^2$ ($A_{tot} = 12.04 \cdot 10^6\ \mu\text{m}^2$), the protrusion coverage is $1.53 \cdot 10^{-3}$ ($\nu = 1.53 \cdot 10^{-3}$) the force applied between the 4 inch stamp and substrate is 15 kN and the zero shear viscosity is $3.92 \cdot 10^4$ Pa s ($\eta_0 = 3.92 \cdot 10^4$ Pa s) at 190 °C, calculated with the WLF equation ($C_1 = 16.66$, $C_2 = 85.79$ K, $T_0 = 120\,^\circ$C and $\eta_0 = 7 \cdot 10^7$ Pa s). Inserting these values in Eqn. 3.5, 3.6 and 3.7 the imprint time is estimated to 91 s, which is less than the imprint time during fabrication (10 min), suggesting a shorter imprint time could be used. However, throughout the measurements it was observed that incomplete filling of the stamp cavities occurred when the imprint time was less than 5 min. The difference in the necessary calculated and observed imprint time originates from the difference in the stamp structure. Only the broadening segment is included in the calculation and not the full device layout as in the real imprint. For more accurate imprint models, including all device structures, numerical finite element methods [151] or a soon-to-be available commercial software from Cognoscens [152] can be applied.

3.2.4 Planar fabricated pinched flow fractionation devices

Devices are fabricated in a thermoplastic polymer (mr-I T85-20XP, $T_g = 85\,^{\circ}\mathrm{C}$) from Micro Resist Technology (GmbH, Berlin, Germany, www.microresist.de) using single step NIL.

A 20 µm thick mr-I T85-20XP layer is spin coated on a 4" single polished (100) silicon wafer at 3000 rpm. The device layout is imprinted into the mr-I T85-20XP layer for 10 min at 190 °C and 1.9 MPa (15 kN) (machine: EVG 25 HE), using the silicon stamp described earlier. After imprinting, the imprint and stamp are cooled below 70 °C and separated. Inlet and outlet holes are powder blasted in the imprint, which is afterwards cleaned in deionised water. Finally a borofloat glass wafer is bonded to the imprinted structures for 10 min at 70 °C and 1.9 MPa (15 kN), using a 300 nm layer of Topas grade 9506 spin coated on the borofloat glass wafer working as a bonding layer [153]. A scanning electron microscopy (SEM) picture of the imprinted device is shown in Fig. 3.2(b). In this image it is seen that the channel walls are vertical and very smooth. The surface roughness of the vertical walls is 15 nm, the same as for the stamp. This fabrication process is described in further detail in [145].

The long term structural stability of the planar nanoimprinted devices was investigated. Devices were imprinted as described above. Profilometer scans at the broadening segment of PFF devices 10 min after imprint and again after 3 months revealed a recovery of only 8 nm. The bottom of the imprinted channels was found to curve slightly upwards - into the channels. Ten minutes after the imprint, a difference in height between the center of the channel and at the sidewalls was measured to be 86±2 nm. Compared to the total channel height of 12.5 µm this is only 0.7 % and the recovery is 0.06 %, which is negligible with respect to the device functionality.

3.3 Thermal roll-to-roll nanoimprint

In this section a high volume replication technique for polymer microfluidic LOC systems based on thermal roll-to-roll (rtr) methods is demonstrated. Even though planar nanoimprint offers high volume production, rtr methods have potential of much larger volumes as described in Chap. 1. As discussed in Chap. 1, deep channels ($> 1\,\mu\mathrm{m}$) which is usually the case for LOC, represents one of the most challenging aspects in rtr imprint due to recovery of the material profile in the channel after imprint. Optimization of the fabrication parameters to avoid recovery in the rtr imprints is described in this section with focus on the imprint temperature.

As a demonstrator LOC device pinched flow fractionation (PFF) was chosen. The rtr imprinted devices were compared with devices fabricated by planar nanoimprint. The basic PFF layout, described in Chap. 2, was used in the study, shown in a rtr fabricated device in Fig. 3.5(a). In this layout, the device channels range from 11.7 µm (pinch segment) to 400 µm (broadening segment) in width and are 12 µm deep.

3.3.1 Principle of roll-to-roll imprinting

Roll-to-roll is a continuous fabrication technique, in which an imprint roll with a structured surface or thin metal film, mechanically attached to the roll, is heated and pressed

against a backing roll at room temperature while a thermoplastic film is introduced in between the two rolls. The production volume depends on the roll rotation speed, the size of the devices and the width of the roll. The only part of the thermoplastic film that is heated is the area where the film is in contact with the imprint roll, which is the width of the roll times the contact length. In this work the contact length is approximately 4 mm. The reason that features can be imprinted much faster in thermal rtr imprinting compared to planar thermal nanoimprint is due to the small contact area. Thus, the imprint pressure can be much larger, than what can be accomplished with planar nanoimprint. Because rtr imprinting is continuous, it can also be combined with up- or down-stream continuous fabrication methods, such as rtr lamination of imprinted microchannels. This is the reason that rtr imprinting has the potential of being superior to current state-of-the-art LOC fabrication tools, such as planar NIL and μ-injection molding, when it comes to the production volume of sealed microfluidic devices.

The rtr fabrication technique presented here is comprised of two parts: rtr thermal nanoimprint (rtrNI) [35, 154] to imprint channel structures into a polymer film and rtr lamination [155] to laminate another polymer film on top of the imprinted fluidic devices. In addition, rtr reverse gravure (RG) [155, 156] is used to coat a smooth material layer on top of the lamination film in order to increase the bonding strength. The fabrication process is illustrated in Fig. 3.4(a). A cross-section of the fabricated channels is shown schematically in Fig. 3.4(b) and an imprinted device in Fig. 3.4(c).

3.3.2 Materials and machine settings

The polymer film used throughout the study is a 95 μm thick and 50 mm wide cellulose acetate (CA) film (P20 from Clarifoil), and the adhesion material is Topas® Grade 9506 (from Topas Advanced Polymer). The Topas® was dissolved in sec-buthylbenzene to a weight percentage (wt%) of 5.7 in order to obtain coating layers of 300 nm in thickness. A rtr RG machine (Minilabo from Yasui Seiki Co.) was applied to coat the 300 nm layer of Topas® on the CA film at a speed of 0.5 m/min using a rod with 32 lines/cm. Cellulose acetate is well suited for thermal rtr imprinting because of its low surface energy (low adhesion to the stamp). Cellulose acetate is not as well suited for LOC applications as Topas® due to its larger water absorption (10 %) and poor chemical resistance to acids and organic polar solvents. Still, it is usable for some LOC applications. In addition, CA had already been frequently used in the rtr machine and is very inexpensive. Cellulose acetate was therefore chosen as a demonstrator material.

PFF devices were patterned into the CA film, using a custom designed rtrNI machine [35], at speeds between 0.1 m/min and 0.2 m/min (minimum of the machine) corresponding to an imprint time of approximately 1.2 s. The pressure between the imprint and backing roll at the contact area was 136 MPa. During imprint, the temperature of the imprint roll was kept at 115 °C and the backing roll at 25 °C. 100 μm thick nickel (Ni) stamps, fabricated by electroplating on a silcone template (RTV630 from GE Silicones) with a 100 nm conductive Au layer (deposited with an Edwards Auto306 system at DC power), were used as shims. The silicone template was made by casting, using a silicon stamp from planar NIL as master. Ni was electroplated onto the Au coated silicone template in a 350 L Ni-electroplating cell (Coburn Corporation) at continuous filtering and at 45 °C. Information on the electrolyte and electrical settings are given in Table 3.3. Detachment of the electroplated Ni-shim was done

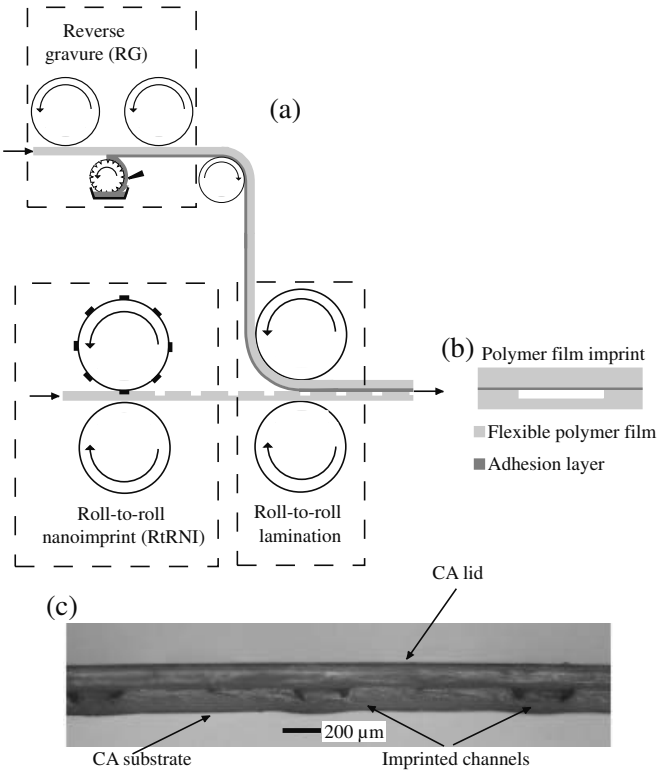

Figure 3.4: a) Principle of roll-to-roll fabrication of microfluidic devices including reverse gravure (RG), roll-to-roll nanoimprint (rtrNI) and roll-to-roll lamination. b) Cross-sectional illustration of an rtr fabricated microfluidic channel. The adhesion layer is added to improve the bonding strength. c) Cross-sectional image of imprinted devices. Six pairs of inlet channels are visible in the image. However, the adhesion layer is too narrow to be seen.

manually. Each shim, including 6 devices, was mechanically attached to the imprint roll.

The imprinted CA film and the Topas coated CA film were bonded at 80 °C at a speed of 0.2 m/min (minimum of the machine). The applied pressure between the two laminating rolls was set to the minimum of the rtr laminator (Eagle 35 from GBC), below 0.1 MPa. After lamination, the devices were diced out and liquid access holes to the microchannels were drilled with a 1 mm glass drill.

3.3.3 Fabrication results

The fabrication line for making PFF devices was optimized for a production volume of 360 devices/hr, approximately 180 times faster compared to the planar imprint process described earlier. At this production volume, the cost per device, including material and machine usage, is approximately 0.5 Euro, i.e. 100 times cheaper than the planar process. To evaluate the fabricated rtr PFF devices they have been benchmarked, in regards to imprint quality and separation performance, against PFF devices with the

Electrolyte	Nickel chloride	10 g/l
	Nickel content	80 g/L
	Boric acid	38 g/L
	pH	4.2
Electrical conditions	Current density	2–3 A/dm^2

Table 3.3: Process parameters for nickel electroplating.

same dimensions but fabricated by planar thermal NIL. A picture of a rtr fabricated device, before access holes were drilled, is shown in Fig. 3.5(a).

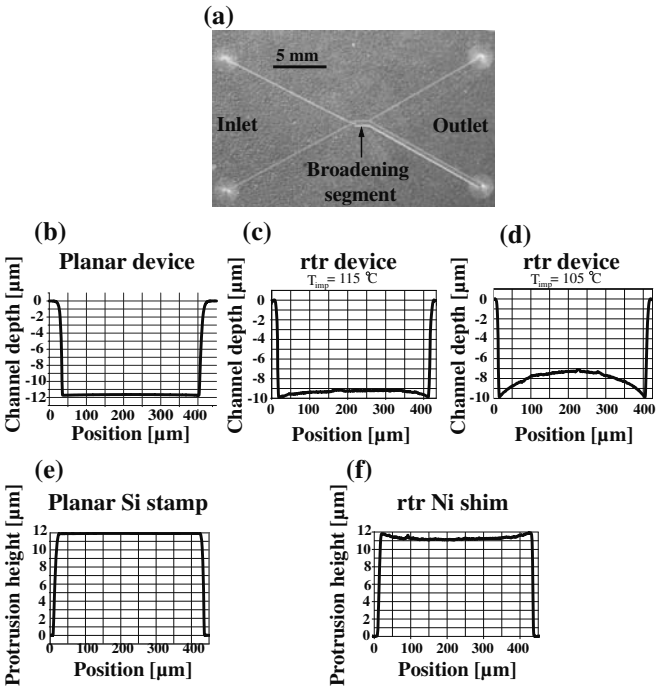

Figure 3.5: (a) Image of a roll-to-roll fabricated pinched flow fractionation device. Surface scans of the broadening segment in a PFF device fabricated by planar (b) and roll-to-roll thermal nanoimprint (c+d) at 115 °C and 105 °C respectively. (e+f) Surface scan of the broadening segment in the Si stamp and Ni shim that was used to imprint the PFF devices, which are scanned in (b) and (c+d).

Cross-sectional profilometer scans of the microfluidic channels in the planar (Fig. 3.5 (b)) and optimized rtr (Fig. 3.5(c)) fabricated devices as well as the Si stamp (Fig. 3.5(e)) and Ni shim (Fig. 3.5(f)) used to imprint the devices respectively, showed good replication in both cases. As seen from the scan of the rtr fabricated device and the Ni shim, a small curvature in the protrusions of the Ni shim is transferred to the bottom of the channels in the rtr fabricated devices. However, this curvature is small and does not, as will be shown later, effect the flow in the device for a measurable scale.

During optimization of the rtr fabrication, the imprint temperature was varied from 90 °C to 125 °C. The glass transition temperature (T_g) of CA is 120 °C. It was evident during optimization that the temperature must be close to T_g in order to avoid any significant recovery of CA. As an example, a cross-sectional scan from the broadening segment in a device, imprinted at 105 °C, is shown in Fig. 3.5(d) and compared to an imprint at 115 °C in Fig. 3.5(c). It is evident that recovery effects become visible as the imprint temperature is below 115 °C. Due to stretching of the CA film at imprint temperatures above T_g, and thereby deformation of the imprinted devices, 115 °C was chosen.

3.3.4 Separation results

In all separation measurements, fluorescent microspheres (from Thermo scientific) were suspended in a carrier buffer consisting of 0.001 % w/w Triton X100 in MilliQ water. The microsphere concentration was 0.01 % w/v. The microsphere solution was introduced into the PFF devices from the sample inlet and carrier buffer without microspheres from the buffer inlet (see Fig. 3.6(a)). The flow rates in the sample and buffer inlet channels were 5 µL/h and 600 µL/h respectively. Flowrates were controlled by syringe pumps (11Plus from Harvard Apparatus).

Separation measurements in the rtr fabricated PFF devices including microsphere radii ranging from 0.26 µm to 2.5 µm, proved similar in separation functionality as compared to the planar thermal NIL devices described in Chap. 2. An example of separation of 0.5 µm and 1.5 µm fluorescent polystyrene microspheres in planar and rtr fabricated devices is shown in the microscope images in Fig. 3.6(b) and 3.6(c), respectively. It is seen from the microscope images in Fig. 3.6, that separation was achieved in both the planar and rtr fabricated devices. The distance from the wall in the broadening segment to the 0.5 µm and 1.5 µm microspheres is 7 µm and 34 µm respectively in the planar devices and 6 µm and 35 µm respectively in the rtr devices. The difference in the measured positions is within the standard deviation, which ranged from 1.3 µm to 4.1 µm.

3.3.5 Outlook

In this section three different machines were used, one for each of the rtr steps. However, all the steps can, with slight machine modifications, be integrated in the custom designed roll-to-roll nanoimprinting machine. This will allow for a fabrication line which requires less interaction with the polymer films and can produce higher volumes. For industrial production this will be a necessary improvement. Another obvious addition to the technique presented in this section is coating of an additional imprint polymer, with a glass transition temperature lower than that of CA, on top of the substrate CA film. In the light of this, a wide range of materials with different properties can be applied, which is highly desirable for the bio-medical industry.

3.4 Summary

The conventional cleanroom processes used throughout the projects are summarized and addressed in the relevant chapters. The first emphasis of the chapter is on the main fabrication technique of this thesis, namely nanoimprint lithography, which was

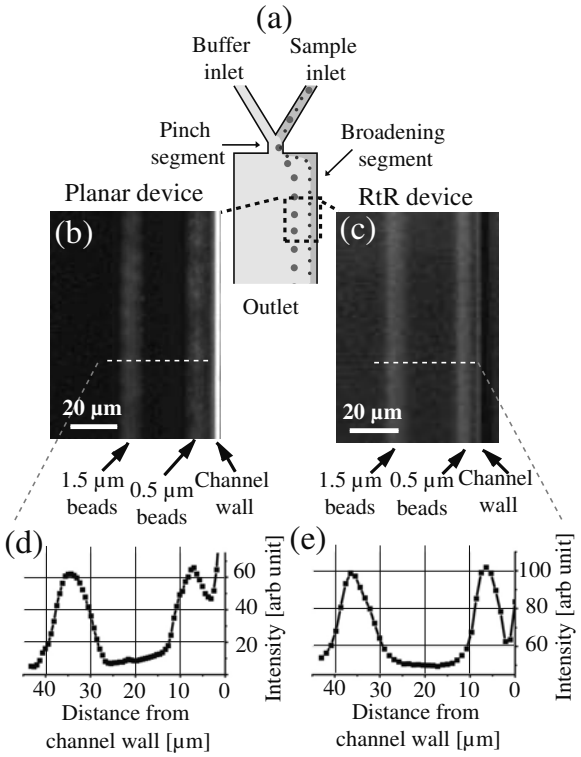

Figure 3.6: (a) Illustration of the separation principle in pinched flow fractionation (PFF). (b+c) Images of 0.5 µm and 1.5 µm (radius) fluorescently labeled polystyrene microspheres (beads) separated in a PFF device fabricated by planar and roll-to-roll thermal nanoimprint respectively. (d+e) Intensity scan perpendicular to the flow direction of the separated microspheres.

used to structure micro-scale pinched flow fractionation devices. Here, aspects such as stamp materials and fabrication, imprint materials and the imprint process itself are discussed, with a focus on silicon stamps and a thermoplastic material called mr-I T85 as they were used in this thesis.

An extreme high volume fabrication process for polymer LOC devices based on roll-to-roll methods has also been introduced and demonstrated. Functional microfluidic separation devices, relying on pinched flow fractionation, were roll-to-roll fabricated in a cellulose acetate (CA) film at a volume of 360 devices/hr and a cost of approximately 0.5 euro/device. The manufacturing process consists of two different steps: 1) roll-to-roll thermal nanoimprint for printing the microchannels into a CA film and 2) roll-to-roll lamination for bonding another CA film onto the imprinted film, thereby sealing the microchannels. Reverse gravure coating was used to apply an adhesive polymer onto the CA lid film before roll-to-roll lamination. This was done to increase the bonding strength. Through optimization of the fabrication process it was found that the imprint temperature must be as high as possible to avoid recovery effects, but not equal to or higher than the glass transition temperature of the CA (120 °C) to avoid film stretching. The optimal temperature was found to be 115 °C. The functionality of

the devices was demonstrated by separation of fluorescent polystyrene microspheres. An example with 0.5 µm and 1.5 µm microspheres was shown.

Chapter 4

Enhancing the separation in pinched flow fractionation

In micro and nanofluidic separation, the success criteria are stability, reliability and high separation resolution. Here, motivated to achieve a high separation resolution towards nano-scale separation of particles by micro-scale structures, a method to enhance the separation in PFF is demonstrated. An additional motivation exists to enable this enhancement without the need for complex functionality nor an increase in microchannel area. Both of these ensure compatibility with the high volume fabrication method: thermal roll-to-roll (rtr) imprinting. Large channel dimensions (width > 400 μm) adds issues with polymer flow and stamp bending. The enhancement method presented here is compatible with rtr fabrication, contrary to previous suggestions from literature, as mentioned in Chap. 1.

In this chapter, the principle of the proposed enhancement method is presented along with one analytical and one numerical model. Afterwards, the device layouts are described and benchmarked against the basic PFF layout (Chap. 2). Finally the work is summarized. The experimental results presented in this chapter are also published in [127].

4.1 The principle of enhanced pinched flow fractionation

The enhancement method does not involve any additional external forces or mechanisms; simply, it involves introducing a snake-like structure in the broadening segment of the PFF layout. The enhanced PFF (EPFF) device layout is shown in Fig. 4.1 together with the basic PFF layout. The part of the broadening segment to the left of the snake-like structure is denoted the sink segment and the part to the right is denoted the enhancing segment. The ratio of hydraulic resistances between these two parts ensures that only fluid containing particles flows through the enhancing segment. As the fluid and particles move from the narrow into the wide part of the enhancing segment, the distance between the streamlines (trajectories of different sized particles) is amplified. By expanding distances primarily in the part of fluid that contains particles and not in the entire fluid as in PFF, the enlargement and thereby separation of

particles can be increased. The simple layout of EPFF facilitates high volume imprint techniques such as thermal roll-to-roll imprint, described in Sec. 3.3.

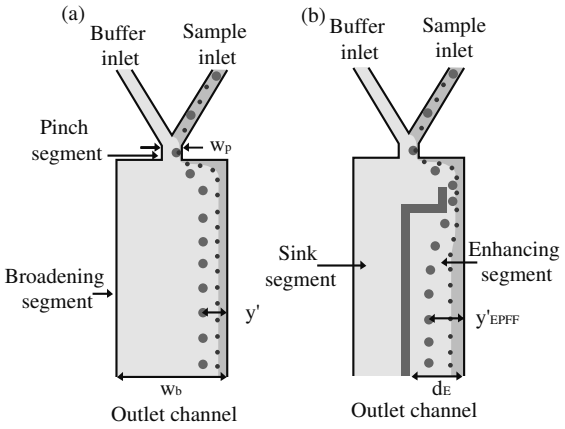

Figure 4.1: The principle of (a) Pinched Flow Fractionation (PFF) and (b) Enhanced Pinched Flow Fractionation (EPFF). Suspended particles are aligned (pinched) against a wall in the pinch segment and separated as they move into the broadening segment due to expansion of the laminar flow sheet. In EPFF the separation is amplified by expanding the part of flow sheet that contains particles.

Using the same assumptions as in Eqn. 2.7 Chap. 2, which describes the particle position in the broadening segment in PFF, a simple model can be derived for the EPFF device, relating the distance from the center-of-mass of a particle to the channel wall in the wide part of the enhancing segment, y'_{EPFF}, and the radius of the particle, r.

From the Hagen-Poiseuille law and basic addition of hydraulic resistance in parallel channels [129], a relation between the total flow rate in the enhancing segment, Q_E, and the total flow rate in the device, Q_{tot}, can be found, see Eqn. 4.1.

$$\frac{Q_E}{Q_{tot}} = \frac{\frac{\Delta p}{R_E}}{\frac{\Delta p}{\left(\frac{1}{R_s}+\frac{1}{R_E}\right)^{-1}}} = \frac{1}{\left(\frac{R_E}{R_s}+1\right)} \tag{4.1}$$

Here Δp is the pressure difference between the entrance and exit point of the snake-like structure in the broadening segment, R_E is the total resistance of the enhancing segment and R_s is the total resistance of the sink segment.

In the above calculation it is assumed that the flow is laminar and the pressure drop across the sink and enhancement segment is the same. A consequence of laminar flow is that the flow rate in the part of the pinch segment from the channel wall to the point corresponding to the radius of a particle, $Q_p(r)$, must equal the flow rate in the wide part of the enhancing segment from the corresponding channel wall to the center-position of the particle, $Q_E(y'_{EPFF})$, see Eqn. 4.2.

$$Q_p(r) = Q_E(y'_{EPFF}) \tag{4.2}$$

The above analysis is generally valid for a Poiseuille flow. As a first approximation and to simplify the calculation, the following analysis will be based on a flat velocity profile, corresponding to a situation were the width of the channel is much larger than the height of the channel. In this case the flow rate, Q, in a channel of height, H, and width, w, is given as $Q = H \cdot w \cdot \upsilon$, where υ is the average flow velocity in the channel. Equation 4.1 for a flat velocity profile will result in a relation between the velocity in the pinch segment, υ_p, and the wide part of the enhancing segment, υ_E, see Eqn. 4.3.

$$\frac{\upsilon_p}{\upsilon_E} = \left(\frac{R_E}{R_s} + 1\right)\frac{d_E}{w_p} \tag{4.3}$$

Here d_E is the width of the wide part of the enhancing segment and w_p is the width of the pinch segment.

If Eqn. 4.2 is solved for a flat velocity profile, it is found that $y'_{EPFF} = \frac{\upsilon_p}{\upsilon_E}\, r$. Combining this equation with Eqn. 4.3, a relation between y'_{EPFF} and r, depending on the geometry of the device, is derived, see Eqn. 4.4.

$$y'_{EPFF} = \left(\frac{R_E}{R_s} + 1\right)\frac{d_E}{w_p} r \tag{4.4}$$

As seen from Eqn. 4.4, y'_{EPFF} is expected to depend on the ratio between the resistance in the enhancement and sink segment, the ratio between the width of the wide part of the enhancement segment and the pinch segment and to be linearly depending on the radius of the particle.

Separation in PFF and in EPFF can be compared by the separation enhancement factor (SEF), which is the ratio between y'_{EPFF} and the corresponding distance in PFF, y'. In the case of a flat velocity profile the SEF is given in Eqn. 4.5.

$$SEF = \frac{y'_{EPFF}}{y'} = \left(\frac{R_E}{R_s} + 1\right)\frac{d_E}{w_b} \tag{4.5}$$

As seen from Eqn. 4.5 we expect the SEF only to depend on geometrical values and to be independent of the particle size.

As discussed in Chap. 2, analytical models based on Poiseuille flow in either 1) flat and wide channels ($w_p >> h$ and $w_b >> h$), corresponding to a two dimensional problem, or 2) channels with a rectangular cross-section ($w_p > h$ and $w_b > h$), are neither one sufficient to describe the flow in PFF. Similarly, they are therefore deemed insufficient for the case of EPFF. Equation 4.4 and 4.5 give a qualitative understanding but not a correct quantitative description. These equations illustrate that to realize a high enhancement of the separation, the hydraulic resistance in the enhancement segment should be large compared to the one in the sink segment. At the same time, the width of the wide part of the enhancement segment should be as large as possible compared to the width of the broadening segment. As illustrated in Chap. 2, a numerical model was proven to be better at least for low solid concentrations. A numerical model, similar to the one described in Sec. 2.2.2, is established for EPFF with dimensions as the fabricated devices described in Sec. 4.2 and no-slip boundary conditions applied at the walls. The inlet flow rates were set to $5\,\mu L/hr$ (sample inlet channel) and $600\,\mu L/hr$ (buffer inlet channel), similar to the values used in the measurements. The result of the

simulation is plotted and compared with a simulation of the flow in PFF in Fig. 4.2. Streamlines corresponding to microspheres with a radius of 0.5 µm, 1.5 µm and 2.5 µm are plotted in the simulations.

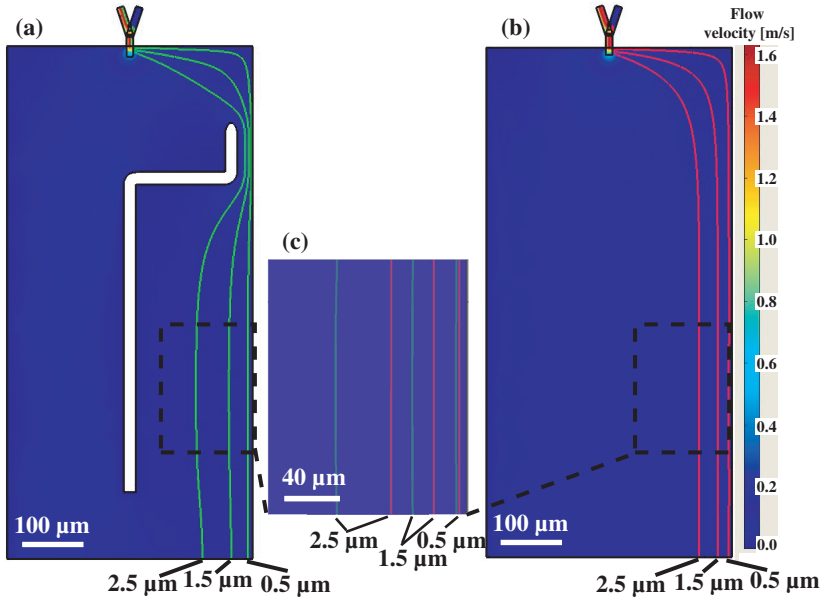

Figure 4.2: Comsol simulations of the flow in (a) an enhanced pinched flow fractionation (EPFF) device and (b) a pinched flow fractionation (PFF) device. Streamlines corresponding to microspheres with a radius of 0.5 µm, 1.5 µm and 2.5 µm are implemented in both pictures. (c) A close-up of the streamlines in both devices stacked on top of each other (green lines are corresponding to EPFF and red to PFF).

It is evident from the simulations that an enhancement of the separation is expected when the snake-like structure is introduced. Furthermore, the size of the enhancement is increasing with the size of the particle, which is different compared to the analytical model in Eqn. 4.5. The numerically calculated y', y'_{EPFF} and SEF are plotted as a function of the particle radius in Fig. 4.4.

4.2 Device layout and fabrication

Devices based on EPFF were fabricated in mr-I T85-20XP using nanoimprint lithography (NIL) as described in Sec. 3.2. The micro channels in both types of devices are 12.5 µm deep, and the width ranges from 11.7 µm (the pinch segment) to 400 µm (the broadening segment). The narrow part of the enhancement segment is 25 µm wide and 90 µm long and the wide part is 190 µm wide and 510 µm long. The EPFF device is constructed so that microspheres with a radius up to 4.5 µm will enter the enhancing segment.

4.3 Separation measurements

Separation in the EPFF devices were evaluated by benchmarking against the basic PFF devices, described in Chap. 2 with the exact same device geometries, differing in the snake-like structure that is only present in the EPFF devices. Separation measurements were conducted in the PFF and EPFF with seven different sizes of fluorescently labeled polystyrene microspheres ranging in radius from 0.26 µm to 2.5 µm. The microspheres were suspended in a buffer solution (Milli-Q water with 0.1 % w/w SDS) and an identical buffer was used as the pinching liquid. The flow rates in the two inlet channels were set to 5 µL/hr and 600 µL/hr in the sample and buffer inlet respectively. All measurements were carried out with a microsphere concentration of 0.05 weight per volume-% (% w/v). Separation of 0.5 µm and 1.5 µm microspheres in the PFF and EPFF devices are shown in Fig. 4.3.

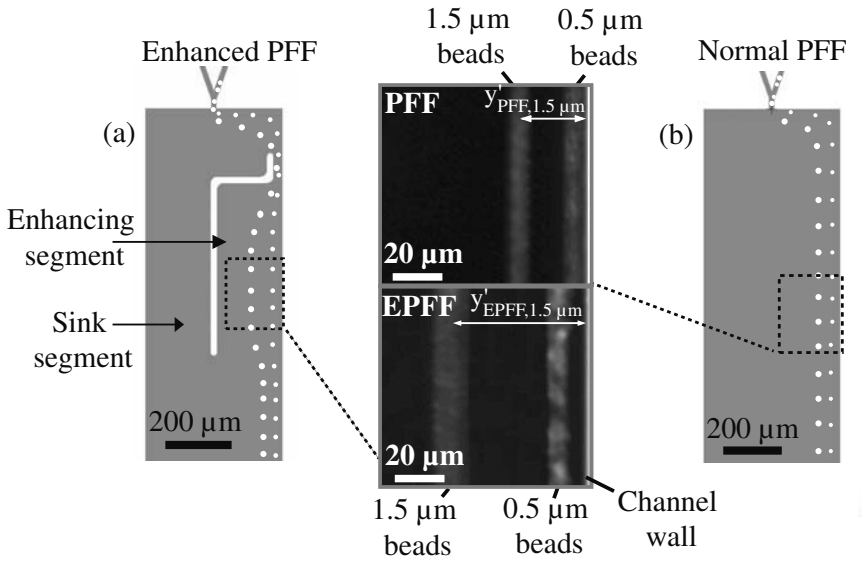

Figure 4.3: Separation of polystyrene microspheres (beads) with a radius of 0.5 µm and 1.5 µm in a pinched flow fractionation (PFF) device and an enhanced pinched flow fractionation (EPFF) device. Each microsphere size is displaced further from the wall and the separation is amplified in EPFF with regards to the PFF device.

As shown in Fig. 4.3 the separation of 0.5 µm and 1.5 µm spheres is enhanced in the EPFF (Fig. 4.3(a)) compared to the PFF device (Fig. 4.3(b)). The measured position of the microspheres in the broadening segment, y' and y'_{EPFF}, of the seven sphere sizes, is plotted together with the analytical and numerical calculations in Fig 4.4(a). The separation enhancement factor (SEF) of each microsphere size is plotted in Fig. 4.4(b) together with the analytical and numerical calculation.

As seen in Fig. 4.4(a) the separation is clearly enhanced in the EPFF. In addition, the numerical calculation fits much better with the measurements compared to the analytical predictions from Eqn. 2.7 and 4.4. The analytical calculations overestimate

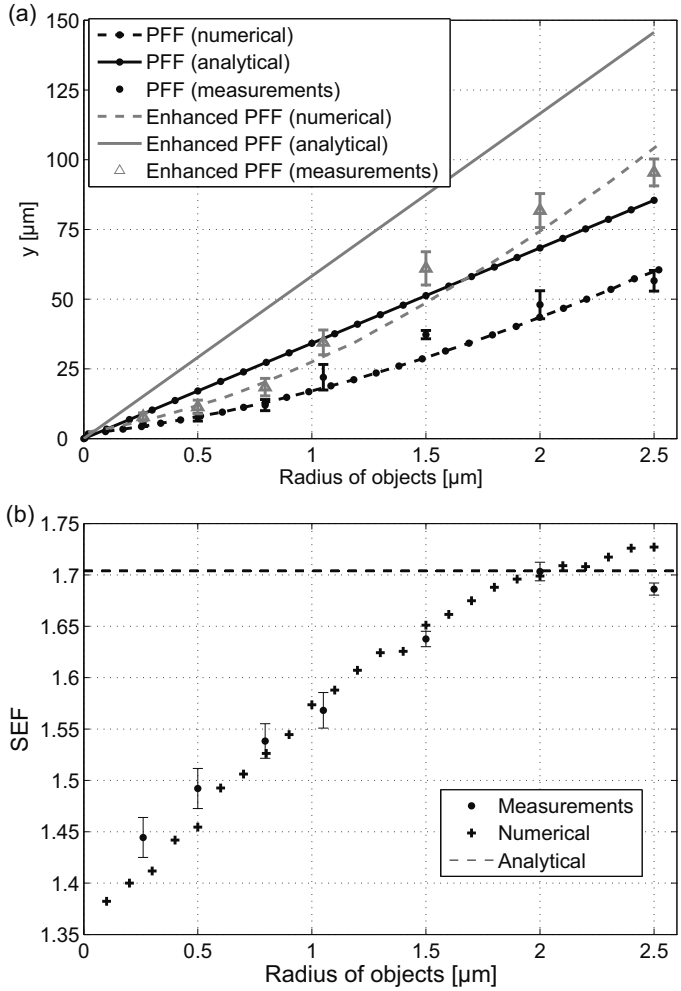

Figure 4.4: (a) Distance between the bead position in the broadening segment and the channel wall y_{PFF} and y_{EPFF} in the PFF and EPFF device respectively as a function of the particle radius. Each measurement data point represents >300 beads, and the error bars represents the standard deviation of the measurements. (b) The separation enhancement factor (SEF) as a function of the particle radius.

the measured values of y'_{PFF} and y'_{EPFF} up to 60 % as discussed in Chap. 2. The numerical calculation fits very well with the results from the smallest microspheres, but begin to deviate more as the sphere size increases, up to a maximum deviation of 23 %. The deviation is seen to be similar in PFF and EPFF. This discrepancy is probably, as discussed in Chap. 2, originating from the lift force. However, the presented numerical calculation represents a qualitatively good description of the results, both for PFF (as demonstrated in Chap. 2) and EPFF. The measured SEFs, plotted in Fig. 4.4(b), fits well with the numerical values, whereas the constant analytical value predicts an upper limit of the SEF. The measurements revealed an enhancement in separation that is increasing with the radius of the particles, saturating at approximately 70 %.

Radius [μm]	$\mathbf{y'_{EPFF}}$ [μm]	$\sigma_{\mathbf{y'_{EPFF}}}$ [μm]	$\delta\mathbf{r_{d,exp}}$ [μm]	$\delta\mathbf{r_{d,h}}$ [nm]
0.26	8.2	1.4	0.08	44
0.5	11.3	2.5	0.20	30
0.75	18.5	3.1	0.24	26
1.05	34.5	4.5	0.26	18
1.5	61.1	5.9	0.28	14
2.0	81.8	6.1	0.30	10
2.5	95.4	4.8	0.24	8

Table 4.1: Separation measurements from the enhanced pinch flow fractionation device and the calculated maximum resolution, $\delta r_{d,h}$, and the measured value, $\delta r_{d,exp}$. $\delta r_{d,h}$ does not include a size distribution of the individual microsphere sizes whereas in $\delta r_{d,exp}$ the standard deviation microsphere size (5 %) is included.

The maximum resolution, $\delta r_{d,h}$, excluding size distribution of the sample, in EPFF in regards to detection of the separated sample particles, is calculated as described in the Chap. 2 and listed in Table 4.1 for the used microsphere sizes. The resolution is limited by diffusion and is therefore dependent on size. The measured standard deviation in y'_{EPFF}, $\sigma_{y'_{EPFF}}$, is listed in Table 4.1 and used to calculate the experimental resolution, $\delta r_{d,exp}$, as described in Chap. 2.

Besides an enhancement of the separation comparing the PFF and EPFF device layout, it is also seen from Table 4.1 and Table 2.3 that the resolution is enhanced. However, the measured resolution range from 80 nm to 300 nm in EPFF and from 100 nm to 420 nm in PFF depending on radius is enhanced up to approximately 25 % for the largest sizes.

4.4 Summary and outlook

To summarize, the separation in PFF can be enhanced by a simple geometric modification of the device layout. This enlargement does not rely on any external forces, which usually add complexity to the fabrication process. Nor does it involve any enlargement of the channel device area. The area is actually slightly reduced. The fabricated enhanced PFF devices are therefore suited for cheap and high volume production by roll-to-roll thermal imprint. Compared to other attempts to amplify the separation in PFF [85, 86] (described in Chap. 1), the layout of EPFF is more simple and does not enlarge the channel area or add any complex control units. The maximum resolution of EPFF for perfect monodisperse samples was calculated to be 8 nm, and is thereby higher than in the normal PFF layout. In the case of the measurements with size distributed microspheres (standard deviation in the size of 5 %), the resolution was increased up to approximately 25 % for the larger particles.

The semi-3D numerical model introduced in Sec. 2.2.2 was seen to give a fine description of the enhanced separation in PFF. The separation enhancement factor was found to be dependent on particle size and range up to 70 %, in good accordance with the numerical model.

The EPFF devices fabricated throughout the study were optimized for separation of the microspheres with radii up to 4.5 µm and not up to 2.5 µm, which was the sphere radii used in this work. If the device was optimized for these radii, a separation enhancement factor up to 2.6, corresponding to a 260 % enhancement and a maximum separation resolution of 4 nm, is expected.

Chapter 5

Optofluidic microscope for detection in pinched flow fractionation

As demonstrated in a prior chapter polymer-based devices based on pinched flow fractionation (PFF) with a reproducible outcome, can be fabricated at a low cost and at a high volume using roll-to-roll methods. However, bulky and expensive optical microscopes are still necessary for data readout from such microfluidic systems, especially in analysis of biological and chemical samples. One alternative is the optofluidic microscope (OFM) [116] which is a cheap, compact and more automated choice in regards to retrieving data. Furthermore, the OFM can be integrated in microfluidic platforms and is therefore also portable.

In the present chapter, integration of an OFM in a PFF device is presented. This setup is demonstrated for 3 dimensional optical detection as well as on-chip particle image velocimetry (PIV), using a conventional microscope as relay. Finally, all results are summarized including a short outlook.

5.1 Principle of OFM detection in PFF

The OFM consist of an opaque film patterned with apertures arranged in a line which is tilted relative to the flow direction of an above lying microfluidic channel. Time resolved transmission of light through the apertures as well as knowledge of the laminar flow velocity is used to reconstruct the image of a passing object, at a resolution defined by the dimensions of the aperture array. The OFM is integrated into a PFF device, positioned under the broadening segment, as illustrated in Fig. 5.1(a). When the separated particles pass the broadening segment they affect the transmission of light through the apertures constituting the OFM. The transmitted light from each aperture spreads radially and is collected in a cone with a characteristic angle, due to the numerical aperture (NA) of a collector objective, as illustrated in Fig. 5.1(b). Each particle thus affects the light from apertures over a distance in regards to the width of the channel, y-direction, which is larger than their diameter and depends on their height in the channel, z-direction, see Fig. 5.1(b). This enables detection of two

dimensional separation: Size separation in the y-direction which occurs in PFF and separation in the z-direction in response of an external force. An additional separation parameter can thereby be added to PFF without adding any complexity in the detection. Furthermore, PIV is enabled by detecting the x position and knowing the readout sampling rate.

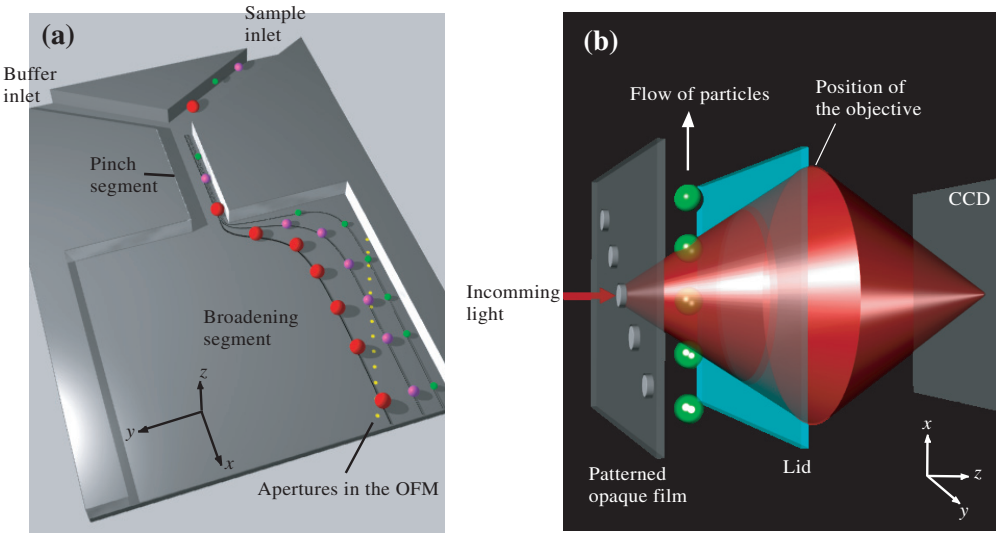

Figure 5.1: (a) Principle of pinched flow fractionation (PFF) with an integrated optofluidic microscope (OFM) located in the broadening segment. (b) Illustration of how transmitted light trough an aperture is affected when particles pass in the channel. The light is collected by an objective, after passing the channel, and redirected to a CCD. The angle of the collected light is defined by the numerical aperture of the objective.

5.2 Layout and fabrication of devices

The microfluidic PFF separation devices are defined by planar nanoimprint lithography in a film of cyclo-olefin copolymer (COC), placed on top of an aluminum (Al) film with periodically arranged circular apertures constituting the OFM. All channels in the PFF device are 12.5 µm deep and range from 11.7 µm (pinch segment) to 400 µm (broadening segment) in width (further described in Chap. 2). The apertures in the Al film are designed to be 650 nm in diameter and are placed underneath the broadening segment. The apertures are placed in a line, which is tilted relative to the flow direction, x, in the broadening segment. The center-to-center distance between the apertures are 14 µm in the x-direction and 650 nm in the perpendicular y-direction, as illustrated in the inset of Fig. 5.2(a). Two lines, each of 307 apertures, are subsequently positioned in the broadening segment along its length, covering the full length and half of the width. The first line of apertures is sufficient to determine the x, y and z position of separated particles, and diffusion can be measured comparing with detection at the second line. An illustration of the design is shown in Fig. 5.2(a) and the fabrication process is described below.

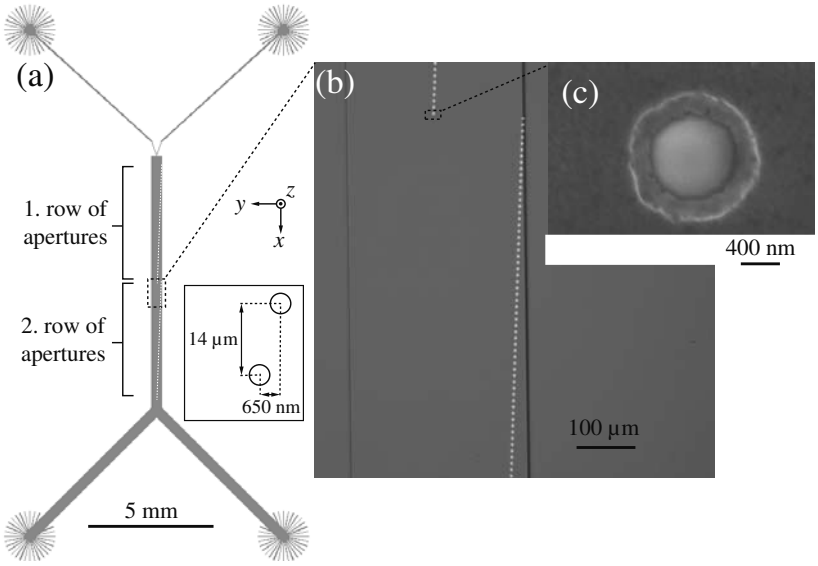

Figure 5.2: (a) The device layout. The distance between the apertures in the x- and y-direction is illustrated in the inset. (b) A microscope image of a finished device with backside illumination. The OFM apertures appear as white dots. (c) Scanning electron microscope image of an aperture. The footprint of the isotropic aluminium etch is clearly visible.

A 4 inch borofloat glass wafer (JinSol, Seul, Korea, www.all4semi.com) is used as the substrate. The glass wafer is cleaned in a mixture of 75% sulfuric acid (H_2SO_4) and 25% hydrogen peroxide (H_2O_2), rinsed in water and left in an oven at 250 °C over night — all to promote adhesion of Al. 150 nm Al is electron beam deposited (QCL 800,Wordentec, Devon, England, http://www.wordentec.com) on the clean borofloat glass wafer, and a 450 nm thick layer of a positive electron beam sensitive resist (ZEP520A, Marubeni Europe Plc, London, England, http://www.europe.marubeni.com) is spin coated on the Al. Apertures are defined in the resist by an electron beam writer (JEOL-JBX9300FS, dose: 250 µC/cm^2, current: 1.38 nA, step size: 4 nm) and the exposed resist is developed in ZEP-N50 (Marubeni Europe Plc, London, England, http://www.europe.marubeni.com). The Al underneath the openings is etched at an ultra-sound treatment in a mixture of 25 % MF322 (Candor Kemiske A/S, Vejle, Denmark, http://www.candordenmark.dk) and 75 % water. A SEM image of an aperture in the Al film is shown in Fig. 5.2(c). As seen from Fig. 5.2(c) the Al etch is isotropic, so under-etching of the mask results in enlargement of the aperture diameter compared to the designed diameter of 650 nm. The aperture diameter of all fabricated devices was measured to range from 650 nm to 850 nm, with an average diameter of 750 nm. At this point the OFM is finished and the PFF device is defined by thermal NIL in mr-I T85 20XP on top of the OFM as described in Chap. 3. The residual layer at the apertures is 8±0.1 µm. A microscope image of the fabricated device with backside illumination is shown in Fig. 5.2(b).

5.3 Measurement setup and data readout

The experimental setup is illustrated in Fig 5.3. The device is mounted on a holder which fits into an inverted fluorescence microscope (Eclipse2000, Nikon) and contains fluid connections to the device. A white Halogen light source (Nikon, Surrey, United Kingdom, http://www.nikoninstruments.com) is used to illuminate the apertures. The transmitted light from the apertures is collected with an 10x objective ($NA = 0.3$ in air, Nikon, Surrey, United Kingdom, http://www.nikoninstruments.com) and detected by an EMCCD camera (Cascade 512II, Photonics, Tucson, United States, http://www.photomet.com), although the electron-multiplication capability of the camera is not used throughout the measurements.

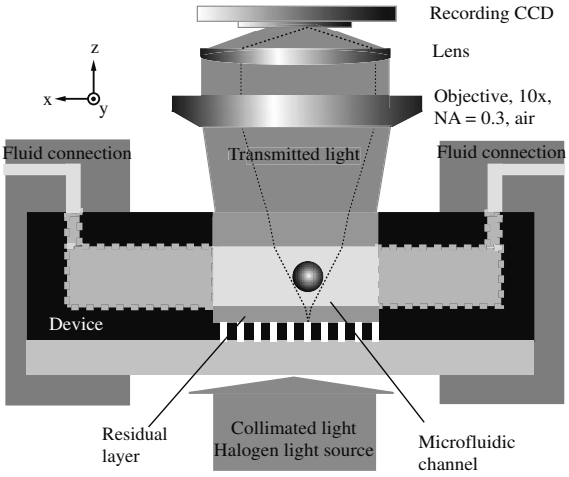

Figure 5.3: Cross-sectional illustration of the measuring setup. A device is mounted in a chuck with fluid connections. The backside of the device is illuminated by collimated light, and the part that is transmitted through the apertures in the device is collected by a 10x air objective (NA = 0.3), focused by a lens onto a CCD detector.

Each aperture appears as a white spot consisting of several pixels on the CCD image. When a movie of the transmission is recorded, all apertures are identified in the first image. Here, both the position and number of pixels of each aperture is defined. For all subsequent images, the intensity from each aperture is summed over the relevant pixels. As a result the transmission versus time for all apertures is recorded. An example of such readout, from one aperture, over 9.4 s is shown in Fig. 5.4(a). Here five microspheres pass the aperture. A reference fluorescence microscope image, also of 1.05 µm pinched polystyrene (PS) microspheres passing the OFM at a similar time interval, is shown in Fig. 5.4(c). Only the transmitted light from each aperture within a solid angle, α, defined by the NA of the objective, is collected, see Fig. 5.1(b). Therefore, the dip in transmission caused by a passing microsphere depends on the overlap with the cone of light. For a specific z position, a maximum dip occurs at the aperture which is best aligned with the center of the sphere. In addition, the microspheres influence the transmission from a number of apertures that cover a distance which is larger than the microsphere diameter. This effect is seen in Fig. 5.4(b), which shows the transmission through 9 holes, corresponding to 5.9 µm, as a 1.05 µm microsphere

passes.

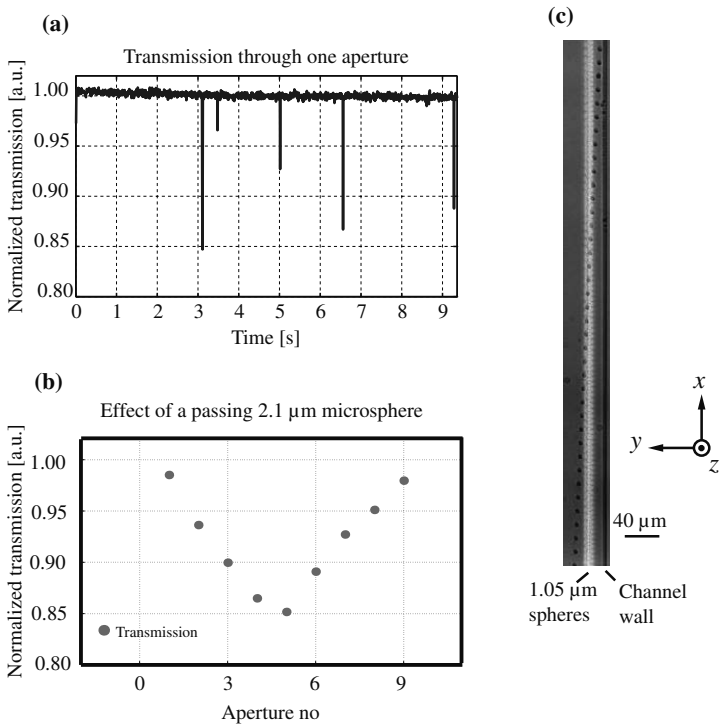

Figure 5.4: Transmission readout from the OFM. (a) Readout from one aperture as a function of time and when 1.05 µm polystyrene spheres passes. (b) Readout from a 1.05 µm microsphere effecting the transmission from several apertures. (c) Reference fluorescence microscope images of pinched 1.05 µm microspheres passing above the apertures. The exposure time of the microscope is long, so the microspheres appears as lines and several microspheres have passed in the image.

With data as those shown in Fig. 5.4(a) and 5.4(b), the $x(t)$, y and z position of a passing microsphere as well as its velocity can be determined as described in the following sections. Here, the expected position- and velocity distribution of passing spheres will also be introduced and used to validate the confocal usage of the OFM.

5.3.1 Detection of separated particles

The position $\langle y \rangle$ for the center of mass of each microsphere in the broadening segment is determined from the "transmission versus aperture number" data. One example of such data set is shown in Fig. 5.4(b). The weighted average of the transmission data is used to find $\langle y \rangle$:

$$\langle y \rangle = \frac{\sum_i y_i(1 - T_i)}{\sum_i (1 - T_i)} \tag{5.1}$$

Here y_i is the position of the ith aperture and T_i is the corresponding transmission (see Fig. 5.4(b)).

In accordance with Eqn. 5.1, the accuracy in $\langle y \rangle$ is increasing with increasing number of data points (apertures, i, for which $T_i < 1$) and thereby, as previously mentioned, it depends on the z position of the sphere and the aperture pitch in the y-direction. The lower limit of the accuracy in $\langle y \rangle$ is given by the aperture pitch, 0.65 µm. As a comparison, the resolution in fluorescence microscopy, using green excitation light ($\lambda \approx 535\,\text{nm}$) and the same objective as used in the OFM detection ($NA = 0.3$), is 0.9 µm in accordance with the Abbe equation.

In the PFF separation experiment, see Fig. 5.1(a), the microsphere radius r determines the distance, y', between the center of the microsphere and the channel wall in the broadening segment, as described in Chap. 2. Knowing the distance to the channel wall from each aperture, $\langle y \rangle$ is used to determine y'. The uncertainty of y' is thereby a combination of two contributions: 1) the above described accuracy in $\langle y \rangle$ ($\leq$0.65 µm). 2) The uncertainty in position of the apertures in the y-direction caused by the electron beam writer (20 nm) and misalignment between the apertures and the imprinted microchannel (0.65 µm). Because of fabrication accuracy the microchannel and the apertures are often misalignment in the y-direction. The first aperture in the microfluidic channel that is not affected by the channel wall is therefore defined as $y = 0$, and is determined with an uncertainty equal to the aperture pitch (0.65 µm). By propagation of errors, the uncertainty of y' is $\leq$0.92 µm.

The expected value of y' as a function of r is calculated numerically, as described in Chap. 2 for spherical objects with a radius of 0.5 µm, 1.05 µm, 1.5 µm and 2 µm. These results are used in Sec. 5.4.1 to convert measured y' values to radii. The size distribution of the microspheres is Gaussian, centered around the nominal radius with a standard deviation of 5% [134]. Therefore, the distance y' of a Gaussian size-distributed particle sample will also be Gaussian, as discussed in Chap. 2. The size distribution results in a standard deviation on y' which is equal to 0.6 µm, 1.4 µm, 2.0 µm and 3.2 µm for the four bead sizes. In addition, diffusion is expected to broaden the original Gaussian distribution. In this work the diffusion length can be calculated using the Stoke-Einstein equation, to vary from 0.8 µm to 3.4 µm depending on the microsphere size and the flow rate in the system. The implications of diffusion are measured in Sec. 5.4.1.

5.3.2 Detecting the z position of particles in the channel

According to Fraunhofer diffraction, a planar wavefront with wavelength λ will, after passing an aperture of diameter a, spread radially from the aperture if a is on the same order as λ. This effect, combined with the numerical aperture, NA, of the optical system collecting the light, is utilized to determine the z position in the channel of a passing microsphere. In the following, ray-optics is used as a first approximation to calculate the light propagation from the aperture, through the microfluidic channel and finally into the objective, as shown in Fig. 5.5.

Here, it is assumed that the NA of the microscope objective sets the maximum angle of the light collected from the apertures. The maximum angle, α, and the NA is correlated by:

$$\alpha = \arcsin\left(\frac{NA}{n}\right) \tag{5.2}$$

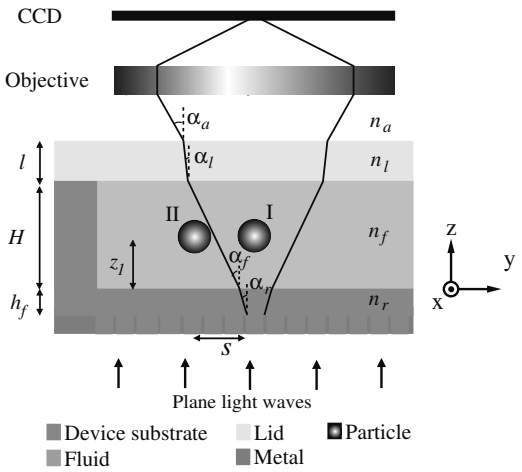

Figure 5.5: Cross-sectional view of the propagation of transmitted light from one aperture in the microfluidic device. Two spheres are passing in two different horizontal positions. I: The sphere is located exactly above the aperture, so the transmission dip is at its maximum. II: The sphere is tangent to the cone of light collected from the aperture by the objective, and the transmission from this aperture is unaffected. This sphere effects the transmission from the five apertures to the left. Besides geometries, the refractive indices of air, n_a, the lid, n_l, the fluid, n_f, and the device material, n_r, is shown in the figure.

Where n is the refractive index of the medium in which the light is propagating.

Refraction of light traveling through an interface is described by Snell's law:

$$n_1 sin(\beta_1) = n_2 sin(\beta_2) \tag{5.3}$$

where n_1 and n_2 are the refractive indices of the medium on each side of an interface and β_1 and β_2 is the angle of the incoming and the outgoing light with respect to the normal of the interface.

Combining Eqn. 5.2 and 5.3, the z position of a passing sphere is derived from the NA of the objective, the geometry of the device, the material properties and the distance, $2s$, over which the sphere will affect the transmitted light from the apertures. Here the distance from the bottom wall to the center of the microsphere is denoted z_1. z_1 is given in Eqn. 5.4.

$$z_1 = \frac{s - rcos\left[\arcsin\left(\frac{NA}{n_f}\right)\right] - h_f \tan\left[\arcsin\left(\frac{NA}{n_r}\right)\right]}{\tan\left[\arcsin\left(\frac{NA}{n_f}\right)\right]} - r\frac{NA}{n_f} \tag{5.4}$$

Here n_f is the refractive index of the fluid in the channel, h_f is the thickness of the imprinted material on top of the Al film and n_r is the refractive index of the imprinted material.

By collecting data from several separated microspheres passing inside the broadening segment, a histogram of their z_1 positions can be made. This histogram is

expected to reflect the distribution of microsphere velocities in the flow direction. In all measurements the flow is pressure driven and the velocity distribution of the fluid is therefore parabolic with maximum velocity in the center of the channel. Provided that the microspheres are distributed evenly in the z-direction and follow the flow of the fluid, their expected z_1 distribution will also be parabolic. However, as discussed in Chap. 2, spheres moving in a shear flow as the Poiseuille flow experience a force perpendicular to the flow direction and will migrate in one of two ways: 1) towards the center of the channel – systems with high solid concentrations and a low Reynolds number ($\ll$ 1) [132] or 2) towards an equilibrium position in between the center and the wall – systems with low solid concentrations and a high Reynolds number ($>$ 1) [133]. In this work the solid concentration is low and the Reynolds number is much smaller than one in the broadening segment. Neither of two descriptions fully describe the presented measurements, but it is expected that the results will reflect one of them.

The detection accuracy in the z-direction, δz, is seen from Eqn. 5.4, to depend on how well s can be determined, the standard deviation of the microsphere radius and the uncertainty of the residual layer thickness. In this study s is found by multiplying the aperture pitch with the number of affected holes of each microsphere divided by two. The accuracy of s, δs, is therefore determined by half the aperture pitch, which is 0.65 µm. The standard deviation of the microsphere radius is 5 % of its size and the uncertainty of the residual layer is 0.1 µm. By propagation of uncertainties, the detection accuracy in the z-direction is found to be limited by $\delta s / \tan[\arcsin(NA/n_f)]$ ($NA = 0.3$ and $n_f = 1.33$), and equals 1.4 µm.

The flow velocity in the system was found to be crucial for the success of a measurement. At high velocities only apertures aligned with the central parts of the microspheres yield a transmission dip that is above the detection limit. In this case the information of the z position is lost. It is therefore important to operate the system at low velocities. The maximum velocity, at which z detection is still possible, is correlated with the minimum exposure time of the used CCD, which in this work is 7.8 ms. The maximum particle velocity was found to be 2 mm/s, corresponding to a total flow rate of 22 µL/h.

5.3.3 Detection of the velocity

The velocity of separated microspheres passing in the broadening segment is determined by recording the number of frames it takes each microsphere to pass the apertures. The velocity is calculated as the slope of a linear function fitted to the 'number of affected apertures' versus 'number of frames' of each microsphere, multiplied by the ratio between the aperture pitch in the x-direction and divided by the exposure time of the CCD. The accuracy of the velocity is limited by the uncertainty of the linear fit ($<$ 4 % of the measured velocity), the uncertainty of the aperture pitch in the x-direction (20 nm defined by the e-beam) and the uncertainty in frame rate of the CCD (0.1 µs at 10 MHz readout). By propagation of uncertainties the accuracy of the velocity can be calculated to be up to 4 % of the measured velocity, defined by the uncertainty of the linear fit. The velocity should not exceed 2 mm/s, as discussed above, giving a lower accuracy limit in the velocity of 0.08 mm/s.

5.3.4 Sample preparation and flow control

In all OFM detection measurements fluorescent labeled polystyrene (PS) microspheres with four different average radii: 0.5 µm, 1.05 µm, 1.5 µm and 2 µm are used. These have absorbance maxima at 542 nm and emission maxima at 612 nm. The microspheres are suspended in a carrier buffer consisting of 0.001 % w/v Triton X100 in MilliQ water. The microsphere concentration is 0.01 % w/v. The microsphere solution is introduced into the device from the sample inlet and carrier buffer without microspheres from the buffer inlet, see Fig. 5.1(a). As discussed earlier the maximum total flow rate is 22 µL/h. Such small flow rates combined with pinched conditions and a steady supply of sample buffer is achieved with a combined flow rate and pressure controlled setup. The flow in the buffer inlet channels is controlled by syringe pumps (11Plus from Harvard Apparatus) and is varied between 5 µL/h and 30 µL/h. The flow in the sample inlet channel is controlled by an air pump (VP 86 with EU-plug, VWR) and is varied from 5 mbar to 30 mbar corresponding to a flow rate between 0.2 µL/h and 1.2 µL/h.

5.4 Detection results

Each time a microsphere passes the OFM in the broadening segment, the $x(t)$, y and z position as well as its velocity is detected. Throughout calibration measurements it was found that the dip in transmission, shown in Fig. 5.4(a), caused by passing microspheres, was doubled when the wavelength of the transmitted light was inside the absorbance range of the microsphere. This observation is important, not only to maximize the signal to noise ratio — which results in better measurements — but also because the absorbance properties of sample particles can be detected and distinguished. At all measurements presented in this chapter a green filter is introduced between the white halogen light source and the device, see Fig. 5.3. Thereby, the device is illuminated at wavelengths of 535±25 nm.

5.4.1 Separation measurements

Initially, the size separation in PFF, detected with OFM, was compared to detection using fluorescence microscopy. A sample containing fluorescent PS microspheres with average radii of 0.5 µm, 1.05 µm, 1.5 µm and 2 µm was introduced into the device as already described, at a total flow rate of 16 µL/h. The transmission signal was recorded during 47 seconds, resulting in the y' position histogram shown in Fig. 5.6. The y' position of the microspheres is seen in Fig. 5.6 to be well described by Gaussian distributions as expected. The average position and width of the fitted Gaussian functions are therefore good measures of the average position and spreading of each microsphere size in the broadening segment. The numerical model from Chap. 2 is used to convert the average positions and spreadings to microsphere radii, r, and standard deviations in size, respectively. These values along with the corresponding values measured by fluorescence microscopy are listed in Table 5.1.

As seen in Table 5.1, the microsphere radii measured by fluorescence microscopy and OFM are in good correspondence. The minor deviations are within the uncertainty given by the measuring method of the y' position (described earlier). The measured

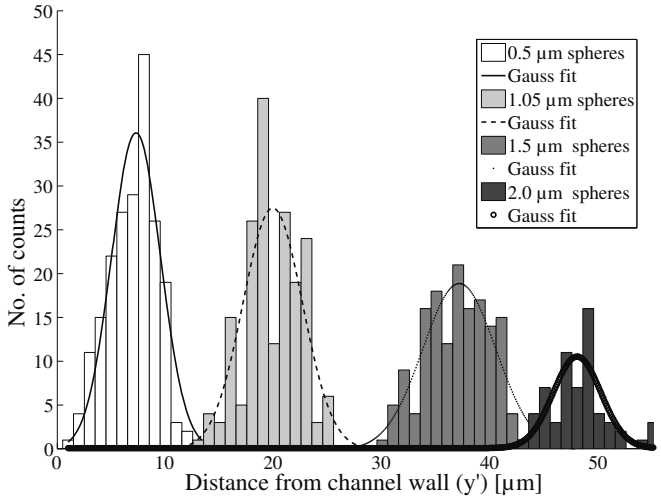

Figure 5.6: Histogram of the position in the broadening segment of separated fluorescent labeled polystyrene microspheres with average radii of 0.5 µm, 1.05 µm, 1.5 µm and 2 µm detected by the optofluidic microscope. A Gaussian function is fitted to each of the peaks in the histogram to find the position of their maximum together with the standard deviation.

radii and standard deviations are also seen to be larger than those given by the manufacturer of the microspheres. The numerical Comsol model overestimates, as described in Chap. 2, the radius for a given value of y'. This is the cause of the deviation in radius. In addition, diffusion is not included in the model. The large deviation in the defined and measured standard deviations is a result of diffusion, which is seen to limit the performance of the system. The total flow rate in the system should therefore be as large as possible, but can not be larger than 22 µL/h without compromising the detection. At this flow rate, diffusion is a significant limiting factor to the resolution of the separation, and exceeds the contribution from uncertainty in size. Compared with the basic PFF measurements (Chap. 2), which was operated at a total flow rate of 605 µL/h, the resolution is lower. In future work, the signal to noise ratio of the transmission data present in the OFM measurements should be optimized for larger

	$\langle r \rangle$	$\sigma(r)$	$\langle r \rangle$	$\sigma(r)$	$\langle r \rangle$	$\sigma(r)$	$\langle r \rangle$	$\sigma(r)$
Microsphere specs [µm]	0.5	0.025	1.05	0.053	1.5	0.075	2.0	0.10
PFF with fluor. [µm]	0.5	0.13	1.2	0.23	1.8	0.26	2.2	0.18
PFF with OFM [µm]	0.5	0.13	1.1	0.26	1.8	0.27	2.2	0.18

Table 5.1: Measured radius, r, and standard deviation in radius, $\sigma(r)$, of the separated microspheres (0.5 µm, 1.05 µm, 1.5 µm and 2 µm delivered with a standard deviation in size of 5%). The numerically model (see text) is used to convert the distance from the channel wall in the broadening segment and the spreading, detected by OFM and fluorescence microscopy to radii and the corresponding standard deviations. The model does not include diffusion, which is the reason for the large deviation between the measured standard deviations and those given by the manufacturer of the microspheres.

flow rates.

In Fig 5.6 it is observed that the number of detected microspheres decreases with increasing radius. This is expected, as for a constant solid content (0.01 % w/v) the number of spheres per volume decreases with increasing radius.

5.4.2 Height position, z_1, and velocity measurement

In all presented z_1 position and velocity measurements, the microspheres were introduced one size at the time. The solid concentration of the microsphere sample is 0.01 % w/v. The microspheres will at this concentration and relevant velocities pass one at the time in the pinch segment. The average distance between the spheres is $\geq 20\,\mu$m, depending on radius. It is therefore reasonable to assume that particle perturbation of the flow in the broadening segment has no significant effect on subsequently passing particles. For each passing microsphere the total number of apertures at which the transmission was affected was recorded. The number of affected apertures was converted by Eqn. 5.4 ($NA = 0.3$, $n_f = 1.33$, $n_r = 1.53$ and $h_f = 8\,\mu$m) to a position in the z-direction. The result of two measurements, with 0.5 µm spheres and 1.05 µm spheres, is shown in Fig. 5.7(a) and 5.7(b) as histograms of the z_1 position. In addition, the time each microsphere affected the transmission through the apertures and the corresponding x position was recorded and converted into a velocity. The measured velocities of the same measurements are shown in Fig. 5.8(a) and 5.8(b).

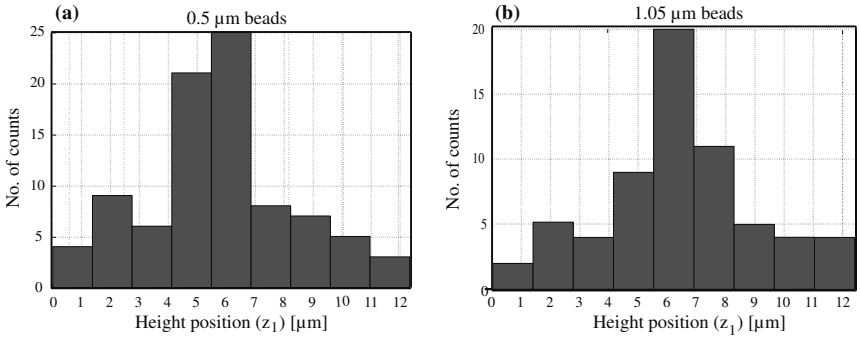

Figure 5.7: Histogram of the height position of 0.5 µm and 1.05 µm pinched fluorescent labeled PS microspheres. The channel height is 12.5 µm.

The total flow rate in the measurement with 0.5 µm microspheres is 9 µL/h corresponding to an expected minimum velocity v_{min} equal to 0.12 mm/s and a maximum velocity v_{max} equal to 0.75 mm/s. At the measurements with 1.05 µm microspheres the total flow rate was 11 µL/h corresponding to $v_{min} = 0.24$ mm/s and $v_{max} = 0.93$ mm/s. The minimum velocity is calculated at a distance from the channel floor or top, corresponding to the radius of the microspheres. However, it should be noted that these calculated values are the velocity of the fluid. The values are indicated as vertical solid lines in the graphs of Fig. 5.8 and is seen to agree well with the measured microsphere velocities. In Fig. 5.8, a plot of the velocities calculated from the z_1-position data in Fig. 5.7, under the assumption that they follow a parabolic velocity profile with the above derived maximum velocities, is added. As seen in Fig. 5.8, the measured z_1

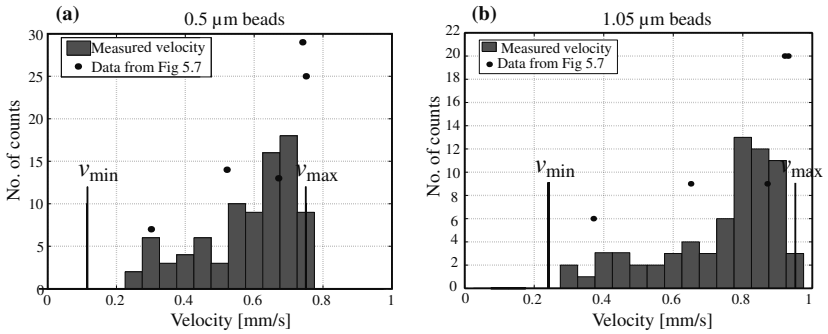

Figure 5.8: Histogram of the velocity of 0.5 µm and 1.05 µm pinched fluorescent labeled PS microspheres. The vertical lines indicate the expected minimum, v_{min}, and maximum, v_{max}, velocity of the carrier fluid.

positions are in good correspondence with the measured velocities. Furthermore, it is seen from the graphs in Fig 5.7 and 5.8 that the spheres are not following the parabolic flow profile of the fluid, but are forced towards the center of the channels as expected for high concentration suspensions at low Reynolds numbers as described by [132].

5.5 Summary and outlook

In this chapter an optofluidic microscope (OFM) is integrated into a pinched flow fractionation (PFF) device. The device has been demonstrated for: 1) in-plane detection of size separated microspheres ranging from 0.5 µm to 2 µm in radius with an accuracy of $\leq$0.92 µm, 2) out-of-plane detection with an accuracy of 1.4 µm and 3) particle image velocimetry (PIV) with an accuracy of 4 % of the measured velocity. The maximum velocity should not exceed 2 mm/s in the OFM measurements, corresponding to an accuracy of 0.08 mm/s. In all measurements the results were in good correspondence with results obtained by fluorescence microscopy. An important point to note is that tumbling of sample particles does not negatively impact the effectiveness of OFM detection in the presented application, contrary to earlier demonstrated applications.

In this chapter, the OFM combined PFF device was demonstrated in combination with a conventional microscope, which was used as a relay. In future work an obvious further development would be to fabricate the device directly on a lens array and a CCD detector, realizing a compact and portable system.

In the combined OFM and PFF devices only detection of separation in the two dimensions perpendicular to the flow direction are of interest. However, detection along the flow direction could be used successfully in field flow fractionation (FFF) based separations. Detection of different absorption properties using the OFM was demonstrated, but not further investigated. However, this would be interesting in regard to effective on-chip microsphere suspension arrays.

Chapter 6

Detection of single nucleotide polymorphisms - an application of pinched flow fractionation

Single nucleotide polymorphisms (SNPs) comprise the most common type of genetic variation in the human genome. SNP genotyping is employed for various purposes including forensic genetics, diagnosis of monogenic diseases and association studies for detecting genetic factors important in polygenic diseases [157]. To meet the growing demand for SNP analysis, technologies that are accurate, robust, flexible and offer high-throughput in regards to number of SNPs are required. Point mutation analysis in microfluidic lab-on-a-chip (LOC) systems can provide fast and automated analysis. The analysis of point mutations has previously been demonstrated using two approaches: 1) by immobilizing DNA probes in fixed spots in microfluidic channels [158, 159, 160], or 2) immobilizing DNA probes on suspended microspheres [161, 162]. When micro-systems are functionalized during fabrication as in the first approach, further downstream processing becomes limited, as DNA is sensitive to heat and chemicals. Furthermore, immobilization of probes within the microstructures reduces the flexibility and potential reuse of the systems [163].

In this chapter a method is described to separate signals from perfect match hybrids and mismatch hybrids by immobilization of probes on differently sized microspheres, and separating the microspheres by pinched flow fractionation (PFF). Genotyping by PFF is characterized by SNP detection with synthetic oligonucleotide targets and SNP detection of human DNA samples from individuals with a point mutation (CD8/9+G) in the Hemoglobin beta (HBB) gene. HBB is a protein that makes up the most common form of hemoglobin in adult humans. The SNP studied in this chapter is responsible for a blood disease, in which the individual has problems with uptake of oxygen in the blood. Preparation of samples, hybridization and stringent wash is described, before the SNP-detection capability of PFF is demonstrated. Finally, the method is compared with other SNP analysis platforms and the results are summarized. Some of the work presented in this chapter is published in [128].

6.1 Principle of SNP detection in PFF

In the PFF-based SNP detection method demonstrated in this chapter, preparation and immobilization of sample on microspheres are performed off-chip. It is a general wish in the LOC community to have these functionalities integrated in the system. Recent work within these topics is promising [164, 165, 166]. However, the task is not trivial. It is therefore possible that future LOC solutions only include the actual SNP detection and all prior steps are done outside the chip. Steps involved in microsphere-based SNP detection in PFF devices are illustrated in Fig. 6.1. A sample including cells, e.g. a blood sample, is withdrawn from the patient, Fig. 6.1(a). The cells are lysed and genomic DNA is extracted from the sample, Fig. 6.1(b). The relevant region of the genomic DNA is amplified in a polymerase chain reaction (PCR) and afterwards labeled with a fluorescent marker, Fig. 6.1(c). Parallel to this process, streptavidin coated microspheres, Fig. 6.1(d), are functionalized with a oligonucleotide probe matching the DNA sequence of interest, Fig. 6.1(e). The functionalized microspheres are mixed into the fluorescently labeled sample and hybridized. Finally, a stringency wash is preformed to remove any non-specific hybridized sample, Fig. 6.1(f). At this point the hybridized spheres are introduced into the PFF devices and analyzed, Fig 6.1(g). The example in Fig. 6.1(g) illustrates detection of two different DNA sequences deviating in one base pair — an SNP. Here, only the sequence corresponding to the large particle is present in the sample, so only this size will show a fluorescence signal, indicated by filled circles. This is the principle of SNP detection in PFF. In Fig. 6.1, the focus is upon SNP detection, but in principle the method can be used in all analysis where sample specifically can be immobilized on the surface of microspheres.

6.2 Pinched flow fractionation devices

In this study the basic PFF layout described in Chap. 2 and pictured in Fig. 6.3(a) is used. The asymmetric outlet channels are designed to collect pinched particles smaller than 2.2 µm in radius in one outlet and larger particles in the other outlet. In this way two different DNA sequences can be separated for end analysis. The devices are fabricated in mr-I T85-20XP using planar nanoimprint lithography, as described in Chap. 3.

6.3 Preparation of the hybridized microspheres

Human genomic DNA samples
The relevant part of the HBB gene was obtained by PCR amplification, using the BCF and BCR primer pairs from Table 6.1. The study included genomic DNA from three individuals, two heterozygous and one homozygous for a mutation in the HBB gene. Both the homozygote (Mt/Mt) and one heterozyote (Wt/Mt) had the CD8/9+G mutation. The third individual was heterozygous for the CD24T>A mutation, and was used as a normal control (Wt/Wt) for CD8/9+G mutation. The PCR products were obtained from the Department of Hematology of the Herlev Hospital, University of Copenhagen.

Oligonucleotide probes and targets
A wildtype (Wt) and mutant (Mt) allele specific oligonucleotide (ASO) probe were designed for genotyping the CD8/9+G mutation in the HBB gene (see Table 6.1)

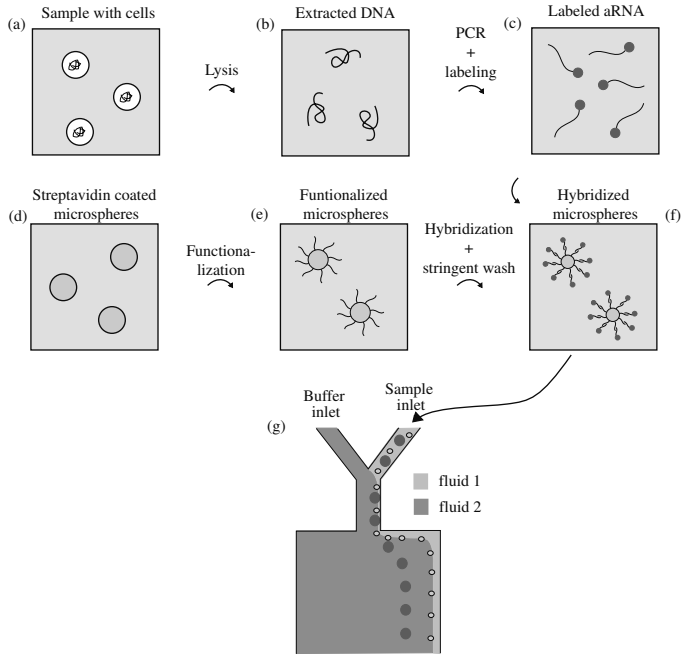

Figure 6.1: Overview of the steps involved in microsphere-based detection of single nucleotide polymorphisms (SNP) by pinched flow fractionation (PFF). (a) A sample including cells is withdrawn from a patient, (b) the cells are lysed to extract the DNA and (c) a relevant sequence of the DNA is amplified by PCR and fluorecently labeled. Parallel to this process streptavidin coated microspheres (d) are funtionalized by oligonucleotide probes (e). (h) The functionalized microspheres and the fluorescently labeled amplified sample are hybridized and exposed to a stringency wash to remove non-complementary bindings. (g) The hybridized microspheres are then separated due to size in the PFF device. In (g) only the sequence corresponding to the large microsphere is present in the sample, indicated by filled circles.

[167]. The probes contained a 5'-biotin for immobilization to streptavidin coated microspheres. Furthermore, the probes contained a spacer comprising ten thymidines upstream of the gene specific sequence. A wildtype (Wt) and mutant (Mt) oligonucleotide target were also designed to simulate the CD8/9+G mutation (see Table 6.1) [167]. However, these oligonucleotide targets were only 42 bp's in length, compared to the 300 bp PCR amplified human genomic DNA sample.

Attachment of probes to microspheres

3.09 µm and 5.6 µm streptavidin-coated polystyrene microspheres (Bangs Laboratories, Fishers, IN) were used in the study. 5'-biotin modified allele specific oligonucleotides (probes) were bonded to the microspheres using the procedure delivered by Bang laboratories [168], using 1 µg/µL of the 5'-biotin modified allele specific oligonucleotides. The microspheres were stored at 4 °C, suspended in wash/binding buffer (20 mM Tris pH 7.5, 1 M NaCl, 1 mM EDTA, 0.0005 % w/w Triton®-X100) until use. Both microsphere sizes were functionalized with the Wt or Mt probe to test the independence of sphere size.

Oligonucleotide	Sequence
Wt probe	5'-Biotin-TTTTTTTTTTTTTTTTTTTT GGAGAAGTCTGCC-3'
Mt probe	5'-Biotin-TTTTTTTTTTTTTTTTTTTT GAGAAGGTCTGCC-3'
Wt target	5'-Cy5-CAGGGCAGTAACGGCAGACTTCTCCTCAGGAG TCAGATGCAC-3'
Mt target	5'-Cy5-CAGGGCAGTAACGGCAGACCTTCTCCTCAGGA GTCAGATGCA-3'
BCF	5'-AGCAGGGAGGGCAGGAGCCA-3'
T7-BCR	**5'-GAAATTAATACGACTCACTATAGGGAGA**AGAG TCAGTGCCTATCAGAAACCC-3'
BCR	5'-AGAGTCAGTGCCTATCAGAAACCC-3'

Table 6.1: DNA oligonucleotide probes, targets and primers used in the study. T7 promoter sequence is denoted in bold.

Target preparation and labeling
Preparation of the patient DNA (PCR product), described earlier, was carried out using a reverse primer T7-BCR containing the T7 promoter sequence in the 5' end (Table 6.1). The resulting amplified RNA (aRNA) is the sample that is used in the SNP detection. The above step was performed as described by Petersen et al. [169], with the exception that direct labeling was performed using 12.5 µM (2.5 % v/v) of Cy3-CTP (GE Healthcare Bio-Sciences Corp, Piscataway, NJ).

Hybridization and stringency wash
The functionalized microspheres were hybridized in a total volume of 200 µL containing 100 nM of complementary wildtype (Wt) or mutant (Mt) Cy3 labeled oligonucleotide target (Table 6.1) in the wash/binding buffer. Hybridization was performed for one hour in an incubator at 26 °C with gentle agitation. In the case of aRNA sample, the microspheres were hybridized with a mixture consisting of 100 µL of aRNA, and 100 µL of the wash/binding buffer, using hybridization conditions as above. Following hybridization, a stringency wash was performed by washing the microspheres briefly in 200 µL wash/binding buffer, followed by two washes using 200 µL 0.1 x SSC + 0.1 % v/v SDS (oligonucleotide targets) or 0.5 x SSC + 0.1 % v/v SDS (aRNA). Each washing step was performed at 26 °C for 15 min with gentle rotation. The washing liquid was removed by centrifugation (10000 rpm for 3 min).

Genotyping using PFF
After the stringent wash, the microspheres were dispensed in a filtered (filter pore size: 0.2 µm) carrier buffer, 0.1 x SSC + 0.1 % v/v SDS (oligonucleotide target) or 0.5 x SSC + 0.1 v% SDS (aRNA target), to a microsphere concentration of 0.1 % w/v. The suspended microspheres were introduced into the PFF device from the sample inlet and carrier buffer without microspheres from the buffer inlet (see Fig. 6.1(g)). The flowrate of the buffer inlet and the bead inlet were 600 µL/h and 5 µL/h respectively during the measurement, both controlled by syringe pumps. Fluorescently labeled targets on the microsphere surfaces were detected, utilizing the measurment setup described in Chap. 2.

6.4 Screening for suitable stringency buffer

The buffer, used for stringent wash and as carrier buffer during genotyping SNPs in the PFF device, was the same throughout the study. The buffer served two purposes: 1) allowing for washing of the target that was hybridized to non-complimentary oligonucleotide probes, while maintaining fluorescent signal from hybridized Cy3-labeled oligonucleotide or aRNA targets with complementary oligonucleotide probes and 2) avoiding clogging of microspheres in the microfluidic channels.

During the study it was noticed that the stringency wash parameter was critical to the performance of the device, microfluidic channels clogged when the Na^+ concentration was too high. This tendency was empirically investigated by observation of the aggregation of hybridized microspheres as a function of the Na^+ concentration. It was observed that too high Na^+ concentrations led to cross-linking of microspheres (aggregation), perhaps due to unspecific hybridization. At the same time the hybridized targets were washed of the microspheres at too low Na^+ concentrations. An optimal Na^+ concentration within the two extremes exists. Results of the buffer optimization for homozygote mutant aRNA are seen in Fig. 6.2.

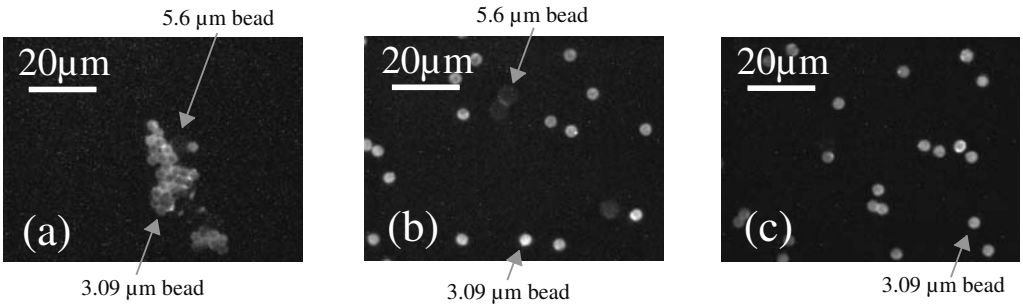

Figure 6.2: Empirical determination of the optimal Na^+ concentration in the buffer for stringency wash and genotyping measurements with aRNA. Fluorescence micrographs of 3.09 µm (Mt) and 5.6 µm (Wt) beads, hybridized with Cy3-labelled Mt/Mt aRNA and using three different Na^+ concentrations: (a) 1000 mM, (b) 168 mM, and (c) 86 mM NaCl for stringent wash and as carrier buffer.

The optimized Na^+ concentrations of the buffer were found both for the oligonucleotide targets and aRNA targets. The Na^+ concentration was varied from 20 mM to 1000 mM. The optimized buffers were found to be 0.1 x SSC and 0.1 % v/v SDS (20 mM Na^+) for oligonucleotide targets and 0.5 x SSC and 0.1 % v/v SDS (86 mM Na^+) for aRNA targets. Slightly different buffers for synthetic oligonucleotide and aRNA is expected. RNA can produce strong hairpin structures that typically weaken the bond of hybrids [170]. This probably explains why the aRNA target required less stringent washing conditions than synthetic oligonucleotides. Three examples of the optimization for aRNA are shown in Fig. 6.2(a)–6.2(c) with Na^+ concentrations of 1000 mM (Binding/wash buffer described in the last section), 168 mM (1.0 x SSC and 0.1 % v/v SDS), and 86 mM (0.5 x SSC and 0.1 % v/v SDS). The ratio of the average fluorescence signal from the 3.09 µm beads (Mt) compared to the 5.6 µm beads (Wt) in the three pictures is constant, approximately 3.5. When the Na^+ concentration was

below 86 mM the ratio increased — aRNA was washed off, especially from the large spheres. As seen in the three images in Fig. 6.2, the aggregation between spheres was reduced significantly as the Na^+ concentration was lowered.

6.5 Characterizing the system with oligonucleotide target

The functionality of the device was demonstrated with Cy3-labeled oligonucleotide targets. Two samples of oligonucleotide targets, Wt and Mt (Table 6.1), were analyzed in the PFF device (Fig. 6.3). Fig 6.3(b) is a bright field microscope image of the separated 3.09 µm (Mt) and 5.6 µm (Wt) microspheres. Fig. 6.3(c) and 6.3(d) are fluorescence images showing the analysis of the Wt and Mt oligonucleotide target respectively. As seen in Fig. 6.3(c), only the signal from the Wt microspheres was detected when hybridization was performed with Wt oligonucleotide targets. When the microspheres on the other hand were hybridized with Mt oligonucleotide targets, only the signal from the Mt microspheres was detected, as seen in Fig. 6.3(d).

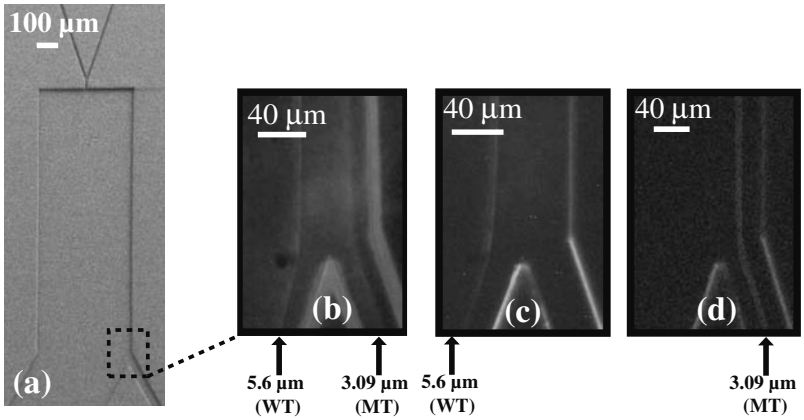

Figure 6.3: Genotyping in the PFF using oligonucleotide target. All images are at the transition between the broadening segment and the outlet channels as illustrated in (a). (b) Bright field microscope image showing separated 3.09 µm (Mt) and 5.6 µm (Wt) microspheres. The size and functionalization is indicated below the arrows, which point to the fluorescent microsphere streams. Fluorescence microscope image of: (c) 3.09 µm and 5.6 µm microspheres hybridized with wild type (Wt) Cy3 labeled oligonucleotide target and (d) 3.09 µm and 5.6 µm microspheres hybridized with mutant type (Mt) Cy3 labeled oligonucleotide target.

6.6 Genotyping human sample using size separation

The device (Fig. 6.3(a)) was tested by target deriving from genomic samples, described earlier, to investigate the mutation status of three subjects. Fig. 6.4(a) is a bright field microscope image demonstrating the separation of the 3.09 µm (Mt) and 5.6 µm (Wt) microspheres into two streams. Fig. 6.4(b-d) are fluorescence images showing the analysis of the Wt/Wt, Wt/Mt, and Mt/Mt sample respectively. As seen in Fig 6.4(b) only

the signal from the Wt microspheres was detected when hybridization was performed with Wt/Wt targets. When the microspheres were hybridized with Wt/Mt targets, signals from both microsphere sizes were detected, as seen in Fig. 6.4(c). Finally, when the microspheres were hybridized with Mt/Mt targets, only the signal from the Mt microspheres was detected, as seen in Fig. 6.4(d). Conclusively, successful analysis of the human DNA sample was performed with the PFF device.

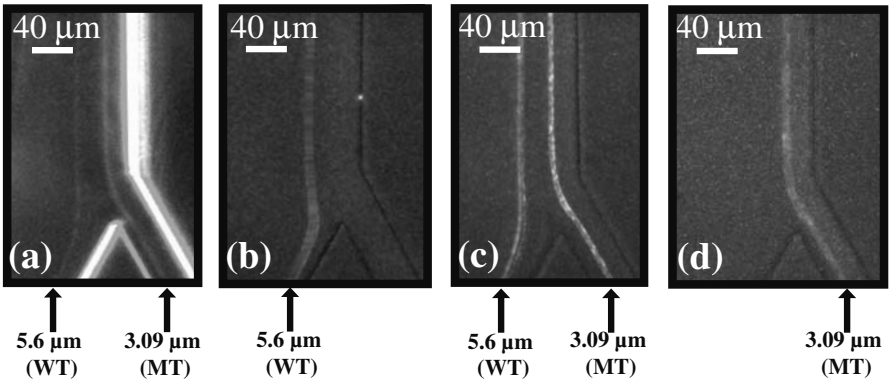

Figure 6.4: Genotyping in PFF using aRNA target. All images are at the transition between the broadening segment and the outlet channels. (a) Bright field microscope image showing separated 3.09 µm (Mt) and 5.6 µm (Wt) beads. The size and functionalization is indicated below the arrows, which point to the fluorescent bead streams. Fluorescence microscope images of: (b) beads hybridized with homozygote Wt/Wt aRNA, (c) beads hybridized with heterozygote Wt/Mt aRNA, and (d) beads hybridized with homozygote Mt/Mt aRNA.

6.7 Comparison with other SNP analysis platforms

Pinched flow fractionation is a flexible genotyping LOC platform, which can be reused, and does not include any critical steps such as functionalization of the device with DNA probes [158, 159, 160, 167]. Results presented in Chap. 2 suggest that the PFF platform can be extended for simultaneous detection of many SNPs, e.g. by adding up to 11 microsphere sizes and/or fluorescent microsphere color combinations. The platform will thereby compete with existing microsphere-based SNP genotyping platforms such as the xMAP platform from Luminex and share benefits associated with these including ease of use, statistical superiority, faster hybridization kinetics and more flexibility in preparation of arrays, when compared to planar arrays [163, 171]. The xMAP system from Luminex can resolve 100 analytes (50 SNPs) using 100 differently spectrally encoded microspheres [172]. In comparison to the xMAP technology from Luminex, the PFF platform will probably not have as high multiplex capacity but offers several advantages which make it attractive for LOC applications. Firstly, the PFF device is fabricated on a LOC platform and can therefore be integrated with other LOC components, such as polymerase chain reaction (PCR) chambers [164], enabling integration of the steps illustrated in Fig. 6.1. Secondly, the PFF platform also enables collection of the separated targets e.g. for downstream analysis of the captured biomolecule. Thirdly, the Luminex flow cytometer system includes an advanced

spectral set-up consisting of two lasers and two detectors for the analysis of the hybridized microspheres. In the PFF platform, the spatial separation of the hybridized microspheres requires a simpler detection system with only one excitation light source and one detector. Fourthly, only two small pumps are needed to ensure separation, and thereby the necessary conditions for genotyping, of the hybridized microspheres. Fifthly, the estimated price of a PFF SNP detection system including 10 micro-devices are 10 kEuro compared to 120 kEuro for a standard solution from Luminex. These advantages of PFF suggest that it is a strong candidate technology for LOC based DNA genotyping. In addition to SNP genotyping, the PFF technique can also be applied for other diagnostic applications. For example, using microspheres conjugated with antibodies for detection of viral and bacterial infection, or using microspheres to look for the presence of biomarkers in order to use the PFF as a general method for resolving multiplexed molecular reactions.

6.8 Summary

In this chapter a platform for genotyping single nucleotide polymorphisms (SNPs) using pinched flow fractionation (PFF) is demonstrated. By addressing allele specific probes (wild-type and mutant) to two differently sized microspheres and subsequently separating the microspheres according to size, genotyping was performed. The PFF device is designed so each microsphere size and therefore allelic variant is collected in individual outlets enabling end point analysis. The platform was demonstrated both with synthetic and genomic DNA from three individuals with a mutation in the HBB gene. The microsystem is generic and is only limited by the number of bead sizes that can be separated and bead colors that can be distinguished. Resolution measurements presented in Chap. 2 indicates that approximately 11 different microsphere sizes, corresponding to 5 SNPs, can optically be separated in the PFF device. Combining this with e.g. three different color codes of the spheres, genotyping of 15 SNPs is possible, which is enough for a commercial attractable point-of-care system.

Chapter 7

Nano-scale separation

Proteins are essential parts of living organisms as they participate in virtually every process within a cell, carrying out the duties specified by the information encoded in their genes. Studies of their structure and functions (proteomics) is today usually performed by electrophoresis and to some extent by flow cytometry. Electrophoresis is very powerful in its selectivity and speed. However, large samples are needed in the process. Flow cytometry is carried out with cell sized samples, either to count single cells or measure the surface chemistry. Flow cytometry is often used in combination with an array of differently functionalized microspheres to detect biomolecules matching the probes on the microspheres, as described in Chap. 6. Today, one of the "hot" topics in proteomics is single cell analysis — to count the different proteins in a single cell. It is not possible to detect such small amounts of proteins either in electrophoresis or flow cytometry, without prior expensive and time consuming sample amplification. This has led to the development of new techniques for single cell proteomics. Pinched flow fractionation (PFF) has the potential for single cell proteomics, and its simple layout, compared to other on-chip methods listed in Chap. 1, Table 1.2, facilitate high volume fabrication schemes as roll-to-roll based methods, presented in Chap. 3. However, to realize this, a down-scaling of the dimensions in the PFF device presented in prior chapters is necessary.

The work presented in this chapter describes the first steps towards a single-protein separation system based on PFF. Initially, the consequences of a down-scaling from micro to nano-scales are discussed, followed by a description of the fabrication of devices, the measurement setup and also the samples that are introduced into the system. Afterwards, device characterization and surface funtionalization to prevent proteins from immobilizing on surfaces are described. To round-up the chapter, an improved device layout is proposed and the results are summarized.

7.1 From micro to nano

Liquids are quantized on molecular length scales, $\sim 0.3\,\mathrm{nm}$, but they appear continuous in most LOC systems, which are usually larger than $1\,\mu\mathrm{m}$. In micro-scale LOC systems the continuum hypothesis can therefore be assumed as valid. The continuum hypothesis states that the macroscopic properties of a fluid are the same everywhere if the fluid is perfectly homogeneous in structure and does not consist of discrete molecules,

as in reality. If a fluidic volume contains a sufficiently large number of molecules, all physical quantities such as energy, mass and momentum of the volume can be taken as the sum of the corresponding quantities for all the molecules.

In the models presented in Chap. 2 for micro-scale PFF (μPFF), fluids are considered continuous. Though, when handling fluids in nano-scale structures ($<$ 1 μm) this assumption may not necessarily be valid anymore. So at what length scale do fluids start acting as discrete molecules? As the microscopic length scale of liquids, ~ 0.3 nm, is approached, the continuum hypothesis must break down. Today, there is no exact known numerical value. However, a qualitative analysis is possible. Lets imagine a small cubic fluidic volume. This fluid volume can be considered continuous when it is sufficient large, so that the average number of molecules or particles is constant, only with small statistical fluctuations. If the number of molecules in the volume are set to fluctuate at a maximum of 0.5 % and the molecular distance in the liquid is ~ 0.3 nm, the volume must contain 4×10^4 molecules and have a side length of ~ 10 nm [129]. During the nano-scale separation presented in this work channels down to 480 nm in width are tested for separation of particles with a radius of 22 nm and 50 nm. These values are still larger than the 10 nm limit. However, when the nano-scale particles are aligned in the pinch segment, the width of the sample fluid is on the order of 20 nm. In the nano-scale PFF (nanoPFF) measurements, the continuum hypothesis is therefore challenged, and quantized effects might appear.

7.2 Experimental details

The device layout of the nanoPFF are basically the same as in the μPFF, presented in Chap. 2. Two inlet channels merge together in a pinch segment, followed by a broadening segment, which ends out in two outlet channels. The layout of nanoPFF is illustrated in Fig 7.2(a). The inlet and outlet channels are 10 μm wide and 9 mm long. 170 μm before the inlet channels meet they narrow down in two steps, first to 2 μm (length 167 μm) and then to the width of the pinch segment (length 3 μm). The pinch segment is 480 nm wide and 2 μm long. The broadening segment is 50 μm wide and 195 μm long. All channels are 495±2 nm high.

In μPFF separation of microspheres with a radius down to 2.2 % of the width of the pinch segment is possible. As a result of these measurements, the nanoPFF device is expected to enable separation of nanospheres with radii as small as 11 nm.

7.2.1 Fabrication of devices

Devices are fabricated in silicon dioxide (SiO_2), defined by electron beam lithography (EBL) and transferred into the SiO_2 by reactive ion etch (RIE), using a double thermal oxidation scheme [173].
A 495±2 nm thick SiO_2 layer was thermally grown on a 4 inch single polished (100) silicon wafer by wet oxidation (1000 °C, 90 min). Afterwards, a 450 nm thick layer of positive electron beam sensitive resist (ZEP520A, Marubeni Europe Plc, London, England, http://www.europe.marubeni.com) was spin coated on the SiO_2, and 15 nm of aluminum (Al) was thermally deposited (QCL 800,Wordentec, Devon, England, http://www.wordentec.com) on top of the resist. The Al layer serves as a conductive layer to avoid charge build up during the electron-beam (e-beam) exposure and

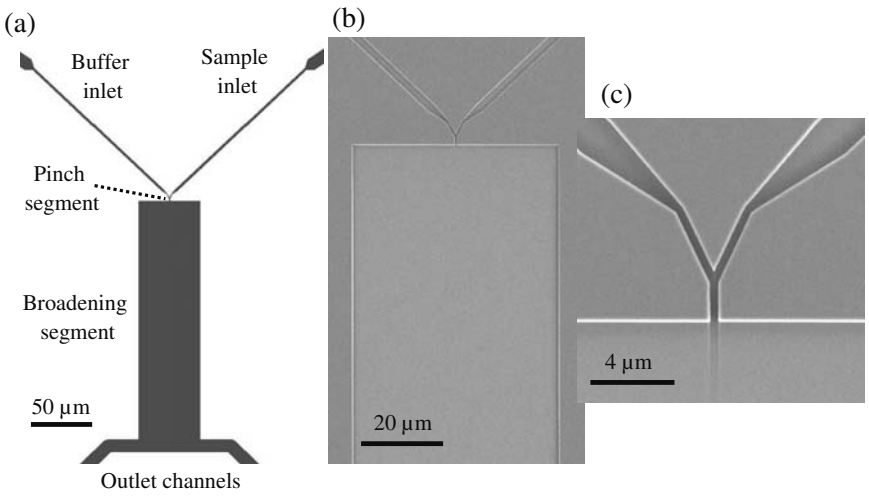

Figure 7.1: a) The layout of the nano-scale pinched flow fractionation (nanoPFF). (b+c) Scanning electron microscope (SEM) image of the pinch and broadening segment and of the pinch segment alone, respectively. The channel height is 495 nm

does not broaden the incoming e-beam. Devices were defined in the resist by an electron beam writer (JEOL-JBX9300FS, dose: 250 µC/cm^2, current: 10 nA, step size: 10 nm). The Al layer was removed at a 50 s dip in MF322 (Candor Kemiske A/S, Vejle, Denmark, http://www.candordenmark.dk) and the exposed resist was afterwards developed in a 2 min dip in ZEP-N50 (Marubeni Europe Plc, London, England, http://www.europe.marubeni.com). The SiO_2 underneath the openings is etched in a reactive ion etch (CF_4: 16 SCCM, CHF_3: 24 SCCM, Power: 60 W) using the underlying Si layer as etch stop. The etch rate at the largest structures (broadening, inlet and outlet channels) was 36 nm/min but is smaller in the pinch segment due to limited access of reactive ions. To ensure that the SiO_2 was entirely removed in all channel parts, the etch time was 18 min. It was observed that, due to heating of the system during etching, the etch rate in the masking resist was increased, resulting in insufficient masking. By dividing the etch into a total of nine intervals of 2 min, flushing the etching chamber with nitrogen in between, heating of the system was avoided. Afterwards, a 20 nm layer of SiO_2 was grown on the wafer by dry oxidation (1000 °C, 20 min) to ensure a hydrophilic channel floor. Inlet and outlet holes were then powder blasted and finally the structures were sealed with a borofloat glass lid by fusion bonding [173]. Scanning electron microscope (SEM) images of devices before bonding are shown in Fig. 7.2(b) and 7.2(c).

7.2.2 Measurement setup

The distance between the center of separated fluorescently labeled particles and the channel wall in the broadening segment, y', was determined optically utilizing an inverted fluorescent microscope (Eclipse2000, Nikon) in combination with an EMCCD camera (Cascade 512II, Photometrics, Tucson, United States). Contrary to the µPFF measurements, y' is not found for the individual particles, but for all of them in a cross-sectional light intensity scan across the broadening segment. A 60x water im-

mersion microscope objective (NA=1.00, Nikon, Surrey, United Kingdom) combined with a 1.5x camera lens was used to get the necessary resolution and collection of light.

The flow in the two inlet channels was pressure controlled, using nitrogen pressure bottles in combination with needle valves (EW-06393-70, Cole Parmer) enabling a resolution of 1 mbar. Fluidic connections to the devices were ensured by clamping onto a holder. O-rings, classified to a maximum pressure of 7 bar, were used to ensure tight connections. The pressure in the inlets could consequently be varied from 0 bar to 7 bar.

7.2.3 Sample

In all measurements fluorescent labeled polystyrene (PS) nanospheres (Thermo Fisher Scientific Inc, Waltham, USA, http://www.thermo.com) with two different average radii, namely 22 nm and 50 nm, and having a standard deviation of $< 15\%$ (3.3 nm) and $< 10\%$ (5 nm) respectively, were used. The fluorescent color of the 22 nm nanospheres are green and red in the case of 50 nm nanospheres. The nanospheres are suspended in a filtered carrier buffer (pore size: 20 nm) consisting of 0.001 % w/w Triton X100 in MilliQ water. The nanosphere concentration is 0.01 % w/v.

7.3 Separation measurements

Contrary to the μPFF measurements, diffusion is of great importance in nanoPFF. In the numerical model describing the flow in μPFF, see Chap. 2, diffusion during expansion in the broadening segment was estimated to be insignificant and was therefore neglected. In the presented nanoPFF measurements, particles are typically traveling at approximately 0.0075 m/s during the first 2 μm of the broadening segment (the most intense expansion region). In addition, the diffusion constant scales linearly with particle radius, according to the Einstein-Stokes equation (Chap. 2), and is more than a of factor 10 larger for nano-scale spheres compared to micro-scale spheres. The resulting diffusion in the expansion region is calculated, using the Einstein-Stokes equation, to be 72 nm and 48 nm for nanospheres with a radius of 22 nm and 50 nm respectively. If it is assumed that the spheres are aligned against the wall in the pinch segment, this corresponds to 3.5 μm and 4.5 μm in the broadening segment, which is larger than the expected 1.4 μm separation of the two sizes. Consequently, diffusion must be included in the numerical model. The model will, by such addition, be used to back-track the nanosphere distributions in the broadening segment to a distribution in the pinch segment, thereby revealing the spatial distribution in nano-scale pinched channels, which can be used to increase the understanding of flow in such systems.

The same COMSOL Multiphysics numerical model as presented in Chap. 2 is used to calculate the flow in nanoPFF. Diffusion is included by adding the convection and diffusion module of COMSOL to the model. First, the time independent Navier-Stokes equation is solved for the pressure driven nanoPFF layout. Afterwards, using the calculated flow field, diffusion in the system is calculated, setting the diffusion constant in the channels to be equal to the one of relevant particle size. In the convection and diffusion module, the channel walls, with exception of the entrance of the pinch and exit of the broadening segment, are set to be insulating. Concentration can therefore not leave the channels through these walls. A concentration flux is allowed at the exit

of the broadening segment, and a concentration distribution is added at the entrance of the pinch segment, equivalent to a particle concentration after the pinching point. The size distribution of the nanospheres is Gaussian [134], and the concentration distribution in the model is therefore also set to be Gaussian with the standard deviation of the nanosphere sample. The Einstein-Stoke diffusion constant of the nanospheres is $9.76 \cdot 10^{-12}\,\mathrm{m}^2/\mathrm{s}$ ($r = 22\,\mathrm{nm}$) and $4.29 \cdot 10^{-12}\,\mathrm{m}^2/\mathrm{s}$ ($r = 50\,\mathrm{nm}$). The average velocity in the broadening segment was measured tracking nanospheres with a radius of 50 nm, and this velocity was used in the flow calculation.

To characterize nanoPFF and to validate the numerical model, the two nanosphere sizes ($r = 22\,\mathrm{nm}$ and $r = 50\,\mathrm{nm}$) suspended in buffer were introduced from the sample inlet channel and buffer without nanospheres from the buffer inlet. The pressure at the sample inlet was set to 1669 mbar and 4003 mbar at the buffer inlet. At these pressures the average velocity in the broadening segment was measured to be 186 µm/s. Because of the different fluorescence properties of the two microsphere sizes, they could be imaged individually. The resulting microsphere distribution is shown in Fig. 7.2(a) and 7.2(b), along with the corresponding COMSOL simulations (the insets). In the COMSOL simulations, the average position of the Gaussian concentration distribution at the entrance of the pinch segment is set so that the average position in the broadening segment equals the measurement in the broadening segment. The standard deviation of the concentration distribution in the beginning of the pinch segment is set to the value of standard deviation of the microspheres given by the manufacturer (3.3 nm for $r = 22\,\mathrm{nm}$ and 5 nm for $r = 50\,\mathrm{nm}$).

As seen from Fig 7.2(c) and 7.2(d), the measured distribution does not decrease as fast as the calculated distributions. The central part of the distributions are similar, but the measured distribution has "tails" in the outer regions, which are not present in the calculated ones. These tails most likely originate from leached dye from the nanospheres, which could be caused by their old age (> 3 years). During the measurements it was observed that buffers with suspended spheres were slightly fluorescent, which was not the case with buffers without spheres. The large diffusion constant of the dye, which is on the order of large molecules ($\sim 10^{-10}\,\mathrm{m}^2/\mathrm{s}$), cause the dye molecules to spread out much more than the nanospheres. According to COMSOL calculations of dye molecules, these are responsible for the observed tails. The dye is not a physical measure of the nanosphere distribution, and is therefore not implemented in the COMSOL calculation. If the dye contribution is extracted from the measured distribution in Fig. 7.2(c) and 7.2(d) and a Gaussian distribution is fitted to the resulting distribution, the standard deviation in y' of these distributions is found to be 6.3 µm ($r = 22\,\mathrm{nm}$) and 4.3 µm ($r = 50\,\mathrm{nm}$), measured 70 µm into the broadening segment. The calculated standard deviations in y', using the standard deviation of the nanosphere sizes given by the manufacturer, is 6.7 µm and 4.5 µm respectively, deviating by 6% and 4% from the measured values. Surprisingly, the calculated standard deviations are larger than the measured values, which indicates that the standard deviation of the samples are less than the maximum standard deviation, stated by the manufacturer. If this is the case, the real nanosphere standard deviation is calculated to be 14.1% and 9.4% for the 22 nm and 50 nm spheres, respectively.

From the COMSOL calculations presented in Fig. 7.2 the average distance from the channel in the pinch segment of the 22 nm and 50 nm nanospheres is found to be 161 nm and 169 nm respectively. This is much further from the channel wall compared to phys-

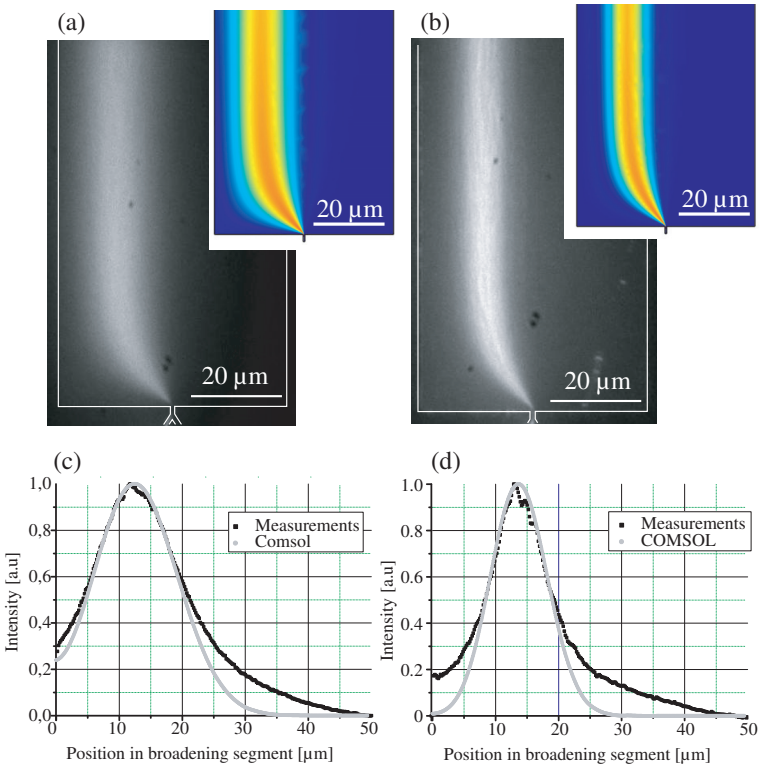

Figure 7.2: Characterization of the nanoPFF device and comparison with COMSOL simulations. Nanospheres with a radius of 22 nm and 50 nm were introduced into the sample inlet at 1669 mbar, and buffer from the buffer inlet at 4003 mbar. The two nanosphere sizes posses different fluorescence properties, and can therefore be imaged independently. (a) Fluorescence settings, enabling visibility of only the 22 nm spheres. (b) A different fluorescent setting, and only the 50 nm spheres are visible. The inset in the figures are COMSOL simulations with similar flow conditions. (c+d) Intensity scans from the broadening segment, 70 µm from the pinch segment, of the measurements compared to the calculated results from COMSOL.

ical alignment against the channel wall, which could indicate that the microspheres are not pinched. However, the width of the measured distributions in the broadening segment corresponds to a standard deviation in the pinch segment equal to the one of the nanosphere sizes, indicating that the spheres are confined as much as possible in the width position of the pinch segment. One plausible explanation to such confinement without an alignment against the wall is the lift forces, introduced in Chap. 2. The lift force will, according to Yapici et al. [132] describing high solid concentration suspensions ($> 10\,\%$w/v) at low Reynolds numbers ($\ll 1$), effect the nanospheres to be forced towards the center of the channel. According to Di Carlo et al. [133], describing low solid concentrations (no particle interactions) at high Reynolds numbers (> 1), the nanospheres are affected towards an equilibrium position in between the center and the walls depending on its size. Both of the above descriptions have only been verified in micrometer scale systems. In the nanoPFF measurements the Reynolds number is $\ll 1$ and the solid concentrations are low ($0.01\,\%$w/v). The two descriptions of the lift

force do not cover the experimental conditions. As a first approach, the model by Di Carlo is used to describe the observation. According to this model the two relevant sphere sizes, $r = 22\,\text{nm}$ and $r = 50\,\text{nm}$, will be affected rather differently. The small spheres will experience a very small lift force ($\sim 10^{-21}\,\text{N}$). Assuming these are pinched initially in the pinch segment, they will be moved approximately 6 nm towards the center during their 70 µs travel time in the pinch segment. The large particles on the other hand will experience a larger force ($\sim 10^{-18}\,\text{N}$) and will be moved approximately 42 nm towards the center. Consequently, the average distance from the channel wall to the center of the two sphere sizes will be 28 nm ($r = 22\,\text{nm}$) and 92 nm ($r = 50\,\text{nm}$), which is less than the observed 161 nm and 168 nm, respectively. According to Yapici, a force towards the channel center will, if the time a particle is affected by the force is long enough, be moved further towards the channel center. Further measurements, as described in Chap. 2, are needed to verify whether a lift force is responsible for the observed position in the pinch segment.

During the first measurements with nanoPFF it was observed that the maximum pressure ratio in the two inlet was 1:4. If the ratio was larger, a back-flow occurred in the inlet channel with the smallest applied pressure. According to µPFF measurements, this ratio is not large enough to align the nanospheres against the wall in the pinch segment. In analog with the µPFF measurements, the flow rate ratio should be approximately 1:60 to pinch spheres with a radius down to 22 nm in the 480 nm wide pinch segment. A future device layout, enabling such flow ratios, is discussed later in this chapter. At measurements with such devices, the nanospheres can be pushed closer to the pinching wall if possible, and the above claim concerning a lift force can be proved or disproved.

From the measurements presented in Fig 7.2, the maximum of the distributions in the broadening segment of the two nanosphere sizes was observed to be separated by 1.4 µm, as shown in Fig 7.3(a). However, a physical separation is not achieved because of the large diffusion in the system. In one device out of seven, a completely different flow was observed. A cross-sectional intensity scan at the measuring point, in the broadening segment 70 µm from the pinch segment, is shown in Fig 7.3(b). This flow pattern was reproducible in the device, but could not be obtained in any of the 6 other nanoPFF devices tested in this work. The separation could therefore originate from a defect in the device, which affects the larger spheres to be displaced further form the channel wall. Such "defect" enhancement the separation was very welcome. However, because of the covalent bonding of the lid, it was not possible to open the device and examine the defect.

Measurements at the same flow rate ratio as used in Fig 7.2 and Fig 7.3, but with a buffer inlet pressure of 7 bar, showed a decrease in the width of the particle distribution of approximately 30 %. Conclusively, the driving pressure must be as high as possible to lower the diffusion during separation in future nanoPFF measurements.

7.4 Preparation for protein separation

Changing the sample from polystyrene microspheres to bio-molecules such as proteins is challenging. Proteins tends to be adsorbed non-specifically on surfaces. Nonspecific protein adsorption to the surface may cause clogging in highly concentrated samples,

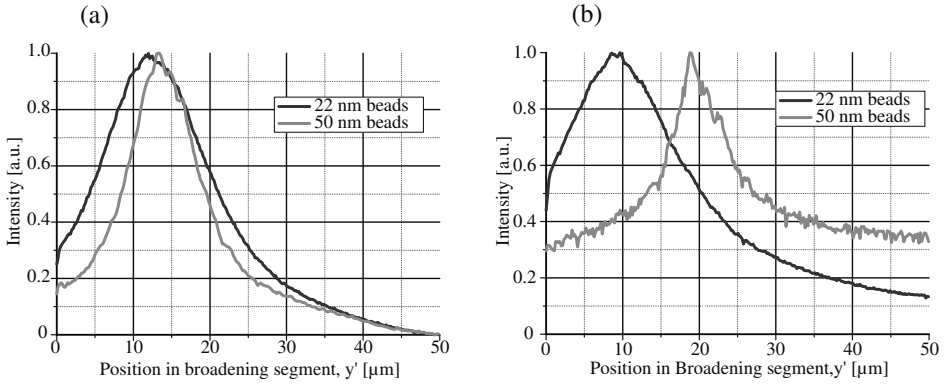

Figure 7.3: Nano-scale separation measurements in pinched flow fractionation with two different sphere (bead) radii (22 nm and 50 nm). The two sizes are labeled with different fluorescent markers, enabling individual imaging. In both graphs a light intensity scan across the broadening segment, 70 µm from the pinch segment, is shown. a) Nanosphere distributions with a sample inlet pressure of 1669 mbar and a buffer inlet pressure of 4003 mbar. b) An increased separation was observed in one device using the same pressure in the two inlets. This enlarged separation is believed to originate from a defect.

whereas in the case of low concentration, as in single cell proteomics, the proteins will be adsorbed on the surface before reaching the relevant point in the device, e.g. the broadening segment in PFF. It is therefore crucial to include a surface-modification protocol that efficiently reduces nonspecific adsorption of proteins. One popular molecule for surface passivation in fluidic environments is the poly(L-lysine)-g-poly(ethylene glycol) (PLL-g-PEG). PLL-g-PEG has been demonstrated to reduce protein adsorption drastically on metal oxide surfaces [174], polymer surfaces e.g. Topas® and PMMA [175] and silicon dioxide surfaces [176]. A PLL-g-PEG monolayer is self-assembled on the surface, with the positively charged PLL backbone electrostatically bonded to a negatively charged surface and an uncharged PEG chain exposed to the sample. The protein repellent properties of PEG are not fully understood, however the dominant mechanisms are expected to originate from steric repulsion preventing contact to the underlying surface, and a hydration shell around the PEG chain which energetically suppresses adsorption [175].

In this section binding of PLL-g-PEG is demonstrated on Topas® surfaces in µPFF devices and subsequently on the silicon dioxide surfaces in nanoPFF devices. The surfaces are activated (made negatively charged) for PLL-g-PEG binding by flushing with 50 % HNO_3. As demonstration of successful binding, the PLL-g-PEG (PP) at 10 µg/mL is introduced from one inlet channel and biotin modified PLL-g-PEG (PPb) and PP mixed in a 1:1 ratio at 10 µg/mL from the other inlet. Afterwards Cy3 labeled streptavidin (SA-Cy3) mixed in a 1:10 ratio with streptavidin (SA) at 10 µg/mL is flushed through the device from both inlet channels. Streptavidin is expected to be repelled from PP and adsorbed on the PPb coated surfaces, thereby leaving a non-fluorescent and fluorescent surface respectively. Examples of the surface treatment are shown in Fig. 7.4. A flow rate ratio in the two inlet channels equal to 1:1 during coating with PP and PPb, is shown in a µPFF device in Fig. 7.4(a), and two examples of nanoPFF devices are shown in Fig. 7.4(b) and 7.4(c), with a flow rate ratio of 4:1 and

1:1 respectively. The image in Fig 7.4(c) is taken at the broadening segment. As seen in Fig. 7.4(b) the fluorescent signal is low, and is decreasing along the broadening segment. The reason is that the inlet coated with PPb clogged shortly after introduction of SA-Cy3. This is a good illustration of what is tried to be avoided with the PP coating.

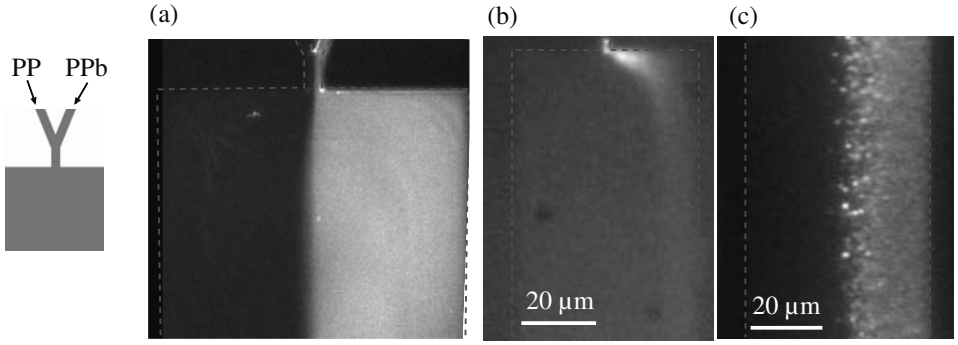

Figure 7.4: Surface functionalization with PLL-g-PEG (PP). The PP coating is demonstrated by introduction of PP in the left inlet channel and biotin modified PP (PPb) in the right inlet channel. Afterwards the entire device is flushed with Cy3 labeled streptavidin, which is expected to be repelled by PP and adsorbed at the PPb. (a) Surface coating in a micro-scaled PFF device, where the flow rate ratio in the two inlets was 1:1 during coating with PP and PPb. This experiment was made by Rodolphe Marie at DTU Nanotech. (b+c) Surface coating in nanoPFF. The flow rate ratio is 5:1 and 1:1 respectively.

Overall, a protocol for PLL-g-PEG coating of PFF devices has been demonstrated. However, as seen from Fig. 7.4(c) there is still room for improvement, concerning more homogeneous coatings in nanoPFF.

7.5 Outlook - new device layouts

In the present design of the nanoPFF device the hydraulic resistance in the inlet channels are equal and 1.6 times smaller than the total resistance of the pinch segment, the broadening segment and the outlet channels. To enable a pinch condition for the 22 nm and 50 nm spheres a flow rate ratio in the two inlets of 1:60 ($Q_{sample} : Q_{buffer}$) is necessary according to the µPFF measurements. This can be ensured by a smaller hydraulic resistance in the buffer inlet compared to the sample inlet. In addition, the resistance in the sample inlet must be larger than the total resistance of the pinch segment, the broadening segment and the outlet channels to avoid back-flow. In a future design the broadening and outlet channels should be kept unchanged. The narrow part of the sample inlet channel should still match the width of the pinch segment, but be ten times as long (compared to the present setup), and the wide part five times more shallow. The narrow part of the buffer inlet should also match the width of the pinch segment where these meet, but be reduced two times in length, and the wide part should be increased by a factor of two in width. In this proposed design, the ratio of the hydraulic resistance between the two inlets are 10 and 3.4 between the sample inlet and the pinch, broadening and outlet segment. In addition, a reduction in the

width of the pinch segment of a factor 2 to 3 will most likely be necessary to enable separation of proteins down to 5 nm in radius.

Diffusion is, due to the nano-scale particles and low flow velocities, a significant limitation to the separation in nanoPFF. To lower diffusion to a level, at which complete separation is possible, the flow velocity must be increased at least a factor of ten, corresponding to a pressure in the inlet buffer channel of approximately 40 bar. The present measuring setup can only last 7 bars, so another connection between the device and holder is a necessary improvement.

Finally, a fabrication scheme including nanoimprinted polymer devices instead of the silicon based, presented in this chapter, should be developed to lower the production cost. The price for each nanoPFF silicon device is approximately 300 Euro, which is completely out of range in most price sensitive lab-on-a-chip markets. A stamp for planar nanoimprinted devices could be made similar to the silicon-based nanoPFF device, but instead of a positive e-beam sensitive resist, a negative resist would ensure stamp protrusions instead of channels. A 10 times reduction in price can be achieved by planar NIL and up to 1000 times reduction using roll-to-roll nanoimprint.

7.6 Summary

An approach towards nano-scale separation by pinched flow fractionation is introduced in this chapter with a special focus on protein separation. A nano-scale PFF device in silicon has been fabricated and the first characterization measurements of nanospheres 22 nm and 50 nm in radius are shown. Diffusion was observed to be a critical limitation to separation in the system, and a new measuring setup enabling inlet pressures above 7 bar should be developed. A numerical model in COMSOL Multiphysics is demonstrated by comparison with the experimental results, and used to convert nanosphere distributions in the broadening segment to a distribution in the pinch segment. This represents a powerful tool for imaging particle distributions in nano-scale pinch channels, and can probably be used to learn more about the physics of such systems. The nanosphere flow dynamics in the pinch segment is not fully understood, and a proposed new device layout is expected to provide such understanding. Throughout the measurements, there was no indication that the continuum hypothesis, discussed in the chapter, breaks down.

In addition, the PFF devices were prepared for protein handling, by coating the channel walls with PLL-g-PEG, which is a protein repellant molecule. In this way nonspecific binding of proteins to surfaces is drastically reduced.

Chapter 8

Microfluidic platform for time-resolved high intensity x-ray measurements

Up until this point, all work in this thesis has been concerned with pinched flow fractionation (PFF). In this chapter the focus change towards time resolved high intensity x-ray studies of sample in a microfluidic platform. At the annual meeting of the Danish physical society 2008, the author was contacted by Kristoffer Haldrup from the center of molecular movies (CMM) at the Niels Bohr institute, University of Copenhagen. He mentioned that they were looking for a microfluidic windowless platform for time-resolved high intensity x-ray studies, and asked if the author could come up with a design. The idea sounded very interesting and a good collaboration started. The resulting platform has received much attention in the time-resolved x-ray community and in future work it would be obvious to integrate PFF into the platform for sample pretreatment. The work concerning a windowless platform is therefore included in the thesis.

In this chapter, a windowless, microfluidic device based on an out-of-plane implementation of the capillary burst valve (CBV) principle is presented. The principle of a CBV is introduced and afterwards characterized with microsphere suspensions, protein samples and a highly photoactive platinum compound. The functionality is also demonstrated in vacuum, relevant at some x-ray measurements. Finally, the device is tested under realistic conditions at a time-resolved x-ray beamline, and an outlook for optimization of the device layout as well as a summary are given. Most of the work presented in the chapter is published in [177].

8.1 The necessity of a windowless microfluidic platform

The arrival of new X-ray Free Electron Laser (XFEL) sources is foreseen to greatly increase the amount of information that can be extracted from liquid-state experiments, due to the exceptional brilliance, time resolution and coherence properties [178] it presents. In order to take full advantage of the possibilities offered by the new

x-ray sources, some crucial points in sample handling will have to be addressed to preserve coherence, sub-ps time resolution and to prevent sample and device damage from the extremely bright x-ray pulse. These points are briefly described in Chap. 1, and some elaborating comments are given here. The brilliance (brilliance is defined as: $(photons/s)/(mrad^2\ mm^2\ 0.1\%\ bandwidth)$, increase by 10 orders of magnitude over current synchrotron sources. To prevent sample damage and debris build-up, the liquid sample should ideally be replaced between every x-ray pulse, which will come at 120 Hz at the Linac Coherent Light Source (LCLS) at Stanford and at 10 Hz/5 MHz at the European XFEL. In addition, any material in the x-ray beam path other than the sample will due to the high brilliance be damaged, and should therefore be avoided. Preserving the pulse-length limited time resolution dictates that the sample must be thin, due to the difference in light speed between a UV-VIS-IR laser pump pulse and the x-ray probe pulse as they propagate through the sample. The accumulated time difference Δt between the two pulses is given by, $\Delta t = \frac{l}{c}(1-n)$, where l is the path length, c is the speed of light and n is the refractive index of the media at a given pump pulse wavelength. Taking water ($n = 1.33$) as a typical example, a path length of 100 µm corresponds to a time delay between the pulses slightly larger than 100 fs, thus limiting the sample thickness to 50 µm–100 µm if 100 fs time resolutions are to be conserved in the case of co-propagating pump and probe beams [179]. Finally, to preserve the coherence of the x-ray beam and thereby ensure an atomic spatial resolution, the sample surface must not be curved, and the number of intermediate layers should be kept to a minimum. Existing measurement setups does not live up to the above requirements as discussed in Chap. 1. Thus, motivating the development of the windowless microfluidic platform presented in this chapter that does meets these requirements.

8.2 Principle of the capillary burst valve

The functionality of the windowless x-ray access hole in the proposed microfluidic platform is based on a capillary burst valve (CBV), suggested and tested earlier [180, 181]. CBVs rely on the surface tension of the liquid at a liquid/solid/gas interface and it consists of a narrow channel with a sudden widening at a given point along its length. The following description represents liquid in a hydrophilic channel. When a liquid reservoir is brought into contact with the narrow channel, the liquid is dragged into the channel by capillary forces. The liquid propagates with a characteristic contact angle, the angle between the channel wall and the liquid front, θ_c, see Fig. 8.1(a). This angle is identical to the contact angle of a drop of the same liquid on a flat horizontal surface. If the size of the channel abruptly increases with an angle, ϕ_{ch}, the liquid stops propagating due to the cost in energy associated with the significant increase in surface area. Additional energy in the form of an increase in the pressure has to be applied at the entrance of the narrow channel to restore the contact angle with respect to the surface connecting the narrow and wide channel segment, $\theta_{cb} = \theta_c + \phi_{ch}$. This is necessary for the liquid to continue along the wall into the wider channel segment. Figure 8.1(b) shows the situation just before the valve will burst. The central performance measure of a CBV is the burst pressure, Δp_b, and in previous work [180, 181, 182, 183] the burst pressure has been predicted and confirmed to be proportional to the liquid surface tension, γ, and inversely proportional with the channel dimension, D. The bursting pressure for a hydrophilic or hydrophobic channel with circular cross-section can be derived from the Young-Laplace equation, and is

given by Eqn. 8.1.

$$\Delta p_b = \frac{-4\gamma \cos\theta_{cb}}{D} \tag{8.1}$$

In previous demonstrations, the CBV has been placed in the plane of the microfluidic network, e.g. for use in microfluidic centrifugal systems [184, 185]. Employing a CBV perpendicular to the flow direction of the sample has not been implemented previously and in the following it will be described how this enables windowless microfluidic measuring platforms.

The microfluidic chip presented in this work has channels in the surface of the chip and a perpendicular windowless access hole through the bulk, as illustrated in Fig. 8.1(c) and 8.1(d).

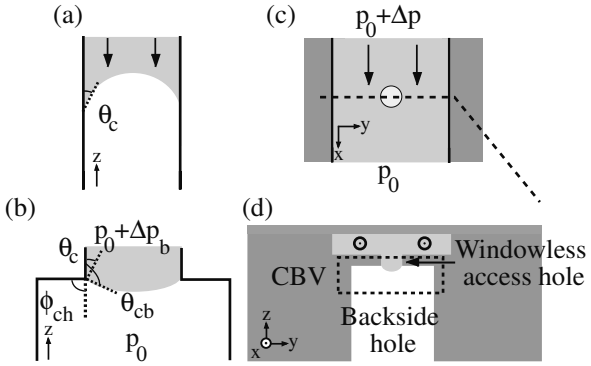

Figure 8.1: (a) Contact angle, θ_c, of a liquid propagating due to capillary forces in a hydrophilic channel. (b) A capillary burst valve at the bursting point, exposed to the burst pressure, Δp_b. (c+d) Schematic layout of the proposed windowless microfluidic platform as seen from above (c) and in cross-sectional view (d). It consists of a capillary burst valve placed in the middle of a flow channel. The dashed box in (d) refers to the situation depicted in (b).

8.3 Design and fabrication of the windowless microfluidic device

The microfluidic sample cell is illustrated in Fig. 8.2. It is designed with two inlet channels merging into a 1 cm long straight channel which terminates in two outlet channels identical to the inlets. All channels are 300 µm wide and 78 µm deep. In the middle of the straight channel the CBV is positioned. Figure 8.2(b) illustrates a top view of the device layout with a close-up of the CBV region in the inset. The large circle indicates the backside hole and the small circle indicates the windowless access hole. The diameter of the large backside hole of the CBV is kept constant at 200 µm but can be arbitrarily increased for better beam access. The diameter of the window itself is varied from 10 µm to 130 µm and the thickness of the window membrane is 25 µm in the substrate wafer and 40 µm in the lid wafer. For x-ray measurements the thickness of the window membrane should be minimized as much as possible as stagnant fluid in this volume will not be exchanged and may give rise to spurious background signals

as discussed in further detail later.

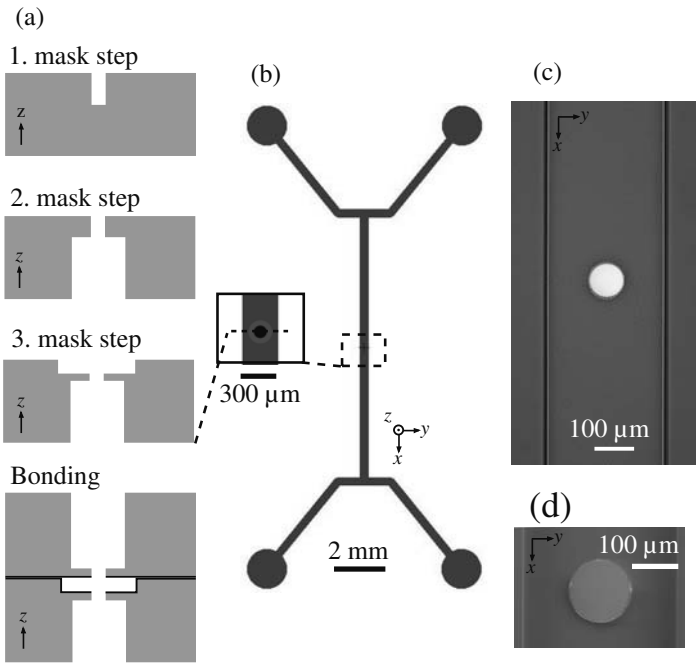

Figure 8.2: (a) Simplified outline of the fabrication process. Three mask steps are involved: 1) The windowless beam access, 2) the backside holes in the capillary burst valve (CBV) and 3) the micro-channel structure. Finally, fusion bonding is used to seal off the channel structures. (b) Chip layout with a close-up of the CBV region. The outer (shaded) circle corresponds to the backside hole and the inner (black) circle is the windowless X-ray beam access hole. (c) Microscope image with backside illumination, showing a finished device before bonding. The hole is 111 µm in diameter. (d) Scanning electron micrograph (SEM) image of the same device, centered on the CBV.

The microfluidic devices are fabricated in 500 µm thick, double polished, single crystalline (100) Si wafers. The fabrication consists of three masking steps. Each step employs a deep reactive ion etch (DRIE) utilizing the Bosch process [143], thereby transferring the structures anisotropically into the Si wafer. All masking steps are illustrated in Fig. 8.2(a). In each of the three steps, UV lithography is used to transfer the mask layout into an 10 µm thick UV sensitive resist layer (AZ4562 standard resist), on top of the Si wafer. The resist functions as an etch mask in the subsequent DRIE process optimized for deep etching (Etch: SF_6:230 sccm, O_2: 23 sccm, RF coil: 2800 W, RF platen: 19 W, Cycle time: 8 s. Passivation: C_4F_4:120 sccm, RF coil: 1000 W, RF platen: 0 W, Cycle time: 5 s.). The window and the backside hole are fabricated in the two first masking steps, and in the case of the substrate wafer, the channel structures are subsequently fabricated in a third masking step. Afterwards, a 110 nm silicon dioxide (SiO_2, black in Fig. 8.2(a)) layer is thermally grown (dry oxidation, 1100 °C, 50 min) on both the substrate and lid Si wafer to prepare the wafers for fusion bonding and to make the channels more hydrophilic. Finally, after removing the SiO_2 on the backside of the wafers and inside the CBV, fusion bonding [173] is

used to seal the channels in the structured Si substrate wafer either with a borofloat glass wafer or a Si wafer with backside- and access holes predefined according to the process described above. The transparent borofloat glass lid is used throughout the CBV characterization and the Si lid is used for the x-ray measurements. An example of a finished device before lid bonding is shown in Fig. 8.2(c) with a close-up of the CBV region in Fig. 8.2(d).

8.4 Characterization of the capillary burst valve

Characterization of the CBV was divided into three parts. The first part was an extensive investigation of the relation between the diameter of the windowless access hole and the burst pressure. A test-liquid consisting of 0.5 µm radius fluorescent labeled polystyrene spheres dispersed in deionized water at a 0.0001 % w/v solid concentration was used. The microspheres were used as marker particles to monitor the fluid flow velocity. No effect of the microspheres on the bursting pressure was observed at this concentration of microspheres, nor at the highest concentration tested, 0.1 % w/v. The second part of the characterization of the CBV-based devices involved testing the functionality with two samples, relevant for ultrafast time-resolved analysis of chemical and biological species in liquid solution. As chemical test sample an 8 mM of the highly photo-active platinum compound Tetrakis-µ-pyrophosphitodiplatinate(II) (PtPOP) in H_2O [120] was applied. The biological test sample was 2 mM, 5 mM and 10 mM of the well-studied protein Cytochrome-C [186] in a dedicated buffer (50 mM Hepes and 150 mM NaCl in deionized water). The third and final part of the characterization was a vacuum compatibility test to confirm that the device would work in environments below atmospheric pressure.

In all cases 500 µL of the sample was added to each of the two inlets and capillary forces dragged the sample into the device. Subsequently, an overpressure, supplied from a mini diaphragm vacuum pump (VP 86 with EU-plug, VWR) and controlled with a multi-turn needle valve (EW-06393-60, Cole Parmer), of 3 mbar was applied to the inlets. The established flow was allowed to continue for 15 minutes in order to secure stability of device and flow. The pressure at the inlets was then increased slowly from 3 mbar until the CBV was observed to burst. For each valve diameter, 5 to 9 chips from the same wafer were tested to provide sufficient statistics on the reproducibility of the results presented in Fig. 8.3. This figure shows the measured burst pressure as function of valve diameter along with the corresponding theoretical values calculated from Eqn. 8.1. After the initial burst events reported in Fig. 8.3, the burst pressure was observed to depend critically on cleaning, but was generally lower than the initial value. This lowering of burst pressure is assigned to the presence of microspheres and other solid contaminants at the transition between the narrow and the wide part of the CBV.

The surface tension in equation 8.1 is set to the value of water on Si at 20 °C, 72.9 mJ/m^2. The contact angle, $\theta_{cb} = \theta_c + \phi_{cb}$, was observed to depend on hole diameter, due to the DRIE process of the backside hole. θ_c was measured (Krüss DSA100) to be 40.5 ° with a standard deviation of 5.7 °. The corresponding uncertainty in predicted burst pressure is represented in Fig. 8.3 by the dashed lines. ϕ_{cb} was determined by SEM investigations of split CBVs was determined to depend directly on the hole diameter and to range from 70 ° for the largest access holes to 90 ° for the smallest

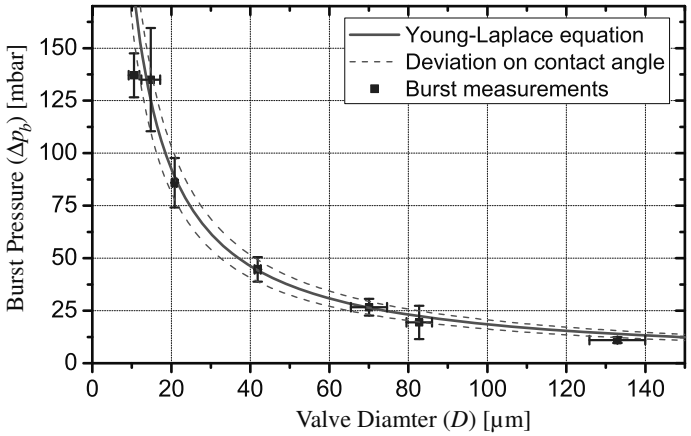

Figure 8.3: Measured (blue data points) and predicted values (red lines) of the bursting pressure as a function of the diameter of the windowless access hole in the capillary burst valve. The length of the error bars on the data points equal 2 standard deviations, the dashed lines denote the upper and lower predicted limits, taking fabrication imperfections into account (see text for details).

holes. Altogether, θ_{cb} ranges from 112 ° to 132 ° in the devices. The burst pressures predicted through Eqn. 8.1, using these values are indicated by the solid line in Fig. 8.3.

As seen in Fig. 8.3, the bursting pressure as a function of valve diameter is well described by Eqn. 8.1. From the characterization measurements on the CBV devices, the average flow velocity in the channel was observed to depend linearly on the pressure difference between inlet and outlet as expected for a Poiseuille flow [129]. The increase in average velocity per mbar pressure increase was found to be 2 mm/(s mbar). The maximum average velocity thus ranged from 44 mm/s for the 130 µm access holes to 540 mm/s for the 10 µm access holes corresponding to a refresh rate of the measuring volume of 0.3 kHz and 54 kHz respectively. It should be noted that the angle of the air-liquid interface of the CBV is strongly dependent on the driving pressure, going from convex to concave with increasing pressure. For applications where refraction effects are of importance, the overpressure can thus be chosen to produce a flat meniscus interface.

In the compatibility test with PtPOP and Cytochrome-C the CBV did not deviate from the tests with 0.0001 % w/v polystyrene microspheres in water presented in Fig. 8.3. These tests were carried out in an identical fashion, but additionally the 500 µl sample from each inlet was collected after passing the chip and from microscope inspections it was verified that it was not absorbed on the inner surfaces of the microfluidic channels. Examples of 2 mM, 5 mM and 10 mM Cytochrome-C samples in the chip is shown in Fig. 8.4(b), 8.4(c) and 8.4(d) respectively.

Basic vacuum functionality was confirmed, using a purpose-built vacuum chamber with liquid connections to the chip. The chip was tested down to a chamber pressure

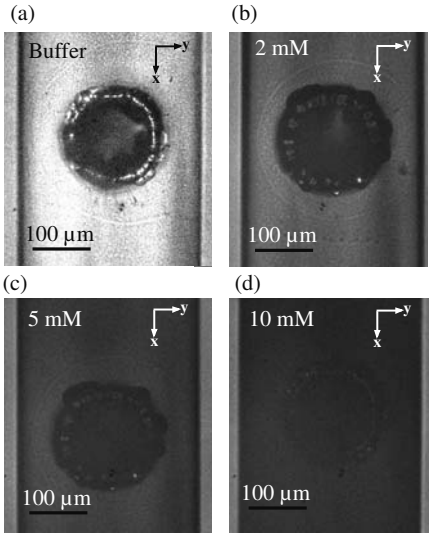

Figure 8.4: Microscope images of the microchannel at the capillary burst valve with three different concentrations of the protein Cytochrome-C: (b) 2 mM, (c) 5 mM and (d) 10 mM compared with only buffer (a). The buffer in these measurements is 50 mM NaCl in deionized water. The intensity scale of the images are equalized, so the darkness in the channel indicates the concentration, with dark corresponding to high concentration. It is evident from the images that there is no build-up of proteins in the channel segments.

of 100 mbar with deionized water as the test liquid. The results were similar to those presented in Fig. 8.3.

8.5 X-ray measurements

To test the proposed sample handling system under realistic operating conditions, a CBV chip with Si lid was mounted at the time-resolved beamline ID09b [187] at the ESRF synchrotron facility in Grenoble using a purpose-built sample chuck with incorporated channels for sample supply to the chip. The measurements were carried out together with Kristoffer Halrup, Martin Meedom Nielsen and other experienced x-ray users from CMM. After preparing the system with a sample solution (water) and connecting it to the flow control system, the access hole on the chip was manually aligned to the incoming laser- and x-ray beams using a microscope. The position was subsequently refined using a point detector situated behind (downstream) the chip+holder.

Figure 8.5 shows the scattering pattern acquired on an area detector (Frelon) placed 10 cm downstream from the laser/x-ray overlap point positioned in the middle of the flow channel. Also shown in this figure are gray rings denoting values of the scattering angle 2θ. Due to the narrow geometry chosen for the backside hole in the CBV, part of the Si substrate will shadow some parts of the detector. The black, bold circle denote the point where shadowing due to absorption in Si exceeds 5 % at 18 keV, assuming scattering from a point in the center of the channel. It is observed that only the part of the scattering pattern extending up to $2\theta = 12\,^\circ$ ($Q = 1.8\,\text{Å}^{-1}$, $Q = \frac{4\pi}{\lambda}\sin\theta$

($\lambda \sim 0.7\,\text{Å}$)) is completely unperturbed by shadowing effects with the present chip geometry. The driving pressure was kept at 3 mbar, corresponding to a flow speed of 6 mm/s (refresh rate = 41 Hz). This corresponds to a sample consumption rate of 0.5 mL/h, in good correspondence with observations during the experiments.

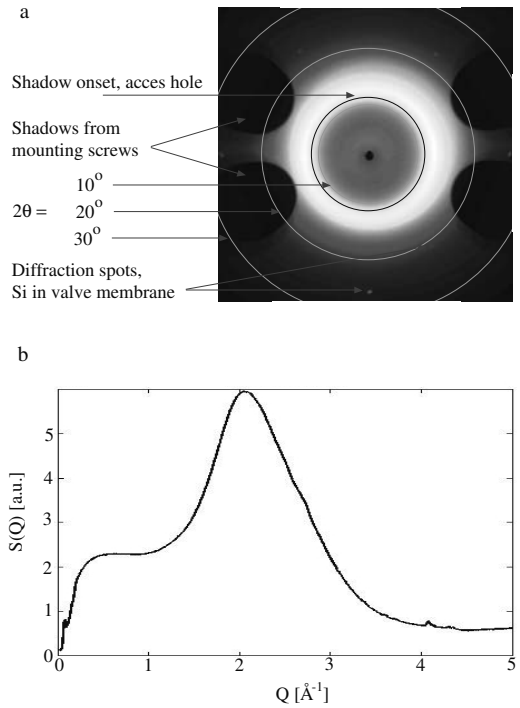

Figure 8.5: (a) Scattering pattern from a de-ionized water sample in a sample chip with a 110 µm capillary burst valve. The scattering pattern was acquired over a 1 s period, corresponding to 986 individual photon bunches from the synchrotron, each containing $\sim 10^9$ photons. The gray circles in the figure denotes values of the scattering vector/scattering angles and the black circle indicates the onset of shadowing effects for a scatterer situated in the middle of the flow channel. (b) Azimuthal integration of the detector-image in (a), the water peak centered at $Q = 2\,\text{Å}^{-1}$ is very evident.

Attempts at acquiring a time-resolved signal with a solution of TlPtPOP [188] were not conclusive, as irradiation of the stagnant volume caused significant precipitation of Pt crystallites as well as strong perturbations of the scattering signals due to local heating. However, transient heating of the precipitated crystallites was observed on the sub-ns time scale, confirming that spatial overlap between laser and x-ray was not lost during the experiment. The observed issues relating to the stagnant volume give rise to considerations regarding chip design and the possibility of introducing thin windows e.g. of silicon nitride. However, the presence of windows may lead to gradual and irreversible irradiation-induced build-up of contaminants on the window surface, whereas any contaminants in the stagnant volume will eventually be removed through diffusion. This is especially so, if the stagnant volume is minimized by decreasing the thickness of the open access window. Also, at sufficiently high x-ray intensities, window

damage will be inevitable, which is an important cosideration for XFEL applications. With a CBV, we achieve a self-healing liquid membrane, which is not permanently damaged and where x-ray diffraction characteristics do not change over time.

8.6 Outlook

As touched upon above, modifications of the existing device layout is necessary before it become fully functional for time-resolved high intensity x-ray measurements. In-situ experiments at ID09b (ESRF) demonstrated that the stagnant volume associated with the CBV region was strongly detrimental to chip performance. Also, significant shadowing effects were observed, complicating data analysis for scattering angles exceeding 2θ=12°. These issues could be addressed by replacing the DRIE process with an anisotropic kalium hydroxide (KOH) etch, giving atomically sharp edges with no associated stagnant volume as well as a 34° slope of the access hole, allowing unimpeded collection of scattered x-rays up to 2θ=30°. Initial measurements on KOH-etched prototype devices confirmed the basic feasibility of this approach, but at the cost of considerable lowered burst pressure, suggesting a combination of KOH and DRIE etch for a final design. It was also confirmed in these measurements that the stagnant volume is required to get burst pressures as expected from Eqn. 8.1. In future measurements the minimum necessary stagnant volume should be investigated. By introduction of an etch-stop layer, before the etch of the backside hole, sub-micrometer thick opening holes can be achieved.

A second improvement of the existing design is a tapered channel at the windowless access hole as illustrated in Fig. 8.6. In initial measurements, the fluid velocity, as well as the refreshment rate, were doubled compared to the previous design. The tapered region can be optimized even further to achieve larger flow velocities. An additional advantage of this design is that all sample will pass the measuring area at the windowless access hole.

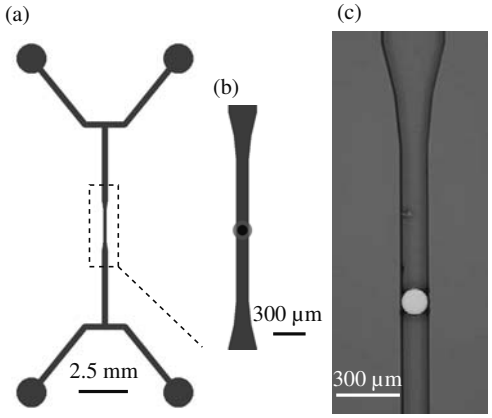

Figure 8.6: Device with tapered channel design at the windowless access hole. (a)+(b) Design drawings of the device. The large circle in (b) indicates the backside hole whereas the the small circle is the front hole. (a) Microscope image of the fabricated device with backside illumination.

An attractive feature of the proposed microfluidic system is the very low sample consumption, mL/h, and straightforward integration of existing LOC technologies, such as separation by PFF and incorporation of optical diagnostics [120]. In future work such an addition should be incorporated in a total LOC platform for time-resolved high intensity x-ray measurements.

8.7 Summary

In the preceding sections, a microfluidic system with an out-of-plane capillary burst valve enabling windowless access to a micro channel has been demonstrated. The functionality of the out-of-plane CBV has been demonstrated up to driving pressures of 280 mbar corresponding to a burst pressure of 140 mbar (the CBV is placed in the middle of the microfluidic network), and the bursting pressure has been shown to be in good correspondence with the Young-Laplace equation for a channel with circular cross-section.

Observing flow velocities of suspended fluorescent microspheres, the maximum sample replenishment rate for the system described in this chapter ranges from 0.3 kHz (130 µm access hole) to 54 kHz (10 µm access hole), and can be doubled in a tapered channel design. Beside suspended microspheres, the device functionality was also demonstrated with protein samples, a photoactive titanium compound and under vacuum conditions in the surrounding of the chip. Finally, synchrotron beamline feasibility and time-resolved x-ray measurements were demonstrated, and an improved device layout was suggested.

Chapter 9

Conclusions and outlook

In this PhD project the three main aspects of lab-on-a-chip (LOC) development — 1) fabrication, 2) sample treatment and transport and 3) detection — are studied using a size separation microfluidic technique called pinched flow fractionation (PFF). Most LOC devices aim for small, compact and easy-to-use systems for fast analysis to enable point-of-care (POC) usage. These subjects are therefore the evaluation criteria of the study. In addition, another part of this thesis involves the development of a windowless microfluidic platform for time-resolved high intensity x-ray imaging. Here the success criteria do not involve POC applications, but rather other advantages of LOC such as low sample consumption, well controlled sample volume and fast flow velocities.

Pinched flow fractionation has been theoretically studied via fluidic models that do not include particles. A numerical model developed throughout this thesis proved to give an improved description of the separation compared to previous analytical models from literature. Inclusion of particles increase the complexity of a theoretical description significantly and is beyond the scope of the thesis. However, a qualitative discussion based on published articles was included. Pinched flow fractionation devices, fabricated by nanoimprint lithography in a Topas®-based cyclo olefin copolymer (mr-I T85), was experimentally characterized by separation of up to 8 different microsphere sizes ranging from 0.26 µm to 2.5 µm. Two reproducible separation regimes were observed depending on the solid concentration and number of different particle sizes. The separation resolution was measured for a sample with a standard deviation of 5 % in size to be down to 100 nm. In all PFF measurements the inlet channels are fed with sample and buffer using syringe pumps, and tight fluid connections are ensured by clamping of the device to a chuck by screws. This measuring setup is not user-friendly, and even for an experienced user is time consuming. A chip design enabling a more simple and user friendly measurement setup in regards to flow control and device fixation has been presented. Here, the hydraulic resistance in the inlet channels of PFF is designed such that particles are pinched and separated by applying vacuum to the outlets.

One of the major remaining bottlenecks of LOC before a commercial breakthrough, is development of cheap and high volume fabrication. In order to address this issue a technique relying on roll-to-roll methods was developed. Roll-to-roll printing in macro-scale has already proven its extreme high volume capability through newspaper printing and holographic printing on money bills. In addition, roll-to-roll methods are continuous, so channel structures can be imprinted and sealed in the same machine in

a very fast and cheap process manner. In a three-step roll-to-roll production line — material coating (reverse gravure), device structure definition (thermal imprinting) and sealing (lamination) — a fabrication volume of 360 functional PFF devices per hour in cellulose acetate at a unit cost of 0.5 Euro was achieved. Through optimization of the fabrication process it was found that the imprint temperature must be as high as possible to avoid recovery effects in the polymer, but not equal to or higher than the glass transition temperature of the substrate material to avoid film stretching. The optimal temperature was found to be 115 °C in cellulose acetate, which has a glass transition temperature of 120 °C. The functionality of the devices was demonstrated by separation of fluorescent polystyrene microspheres. An example with 0.5 µm and 1.5 µm microspheres was shown. In this study three different machines were used, one for each of the rtr steps. However, all the steps can, with slight machine modifications, be integrated in the custom designed roll-to-roll nanoimprinting machine used for imprinting. In industrial productions this will be a necessary improvement and is an obvious extension of the work presented here.

The separation in PFF has been enhanced by a small channel modification in the broadening segment, still compatible with the roll-to-roll fabrication. Enhancement in the separation of up to 70 % and in the resolution up to 25 % was measured for sample with a standard deviation in size of 5 %. The EPFF devices characterized throughout the study were design for separation of the microspheres with radii up to 4.5 µm and not up to 2.5 µm, which was the sphere radii used in this work. If the device was optimized for these radii, a separation enhancement factor up to 2.6, corresponding to a 260 % enhancement, would be expected.

In most microfluidic systems, especially in biological and chemical analysis, very expensive and bulky readout systems are used, in conflict with the basic idea of LOC in POC diagnosis. A detection unit, based on an optofluidic microscope, has been integrated in the PFF layout, to realize cheap and compact detection. This setup enable three dimensional optical detection of separated polystyrene microspheres using a microscope as relay. The resolution of the detection in the microchannel was $\leq$0.92 µm in width and 1.4 µm in height. The optofluidic microscope was also used for particle image velocimetry at a resolution of 4 % of the measured velocity, which ranged up to 2 mm/s. The resolution in space and velocity was limited by the geometric setup of the optofluidic microscope, the objective used for light collection and the data converting methods. For a more compact and portable system, the OFM integrated PFF device should either be combined with a small purpose-built measuring setup including a light source, a microscope objective and a CCD detector, or be fabricated directly on top of the a lens array and a CCD detector. The principle of the second solution has already been demonstrated [117].

A microsphere-based array for genotyping single nucleotide polymorphisms using the PFF setup has been demonstrated. Two different streptavidin-coated microsphere sizes were funtionalized with biotin-labeled oligonucleotides for detection of a mutant- or wild-type DNA sequence in the Hemoglobin beta (HBB) gene. Fluorescent labeled amplified RNA, synthesized using human DNA samples from individuals with point mutations in the HBB gene were hybridized to the functionalized microspheres. The microspheres were separated in PFF, and by fluorescent detection of their position in the broadening segment the patients were diagnosed by PFF.

To pursue one of the presently "hot" topics in LOC, namely single cell proteomics, the basic layout of PFF was down-scaled to the nanometer regime to enable single protein separation. In this study the first steps towards protein separation in a nano-scale PFF (nanoPFF) device was demonstrated, including surface functionalization to prevent protein immobilization. A finite element model (FEM) in COMSOL Multiphysics was used to back-track imaged distributions of nanospheres with a radius of 22 nm and 50 nm in the broadening segment to a distribution in the pinch segment, where the spatial resolution is below the detection limit. This is a possible tool for future studies of the physics for particle behavior within nano-scale channels. The presented nanoPFF device was designed with symmetric inlet channels, with a lower hydraulic resistance compared to the total of the pinch segment, broadening segment and outlet channels. A large flowrate-ratio in the two inlets is therefore not possible without a back-flow in one of the inlets. A layout with asymmetric inlet channels was proposed to avoid this issue, which is expected to enable better separation. A second essential improvement towards better separation is a measurement setup that can withstand up to 40 bar. Diffusion, which constitutes a significant limitation to the separation, could then be lowered considerably.

To sum up, all development aspects of LOC have been addressed using PFF as a model system. The solutions in regards to fabrication, separation and detection were chosen to be consistent, realizing a POC device that is cheap, compact and easy-to-use. In addition, an application is demonstrated through SNP genotyping and the scalability for separation of single nanometer-size particles was also demonstrated. In the present study roll-to-roll fabrication, vacuum driven user-friendly devices and three dimensional detection by an OFM have all been demonstrated in combination with PFF. These techniques are chosen to be consistent, but have not been demonstrated in combination. An obvious continuation of the work would therefore be a combined PFF device fabricated by roll-to-roll methods with a channel design enabling vacuum driven separation and detection by an OFM. In this thesis, spherical rigid particles have been separated. However, in literature PFF has also been demonstrated for non-spherical red blood cells and soft emulsion droplets, proving a wide range of applications. As such, the combined PFF device as described above would be a promising candidate for LOC applications involving size separation. This study will hopefully inspire future LOC development to include considerations on all of the three above-mentioned development aspects in a coherent fashion. However, while it is true that such studies are time consuming and expensive, when they gain credibility in the academic world, it is the authors expectation that LOC systems will become economically viable. As a result point-of-care analysis devices will be realized.

Finally, a windowless microfluidic platform based on capillary burst valves (CBVs) for time-resolved high intensity x-ray measurements was developed. This platform meets existing, challenges of current measurement techniques such as unstable measuring volume, curved interfaces and intermediate layers in the x-ray beam path. Capillary burst valves with circular x-ray access holes ranging from 10 µm to 130 µm in diameter, D, was characterized to withstand a pressure difference from 12 mbar ($D = 130\,\mu m$) to 140 mbar ($D = 10\,\mu m$), corresponding to a sample refresh rate in the microfluidic channel of 0.3 kHz and 54 kHz respectively. The refreshment rate can be increased considerable by channel modifications around the access hole. The tested access hole diameters are relevant in most existing and soon coming time-resolved x-ray facilities, and the refreshment rate is usable in most biological and some chemical studies. The

functionality of the platform was demonstrated with microspheres suspensions, protein samples and a photoactive platinum compound — relevant in a catalysis process in the car industry. Additionally, the system was tested successfully under realistic operation conditions at the time-resolved beamline ID09b at the ESRF synchrotron facility in Grenoble, and a sub-nanosecond time resolution was confirmed.

The microfluidic platform for x-ray studies has already gained much attention in the time-resolved x-ray community. Still, the platform has to be further optimized before it is ready for state-of-the-art measurements. The largest challenge is to minimize the stagnant volume present at the open windows. In the present device layout this volume is rather large and sample tends to accumulate here, which gives rise to a high noise level. By a reduction of the volume, diffusion is expected to ensure a low sample concentration in the volume. In addition, the microfluidic windowless platform enables integration of a wide range of LOC components e.g. lasers and waveguides for optical characterization of the x-ray exposed sample, or PFF for separation prior to the exposure. After such improvements the platform is expected to have a large impact, especially in studies with rare sample. Time-resolved high intensity x-ray studies enable an insight in the dynamics of the smallest building blocks of nature, e.g. in proteins, DNA or molecules, and is expected to add significant understanding to the physics and chemistry of these in the comming decades.

Bibliography

[1] H.M. Widmer. Trends in industrial analytical chemistry. *Trends in Analytical Chemistry*, 2(1):R8–R10, 1983.

[2] A. Manz, N. Graber, and H.M. Widmer. Minituarized Total Chemical Analysis Systems: a Novel Concept for Chemical Sensing. *Sensors and Actuators*, B1:244–248, 1990.

[3] A. Manz, J. C. Fettinger, E. Verpoorte, L. Lüdi, H.M. Widmer, and D.J. Harrison. Micromachining of moncrystaline silicon and glass for chemical analysis systems - a look into next century's technology or just a fasionable craze. *Trends in Analytical Chemistry*, 10(5):144–149, 1991.

[4] Limunex corporation. http://www.luminexcorp.com. 2 November 2009.

[5] Interuniversity Microelectronics Centre. http://www.medicalnewstoday.com/articles/166835.php. *Medical News Today*, 2 November 2009.

[6] A. Hatch, A.H. Kamholz, K.R. Hawkins, M.S. Munson, E.A. Schilling, B.H. Weigl, and P. Yager. A rapid diffusion immunoassay in a T-sensor. *Nature Biotechnology*, 19:461–465, 2001.

[7] P. Abgrall and A.-M. Gué. Lab-on-a-chip technologies: making a microfluidic network and coupling it into a complete microsystem - a review. *Journal of Micromechanics and Microengineering*, 17:R15–R49, 2007.

[8] H. Becker and C. Gärtner. Polymer microfabrication technologies for microfluidic systems. *Analytical and Bioanalytical Chemistry*, 309:89–111, 2008.

[9] M. Heckele and W. K. Schomburg. Review on micro molding of thermoplastic polymers. *Journal of Micromechanics and Microengineering*, 14:R1–R14, 2004.

[10] R.-D. Chien. Micromolding of biochip devices designed with microchannels. *Sensors and Actuators A*, 128:238–247, 2006.

[11] D. A. Mair, E. Geiger, A. P. Pisano, J. M. J. Fréchet, and F. Svec. Injection molded microfluidic chips featuring integrated interconnects. *Lab on a Chip*, 6:1346–1354, 2006.

[12] T. Katoh, R. Tokuno, Y. Zhang, M. Abe, K. Akita, and M. Akamatsu. Micro injection molding for mass prodution using Liga mold inserts. *Microsystem Technologies*, 14:1507–1514, 2008.

[13] D. Macintyre and S. Thoms. The Fabrication of High Resolution Features By Mould Injection. *Microelectronic Engineering*, 41:211–214, 1998.

[14] H. Pravnov, H. K. Rasmussen, N. B. Larsen, and N. Gadegaard. On the Injection Molding of Nanostructured Polymer Surfaces. *Polymer Engineering and Science*, pages 160–171, 2006.

[15] U. M. Attia, S. Marson, and J. R. Alcock. Micro-injection moulding of polymer microfluidic devices. *Microfluid Nanofluid*, 7:1–28, 2009.

[16] H. Becker and U. Heim. Hot embossing as a mothod for fabrication of polymer high aspect ratio structures. *Sensors and Actuators*, 83:130–135, 2000.

[17] H. Schift, C. David, M. Gabriel, J. Gobrecht, L. J. Heyderman, W. Kaiser, S. Köppel, and L. Scandella. Nanoreplication in polymers using hot embossing and injection molding. *Micreelectronic Engineering*, 53:171–174, 2000.

[18] J. Giboz, T. Copponex, and P. Méle. Microinjection molding of thermoplastic polymers: a review. *Journal of Micromechanics and Microengineering*, 17:R96–R109, 2007.

[19] M. D. Austin, H. Ge, W. Wu, M. Li, Z. Yu, D. Wasserman, S. A. Lyon, and Y. Chou. Fabrication of 5 nm linewidth and 14 nm pitch features by nanoimprint lithography. *Applied Physics Letters*, 84(26):5299–5301, 2004.

[20] T. E. Kimerling, W. Liu, B. H. Kim, and D. Yao. Rapid hot embossing of polymer microfeatures. *Microsystem Technologies*, 12:730–735, 2006.

[21] M. Madou, J. Zoval, G. Y. Jia, H. Kido, J. Kim, and N. Kim. Lab on a CD. *Annual Review of Biomedical Engineering*, 8:601–628, 2006.

[22] J. C. McDonald, D. C. Duffy, D. T. Chiu, H. Wu, O. J. A. Schueller, and G. M. Whitesides. Fabrication of microfluidic systems in poly(dimethylsiloxane). *Electrophoresis*, 21:27–40, 2000.

[23] H. Feng, A. Gaur, S. Yugang, M. Word, J. Niu, I. Adesida, M. Shim, A. Shim, and J. A. Rogers. Processing Dependent Behavior of Soft Imprint Lithography on the 110 nm Scale. *IEEE Transactions on Nanotechnology*, 5(3):301–308, 2006.

[24] P. R. Cusachs, F. Rico, E. Martinez, J. Toset, R. Farré, and D. Navajas. Stability of Microfabricated High Aspect Ratio Structures in Poly(dimethylsiloxane). *Langmuir*, 21(12):5542–5548, 2005.

[25] S. Giselbrecht, T. Gietzelt, E. Gottwald, C. Trautmann, R. Trukenmüller, K. F. Weibezhan, and A. Welle. 3D tissue culture substrates produced by microthermoforming of pre-processed polymer films. *Biomedical Microdevices*, 8:191–199, 2006.

[26] R. Truckenmüller, S. Giselbrecht, C. van Bitterswijk, N. Dambrowsky, E. Gottwald, T. Mappes, A. Rolletschek, V. Saile, C. Trautmann, K.-F. Weiberzahn, and A. Welle. Flexible fluidic microchip based on thermoformed and locally modified thin polymer films. *Lab on a Chip*, 8:1570–1579, 2008.

[27] C. Harrison, J. T. Cabral, C. M. Stafford, A. Karim, and E. J. Amis. A rapid prototyping technique for the fabrication of solvent-resistant structures. *Journal of Micromechanics and Microengineering*, 14:153–158, 2004.

[28] S. Metz, S. Jiguet, A. Bertsch, and Ph. Renaud. Polyimide and SU-8 microfluidic devices manufactured by heat-depolymerizable sacrificial material technique. *Lab on a Chip*, 4:114–120, 2004.

[29] H. Lorentz, M. Despont, N. Fahrni, J. Brugger, P. Vettiger, and P. Renaud. High-aspect-ratio, ultrathick, negative-tone near-UV photoresist and its applications for MEMS. *Sensors and actuators A*, 64:33–39, 1998.

[30] J. Kim and X. Xu. Excimer laser fabrication of polymer microfluidic devices. *Journal of Laser Applications*, 15(4):255–260, 2003.

[31] H. Klank, J. P. Kutter, and O. Geschke. CO_2laser micromachining and back-end processing for rapid production of PMMA-based microfluidic systems. *Lab on a Chip*, 2:242–246, 2002.

[32] Inc Clark MXR. http://www.cmxr.com/industrial/handbook/. October 29 2009.

[33] V. N. Tokarev, J. Lopez, S. Lazare, and F. Weisbuch. High-aspect-ratio micro-drilling of polymers with UV laser ablation: experiment with analytical model. *Applied Physics A*, 76:385–396, 2003.

[34] J. D. Plummer, M. D. Deal, and P. B. Griffin. *Silicon VLSI Technology - Fundamental, Practice and Modelling*. Prentice Hall, Inc, 2000.

[35] T. Mäkelä, T. Haataninen, P. Majander, and J. Ahopelto. Continuous roll-to-roll nanoimprinting of inherently conducting polyaniline. *Microelectronic Engineering*, 84:877–879, 2007.

[36] S. H. Ahn and L. J. Guo. High-Speed Roll-to-Roll Nanoimprint Lithography on Flexible Plastic Substrates. *Advanched Materials*, 9999:1–6, 2008.

[37] N. Ishizawa, K. Idei, T. Kimura, D. Noda, and T. Hattori. Resin micromachining by roller hot embossing. *Microsystem Technologies*, 14:1381–1388, 2008.

[38] S. H. Ng and Z. F. Wang. Hot roller embossing for microfluidics: process and challenges. *Microsystem Technologies*, 15:1149–1156, 2009.

[39] D. J. Laser and J. G. Santiago. A review of micropumps. *Journal of Micromechanics and Microengineering*, 14:R35–R64, 2004.

[40] P. Woias. Micropumps - past, present and future prospects. *Sensors and Actuators B*, 105:28–38, 2005.

[41] K. W. Oh and C. H. Ahn. A review of microvalves. *Journal of Micromechanics and Microengineering*, 16:R13–R39, 2006.

[42] N.-T. Ngyuen and Z. Wu. Mixromixers - a review. *Journal of Micromechanics and Microengineering*, 15:R1–R16, 2005.

[43] E. A. Mansur, Y. Mingxing, W. Yundong, and D. Youynan. A state-of-the-art review in mixrofluidix mixers. *Chinese Journal of Chemical Engineering*, 16(4):503–518, 2008.

[44] S. Haeberle and Z. Roland. Microfluidic platforms for lab-on-a-chip applications. *Lab on a Chip*, 7:1094–1110, 2007.

[45] C.-T. Lin, M.-T. Kao, K. Kurabayashi, and E. Meyhofer. Self-Containing, Biomolecular Motor-Driven Protein Sorting and Concentrating in an Ultrasensitive Microfluidic Chip. *Nanoletters*, 8(4):1041–1046, 2008.

[46] N. Pamme. Continous flow separations in microfluidic devices. *Lab on a Chip*, 7:1644–1659, 2007.

[47] J. C. Giddings. Field-flow fractionation: analysis of macromolecular, colloidal, and particulate materials. *Science*, 260:1456–1465, 1993.

[48] S. Oh, D. Kang, S.-M. Ahn, R. J. Simpson, B.-H. Lee, and M. H. Moon. Minituarized asymmetrical flow field-flow fractionation: Application to biological vesicles. *Journal of Separation Science*, 30:1082–1087, 2007.

[49] S. T. Kim, D. Y. Kang, S. Lee, W.-S. Kim, J. T. Lee, H. S. Cho, and S. H. Kim. Separation and Quantitation of Silver Nanoparticles using Sedimentation Field-Flow Fractionation. *Journal of Liquid Chromatography and Related Technologies*, 30:2533–2544, 2007.

[50] M. T. Blom, E. Chmela, R. E. Oosterbroek, R. Tijssen, and A. van den Berg. On-chip hydrodynamic chromatography separation and detection of nanoparticles and biomolecules. *Analytical Chemistry*, 75(24):6761–6768, 2005.

[51] H. Ghourchian and H. Elyasvandi. Capacitively induced pulsed-field gel elctrophoresis: a novel method for dna separation. *Medical Engineering and Physics*, 27:723–727, 2005.

[52] Y. Okamoto, F. Kitagawa, and K. Otsuka. Separation of cationic polymer particles and charaterization af avidin-immobilized particles by capillary electrophoresis. *Electrophoresis*, 27:1031–1040, 2006.

[53] R. T. Turgeon and T. B. Browser. Micro free-flow electrophoresis: theory and applications. *Analytical and Bioanalytical Chemistry*, 394:187–198, 2009.

[54] H. Watarai, M. Suwa, and Y. Iiguni. Magnetophoresis and electromagnetophoresis of microparticles in liquids. *Analytical and Bioanalytical Chemistry*, 378:1693–1699, 2004.

[55] B. Cetin, Y. Kang, Z. Wu, and D. Li. Continuous particle separation by size via AC-dielectrophoresis using a lab-on-a-chip device with 3-D electrodes. *Electrophoresis*, 30:766–772, 2009.

[56] F. Petersson, L. Åberg, A.-M. Swärd-Nilsson, and T. Laurell. Free flow acoustophoresis: microfluidic-based mode of particle and call separation. *Analytical Chemistry*, 79:5117–5123, 2007.

[57] M. P. MacDonald, G. C. Spalding, and K. Dholakia. Microfluidic sorting in an optical lattice. *Letters to Nature*, 426:421–424, 2003.

[58] M. Yamada and M. Seki. Hydrodynamic filtration for on-chip particle concentration and classification utilizing microfluidics. *Lab on a Chip*, 5:1233–1239, 2005.

[59] R. Aoki, M. Yamada, M. Yasuda, and M. Seki. In-channel focusing of flowing microparticles utilizing hydrodynamic filtration. *Microfluidics and Nanofluidics*, 6:571–576, 2009.

[60] A. A. S. Bhagat, S. S. Kuntaegowdanahalli, and I. Papautsky. Continuous particle separation in spiral microchannels using dean flow and differential migration. *Lab on a chip*, 8:1906–1914, 2008.

[61] S. S. Kuntaegowdanahalli, A. A. S. Bhagat, G. Kumar, and I. Papautsky. Inertial microfluidics for continuous particle separation in spiral microchannels. *Lab on a Chip*, 9:2973–2980, 2009.

[62] C.-H. Lin, C.-Y. Lee, C.-H. Tsai, and L.-M. Fu. Novel continuous particle sorting in microfluidic chip utilizing cascade squeeze effect. *Microfluidics and Nanofluidics*, 7:499–508, 2009.

[63] J. Fu, R. B. Schoch, A. L. Stevens, S. R. Tannenbaum, and J. Han. A patterned anisotropic nanofluidic sieving structure for continuous-flow separation of DNA and proteins. *Nature*, 2:121–128, 2007.

[64] V. VanDelinder and A. Groisman. Separation of Plasma from Whole Human Blood in a Continuous Cross-Flow in a Molded Microfluidic Device. *Analytical Chemistry*, 78:3765–3771, 2006.

[65] V. VanDelinder and A. Groisman. Perfusion in Microfluidic Cross-Flow: Separation of White Blood Cells from Whole Blood and Exchange of Medium in Contionuous Flow. *Analytical Chemistry*, 79:2023–2030, 2007.

[66] L. R. Huang, E. C. Cox, R. H. Austin, and J. C. Sturm. Continuous Particle Separation Through Deterministic Lateral Displacement. *Science*, 304:987–990, 2004.

[67] D. W. Inglis, J. A. Davis, R. H. Austin, and J. C. Sturm. Critical particle size for fractionation by deterministic lateral displacement. *Lab on a Chip*, 6:655–658, 2006.

[68] J. Beech and J. Tegenfeldt. Tunable separation in elastomeric microfluidic devices. *Lab on a Chip*, 8:657–659, 2008.

[69] D. W. Inglis, K. J. Morton, J. A. Davis, T. J. Zieziulewicz, D. A. Lawrence, R. H. Austin, and J. C. Sturm. Microfluidic devices for label-free measurements of platelet activation. *Lab on a Chip*, 8:925–931, 2008.

[70] Beech J. P., P. Jönsson, and J. O. Tegenfeldt. Tipping the balance of deterministic lateral displacement devices using dielectrophoresis. *Lab on a Chip*, 9:2698–2706, 2009.

[71] D. W. Inglis. Efficient microfluidic particle separation arrays. *Applied Physics Letters*, 94:013510, 2009.

[72] S. Yang, A. Ündar, and J. D. Zahn. A microfluidic device for continuous, real time blood plasme separation. *Lab on a Chip*, 6:871–880, 2006.

[73] R. D. Jäggi, R. Sandoz, and C. S. Effenhauser. Microfluidic depletion of red blood cells from whole blood in high aspect ratio microchannels. *Microfluidics and Nanofluidics*, 3:47–53, 2007.

[74] T. A. J. Duke and R. H. Austin. Microfabricated Sieve for the Continuous Sorting of Macromolecules. *Physics Review Letters*, 80(7):1552–1555, 1998.

[75] J. S. Bader, R. W. Hammond, S. A. Henck, M. W. Deem, G. A. McDermott, J. M. Bustillo, J. W. Simpson, G. T. Mulhern, and J. M. Rothberg. DNA transport by a micromachined Brownian ratchet device. *Proceedings of the National Academy of Science*, 96(23):13165–13169, 1999.

[76] L. R. Huang, P. Silberzan, J. O. Tegenfeldt, E. C. Cox, J. C. Sturm, R. H. Austin, and H. Craighead. Role of Molecular Size in Ratchet Fractionation. *Physics Review Letters*, 89(17):178301, 2002.

[77] L. R. Huang, E. C. Cox, R. H. Austin, and J. C. Sturm. Tilted Brownian Ratchet for DNA Analysis. *Analytical Chemistry*, 75(24):6963–6967, 2003.

[78] S. Choi, S. Song, C. Choi, and J.-K. Park. Continous blood cell separation by hydrophoretic filtration. *Lab on a Chip*, 7:1532–1538, 2007.

[79] S. Choi and J.-K. Park. Continuous hydrodynamic separation and sizing of microparticles using slanted obstacles in a microchannel. *Lab on a Chip*, 7:890–897, 2007.

[80] S. Choi, S. Song, C. Choi, and J.-K. Park. Sheatless Focussing of Microbeads and Blood Cells based on Hydrophoresis. *Small*, 4(5):634–641, 2008.

[81] S. Choi, S. Song, C. Choi, and J.-K. Park. Microfluidic Self-Sorting of Mammalian Cells to Achieve Cell Cycle Synchrony by hydrophoresis. *Analytical Chemistry*, 81(5):1964–1968, 2009.

[82] S. Choi, S. Song, C. Choi, and J.-K. Park. Hydrophoretic Sorting of Micrometer and Submicrometer Particles using Anisotropic Microfluidic Obstacles. *Analytical Chemistry*, 81(5):50–55, 2009.

[83] P. Sethu, A. Sin, and M. Toner. Microfluidic diffusive filter for apheresis (leukapheresis). *Lab on a Chip*, 6:83–89, 2006.

[84] M. Yamada, M. Nakashima, and M. Seki. Pinched Flow Fractionation: Continuous Size Separation of Particles Utilizing a Laminar Flow Profile in a Pinched Microchannel. *Analytical Chemistry*, 76:5465–5471, 2004.

[85] J. Takagi, M. Yamada, M. Yasuda, and M. Seki. Continuous particle separation in a microchannel having asymmetrically arranged multiple branches. *Lab on a Chip*, 5:778–784, 2005.

[86] Y. Sai, M. Yamada, M. Yasuda, and M. Seki. Continuous separation of particles using a microfluidic device equipped with flow rate control valves. *Journal of Chromatography A*, 1127:214–220, 2006.

[87] H. Maenaka, M. Yamada, M. Yasuda, and M. Seki. Continuous and Size-Dependent Sorting of Emulsion Droplets Using Hydrodynamics in Pinched Microchannels. *Langmuir*, 24:4405–4410, 2008.

[88] A. Jain and J. D. Posner. Particle Dispersion and Separation Resolution of Pinched Flow Fractionation. *Analytical Chemistry*, 80(5):1641, 2008.

[89] K. B. Andersen, S. Levinsen, W. E. Svendsen, and F. Okkels. A generalized theoretical model for "continuous particle separation in a microchannel having asymetrically arranged multiple branches. *Lab on a Chip*, 9:1638–1639, 2009.

[90] C. Yi, Q. Zhang, C. W. Li, J. Yang, J. Zhao, and M. Yang. Optical and electrochemical detection techniques for cell-based microfluidic systems. *Analytical and Bioanalytical Chemistry*, 384:1259–1268, 2006.

[91] S. Götz and U. Karst. Recent development in optical methods for microchip separation. *Analytical and Bioanalytical Chemistry*, 387:183–192, 2007.

[92] K. L. Adams, M. Puchades, and A. G. Ewing. In Vitro Electrochemistry of Biological Systems. *Annual Review of Analytical Chemistry*, 1:329–355, 2008.

[93] M. Franko. Thermal Lens Spectroscopy Detection in Flow Injection Analysis and Separation Techniques. *Applied Spectroscopy Review*, 43:358–388, 2008.

[94] P. J. Viskari and J. P. Landers. Unconventional detection methods for microfluidic devices. *Electrophoresis*, 27:1797–1810, 2006.

[95] J. Fritz. Cantilever biosensors. *Lab on a Chip*, 133:855–863, 2008.

[96] D. Brennan, J. Justice, B. Corbett, T. McCarthy, and P. Galvin. Emerging optofluidic technologies for point-of-care genetic analysis systems: a review. *Analytical and Bioanalytical Chemistry*, 395:621–636, 2009.

[97] R. Bashir. Micromechanical cantilever as an ultrasensitive pH microsensor. *Applied Physics Letters*, 81(16):3091–3093, 2002.

[98] S. Kohale, S. M. Molina, B. L. Weeks, R. Khare, and L. J. Hope-Weeks. Monitoring the Formation of Self-Assembled Monolayers of Alkanedithiols Using a Micromechanical Cantilever Sensor. *Langmuir*, 23:1258–1263, 2007.

[99] J. Fritz, M. K. Baller, H. P. Lang, H. Rothuizen, P. Vettiger, E. Meyer, H.-J. Güntherodt, Ch. Gerber, and J. K. Gimzewski. Translating Biomolecular Recognition into Nanomechanics. *Science*, 288:316–318, 2000.

[100] R. Marie, J. Thaysen, and C. B. V. Christensen. D.

[101] A. Gupta, D. Akin, and R. Bashir. Detection of bacterial cells and antibodies using surface micromachined thin silicon cantilever resonators. *Journal of Vacuum Science Technology B*, 2004.

[102] M. B. Christiansen, J. M. Lopacinska, M. H. Jakobsen, N. A. Mortensen, M. Dufva, and A. Kristensen. Photonic polymer crystal dye lasers as Optofluidic Cell Sensors. *Optics Express*, 17(4):106347, 2009.

[103] C. Y. Chao, W. Fung, and L. J. Gou. Polymer microring resonator for biochemical sensing applications. *IEEE Journal of selected topics in quantum electronics*, 12(1):134–142, 2006.

[104] C.-Y. Liu, J. Rick, T.-C. Chou, H.-H. Lee, and G.-B. Lee. Integrated microfluidic system for electrochemical sensing of urinary proteins. *Biomedical Microdevices*, 11:201–211, 2009.

[105] A. A. Dawoud, T. Kawaguchi, Y. Markushin, M. D. Porter, and R. Jankowiak. Separation of catecholamines and dopamine-derived DNA adduct using a microfluidic device with electrochemical detection. *Sensors ans Actuators B*, 120:42–50, 2006.

[106] S. Kwakye, V. N. Goral, and A. J. Baeumner. Electrochemical microfluidic biosensor for nucleic acid detection with integrated minipotentiostat. *Biosensors and Bioelectronics*, 21:2217–2223, 2006.

[107] J. R. Webster, M. A. Burns, D. T. Burke, and C. H. Mastrangelo. Monolithic Capillary Electrophoresis Device with Integrated Fluorescence Detector. *Analytical Chemistry*, 73(1622-1626), 2001.

[108] Y.-C. Tsung, M. Zhang, C. T. Lin, K. Kurabayashi, and S. J. Skerlos. PDMS-based optofluidic micro flow cytometer with two-color, multi-angle fluorescence detection capability using pin photodiodes. *Sensors and Actuators B*, 98:356–367, 2004.

[109] M. L. Chabinyc, D. T. Chiu, J. C. McDonald, A. D. Stroock, J. F. Christian, A. M. Karger, and G. M. Whitesides. An Integrated Fluorescence Detection System in Poly(dimethylsiloxane) for Microfluidic Application. *Analytical Chemistry*, 73:4491–4498, 2001.

[110] N. J. Petersen, K. B. Mogensen, and J. P. Kutter. Performance of an in-plane detection cell with integrated waveguides for UV/Vis absorbance measurements on microfluidic separation devices. *Electrophoresis*, 23(3528-3536), 2002.

[111] R. De Palma, G. Reekmanns, C. Liu, R. Wirix-Speetjens, W. Laureyn, O. Nilsson, and L. Lagae. Magnetic Bead Sensing Platform for Detection of Proteins. *Analytical Chemistry*, 79:8669–8677, 2007.

[112] J. Loureiro, C. Fermon, M. Pannetier-Lecoeur, G. Arrias, R. Ferreira, S. Cardoso, and P. P. Freitas. Magnetoresistive Detection of Magnetis Beads Flowing at High Speed in Microfluidic Channels. *IEEE Transactions on Magnetics*, 45(10):4873–4876, 2009.

[113] M. Yamauchi, M. Tokeshi, J. Yamaguchi, T. Fukazawa, A. Hattori, A. Hibara, and T. Kitamori. Minituarized thermal lens and fluorescence detection system for microchemical chips. *Journal of Chromatography A*, 1106:89–93, 2006.

[114] A. Smirnova, K. Mwatari, A. Hibara, M. A. Proskurnin, and Kitamori. Micromultiphase laminar flows for the extraction and detection of carbaryl derivatives. *Analytica Chimica Acta*, 558:69–74, 2006.

[115] E. Tamaki, K. Sato, M. Tokeshi, K. Sato, M. Aihara, and T. Kitamori. Single-Cell Analysis by a Scanning Thermal Lens Microscope with a Microchip: Direct Monitoring of Cytochrome C Distribution during Apoptosis. *Analytical Chemistry*, 74:1560–1564, 2002.

[116] X. Heng, D. Erickson, L. R. Baugh, Z. Yaqoob, P. W. Sternberg, D. Psaltis, and C. Yang. Optofluidic microscopy - a method for implementing a high resolution optical microscope on a chip. *Lab on a Chip*, 6:1274–1276, 2006.

[117] X. Cui, L. M. Lee, X. Heng, W. Zhong, P. W. Sternberg, D. Psaltis, and C. Yang. Lensless high-resolution on-chip optofluidic microscopes for Caenorhabditis elegans and cell imaging. *Proceedings of the National Academic of Science*, 105:10670–10675, 2008.

[118] X. Heng, E. Hsiao, D. Psaltis, and C. Yang. An optical tweezer actuated, nanoaperture-grid based Optofluidic Microscope implementation method. *Optics Express*, 15:16367–16375, 2007.

[119] C. Ihee, M. Lorenc, T. K. Kim, Q. Y. Kong, M. Cammarata, J. H. Lee, S. Bratos, and M. Wullf. Ultrafast X-ray Diffraction of Transient Molecular Structures in Solutions. *Science*, 309:1223–1226, 2005.

[120] M. Christensen, K. Haldrup, K. Bechgaard, R. Feidenhans'l, Q. Kong, M. Cammarata, M. L. Russo, M. Wulff, N. Harrit, and M. M. Nielsen. Time-Resolved X-ray Scattering of an Electronically Excited State in Solution. Structure of the $^3A_{2u}$ State of Tetrakis-μ-Pyrophosphitodiplatinate(ii). *Journal of the American Chemical Society*, 131:502–508, 2009.

[121] M. Cammarata, M. Levantino, F. Schotte, P. A. Anfinrud, F. Ewald, J. Choi, A. Cupane, M. Wulff, and H. Ihee. Tracking the structural dynamics of proteins in solution using time-resolved wide-angle X-ray scattering. *Nature Methods*, 5(10):881–886, 2008.

[122] D. J. Thiel, P. Livins, E. A. Stern, and A. Lewis. Microsecond-resolved XAFS of the triplet excited state of $PT_2(P_2O_5H_2)^{4-}{}_4$. *Nature*, 362(40-43), 1993.

[123] M. Saes, F. van Mourik, W. Gawelda, M. Kaiser, M. Chergui, C. Bressler, D. Grolimund, R. Abela, T. E. Glover, P. A. Heimann, R. W. Schoenlein, S. L. Johnson, A. M. Lindenberg, and R. W. Falcone. A setup for ultrafast time-resolved x-ray absorption spectroscopy. *Review of Scientific Instruments*, 75(1):24–30, 2004.

[124] V.-T. Pham, W. Gawelda, Y. Zaushitsyn, M. Kaiser, D. Grolimund, S. L. Johnson, R. Abela, C. Bressler, and M. Chergui. Observation of the Solvent Shell Reorganization around Photoexcited Atomic Solutes by Picosecond X-ray Absorption Spectroscopy. *Journal of the American Chemical Society*, 129(1530-1531), 2007.

[125] B. Winter, E. F. Aziz, N. Ottosson, M. Faubel, N. Kosugi, and I. V. Hertel. Electron Dynamics in Charge-Transfer-to-Solvent States of Aqueous Chloride Revealed by Cl^- 2p Resonant Auger-Electron Spectroscopy. *Journal of the American Chemical Society*, 130(7130-7138), 2008.

[126] U. Weierstall, R. B. Doak, J. C. H. Spence, D. Starodub, D. Shapiro, P. Kennedy, J. Warner, G. G. Hembree, P. Fromme, and H. N. Chapman. Droplet stream for serial crystallography of proteins. *Experimental Fluids*, 44:675–689, 2008.

[127] A. L. Vig and A. Kristensen. Separation enhancement in pinched flow fractionation. *Applied Physics Letters*, 93:203507, 2008.

[128] A. V. Larsen, L. Poulsen, H. Birgens, M. Dufva, and A. Kristensen. Pinched flow fractionation devices for detection of single nucleotide polymorphisms. *Lab on a Chip*, 8:818–821, 2008.

[129] H. Bruus. *Theoretical microfluidics*. Oxford University Press Inc, 2008.

[130] Comsol. http://www.comsol.com/. August 12 2008.

[131] Wikipedia. http://en.wikipedia.org/wiki/laminar. November 4 2009.

[132] R. L. Yapici, R. L. Powell, and R. J. Phillips. Particle migration and suspension structure in steady state and oscillatory plane Poiseuille flow. *Physics of Fluids*, 21:053302, 2009.

[133] D. Di Carlo, J. F. Edd, K. J. Humphry, H. A. Stone, and M. Toner. Particle Segregation and Dynamics in Confined Flows. *Physics Review Letters*, 102:094503, 2009.

[134] Thermo Scientific. http://www.thermo.com/ethermo/cma/pdfs/articles/articlesfile_52060.pdf. August 10 2009.

[135] S. Y. Chou, P. R. Krausss, and J. Rentrom. Imprint of sub-25 nm vias and trenches in polymer. *Applied Physics Letters*, 67:3114–3116, 1995.

[136] M. Madou. *Fundamentals of Microfabrication*. CRC Press, 1997.

[137] J. D. Plummer, M. D. Deal, and P. B. Griffin. *Silicon VLSI Technology - Fundamentals, Practice and Modeling*. Printice Hall, Inc., 2000.

[138] S. D. Senturia. *Microsystem Design*. Springer Science + Buisness Madia, Inc., 2001.

[139] H. S. Nalwa, editor. *Handbook of Thin Film Materials*. Academic Press, 2002.

[140] 16th European Conference on Mask Technology for Integrated Circuits and Microcomponents, editors. *Mask fabrication by nanimprint lithography using anti-sticking layers*, volume 3996. Proceeding SPIE, 2000.

[141] M. Beck, M. Graczyk, I. Maximov, E.-L. Sarwe, T. G. I. Ling, M. Kiel, and L. Montelius. Improving stamps for 10 nm level wafer scale nanoimprint lithopraphy. *Microelectronic engineering*, 61-62:441–448, 2002.

[142] P. Silberzan, L. Léger, D. Ausserré, and J. J. Benattar. Silanation of Silica Surfaces. A New Method of Constructing Pure or Mixed Monolayers. *Langmuir*, 7:1647–1651, 1991.

[143] F. Laermer and S. Schlip. Robert bosch gmbh. page 5501893, US pat.

[144] D. Nilsson, S. Balslev, and S. Kristensen. A microfluidic dye laser fabricated by nanoimprint lithography in a highly transparent and chemically resistant cyclo-olefin copolymer (COC). *Journal of Micromechanics and Microengineering*, 15:296–300, 2005.

[145] A. V. Larsen. Deterministic Bio Separation Devices. M. Sc. Thesis, DTU Nanotech Department of Micro and Nanotechnology, 2006.

[146] Topas Advanced Polymers. http://www.topas.com/topas_brochure_english.pdf. November 20 2009.

[147] G. Khanarian and H. Celanese. Optical properties of cyclic olifin copolymers. *Optical Engineering*, 40(6):1024–1029, 2001.

[148] T. Nielsen, D. Nilsson, F. Bundgaard, P. Shi, P. Szabo, O. Geschke, and A. Kristensen. Nanoimprint lithography in the cyclic olefin copolymer, Topas, a highly ultraviolet-transparent and chemically resistant thermoplast. *Journal of Vacuum Science Technology B*, 13:814–818, 2004.

[149] *Rheological characterisation and tuning of polymers for nanoimprint lithography*, number Poster P-456. 34th International Conference on Micro- and Nano-Engineering, MNE-2008, 2008.

[150] C. M. Sotomayor Torres, editor. *Alternative Lithography: Unleashing the Potentials of Nanotechnology*. Kluwer Academic Publisher, 2003.

[151] R. H. Pedersen. Nanoimprint lithography and nanophotonics. Ph.d. thesis, DTU Nanotech Department of Micro and Nanotechnology, 2009.

[152] Cognoscens. http://www.cognoscens.com. November 21 2009.

[153] B. Bilenberg, M. Hansen, D. Johansen, V. Özkapici, C. Jeppesen, P. Szabo, I. M. Obieta, O. Arroyo, J. O. Tegenfeldt, and A. Kristensen. Topas based lab-on-a-chip microsystems fabricated by thermal nanoimprint lithography. *Journal of Vacuum Science Technology B*, 23(6):2944–2949, 2005.

[154] T. Mäkelä, P. Majander, J. Ahopelto, and V. Lambertini. Continuous Double-Sided Roll-to-Roll Imprinting in of Polymer Film. *Japanese Journal of Applied Physics*, 47(5142-5144), 2008.

[155] H. Kipphan. *Handbook of Print Media*. Springer, 2001.

[156] N. J. Kaihovirta, D. Tobjörk, T. Mäkelä, and R. Österbacka. Low-Voltage Organic Transistors Fabricated using Reverse Gravure Coating on Prepatterned Substrates. *Advanched Engineering Materials*, 10:640–643, 2008.

[157] A. C. Syvanen. Accessing Genetic Variation: Genotyping Single Nucleotide Polymorphisms. *Nature Review Genetics*, 2(12):930–942, 2001.

[158] Y. Wang, B. Vaidya, H. D. Farquar, W. Stryjewski, R. P. Hammer, R. L. McCarley, S. A. Soper, Y. W. Cheng, and F. Barany. Microarrays Assembled in Microfluidic Chips Fabricated from Poly(methyl methacrylate) for the Detection of Low-Abundant.

[159] Y. Liu and C. B. Rauch. DNA Probe Attachment on Plastic Surfaces and Microfluidic Hybridization Array Channel Devices with Sample Oscillation. *Analytical Biochemistry*, 317(1):76–84, 2003.

[160] H. Andersson, C. Jönsson, C. Moberg, and G. Stemme. Patterned self-assembled beads in silicon channels. *Electrophoresis*, 22(18):3876–3882, 2001.

[161] A. Russom, H. Ahmadian, H. Andersson, P. Nillson, and G. Stemme. Single-nucleotide polymorphism analysis by allele-specific extension of fluorescently labeled nucleotides in a microfluidic flow-through device. *Electrophoresis*, 24:158–161, 2003.

[162] M. F. Ali, R. Kirby, A. P. Goodey, M. Rodriguez, A. D. Ellington, D. P. Neikirk, and J. T. McDevitt. DNA Hybridization and Discrimination of Single-Nucleotide Mismatches Using Chip-Based Microbead Arrays. *Analytical Chemistry*, 75:4132–4739, 2003.

[163] E. Verpoorte. Beads and chips: new recipes for analysis. *Lab on a Chip*, 3:60N–68N, 2003.

[164] J. El-Ali, I. R. Perch-Nielsen, C. R. Poulsen, D. D. Bang, P. Telleman, and A. Wolff. Simulation and experimental validation of a SU-8 based PCR thermocycler chip with integrated heaters and temperature sensor. *Sensors and actuators A*, 110:3–10, 2004.

[165] J. Kim, D. Byun, M. G. Mauk, and H. H. Bau. A disposable, self-contained PCR chip. *Lab on a Chip*, 9(606-612), 2009.

[166] M. Mahalanabis, H. Al-Muayad, M. D. Kulinski, D. Altman, and C. M. Klapperich. Cell lysis and DNA extraction of gram-positive and gram-negative bacteria from whole blood in a disposable microfluidic chip. *Lab on a Chip*, 9(2811-2817), 2009.

[167] K. Smistrup, B. G. Kjeldsen, J. L. Reimers, M. Dufva, J. Petersen, and M. F. Hansen. On-chip magnetic bead microarray using hydrodynamic focusing in a passive magnetic separator. *Lab on a Chip*, 5(11):1315–9, 2005.

[168] Bang Laboratories. http://www.bangslabs.com/products/bangs/pdf/pds/pds%20714.pdf. Januar 21 2008.

[169] J. Petersen, L. Poulsen, S. Petronis, H. Birgens, and M. Dufva. Use of a multi-thermal washer for DNA microarrays simplifies probe design and gives robust genotyping assays. *Nucleic Acids Research*, 36:e10, 2007.

[170] K. J. Luebke, R. P. Balog, and H. R. Garner. Prioritized selection of oligodeoxyribonucleotide probes for efficient hybridization to rna transcripts. *Nucleic Acids Research*, 31(2):750–758, 2003.

[171] B. Armstrong, M. Stewart, and A. Mazumder. Suspension Arrays for high Throughput, Multiplexed Single Nucleotide Polymorphism Genotyping. *Cytometry*, 40:102–108, 2000.

[172] S. A. Dunbar. Application of Luminex xMAP technology for rapid, high-throughput multiplexed nucleic acid detection. *Clinica Chimica Acta*, 363:71–82, 2006.

[173] F. Persson, L. H. Thamdrup, M. B. L. Mikkelsen, S. E. Jaarlgaard, P. Skafte-Pedersen, H. Bruss, and A. Kristensen. Double thermal oxidation scheme for fabrication of SiO_2 nanochannel. *Nanotechnology*, 18:245301, 2007.

[174] G. L. Kenausis, J. Vörös, D. L. Elbert, N. Huang, R. Hofer, L. Ruiz-Taylor, M. Textor, J. A. Hubbell, and N. D. Spencer. Poly(L-lysine)-g-Poly(ethylene glycol) Layers on Metal Oxide Surfaces: Attachment Mechanism and Effects of Polymer Architecture on Resistance to Protein Adsorption. *Journal of Physics Chemistry B*, 104:3298–3309, 2000.

[175] R. Marie, J. P. Beech, J. Vörös, J. O. Tegenfeldt, and F. Höök. Use of PLL-g-PEG in Micro-Fluidic Devices for Localizing Selective and Specific Protein Binding. *Langmuir*, 22:10103–10108, 2006.

[176] R. Marie, A. B. Dahlin, J. O. Tegenfeldt, and F. Höök. Generic surface modification strategy for sensing applications based on Au/SiO_2 nanostructures. *Biointerphases*, 2(1):49–55, 2007.

[177] A. L. Vig, K. Haldrup, N. Enevoldsen, A. H. Thilsted, J. Eriksen, A. Kristensen, R. Feidenhans'l, and M. M. Nielsen. Windowless microfluidic platform based on capillary burst valves for high intensity x-ray measurements. *Review of Scientific Instruments*, 80:115114, 2009.

[178] P. Wochner, C. Gutt, T. Autenrieth, T. Demmer, V. Bugaev, A. D. Ortiz, A. Duri, F. Zontone, G. Grübel, and H. Dosch. X-ray cross corelation analysis uncovers hidden local symetries in disordered matter. *Proceedings of the National Academy of Science*, 106(28):11511–11514, 2009.

[179] A. Aghababyan et al. *XFEL The European X-ray Free-Electron Laser Technical Design Report*. HelmHoltz Gemeinschaft, 2006.

[180] D. C. Duffy, H. L. Gills, J. Lin, N. F. Sheppard, and G. J. Kellog. Microfabricated Centrifugal Microfluidic Systems: Characterization and Multiple Enzymatic Assays. *Analytical Chemistry*, 71:4669–4678, 1999.

[181] S. Lai, S. Wang, J. Luo, L. J. Lee, S.-T. Yang, and J. Madou. Design of a Compact Disk-like Microfluidic Platform for Enzyme-linked Immunosorbent Assay. *Analytical Chemistry*, 76:1832–1837, 2004.

[182] *Centrifuge-Based Fluidic Platforms*, volume 92. Proc IEEE, 2004.

[183] H. Cho, H.-Y. Kim, J. Y. Kang, and T. S. Kim. How the capillary burst microvalve works. *Journal of Colloid Interface Science*, 306:319–385, 2007.

[184] R. D. Johnson, I. H. A. Badr, G. Barret, S. Lai, Y. Lu, M. J. Madou, and L. G. Bachas. Development of a Fully Integrated Analysis System for Ions Based on Ion-Selective Optodes and Centrifugal Microfluidics. *Analytical Chemistry*, 73:3940–3946, 2001.

[185] L. G. Puckett, E. Dikici, S. Lai, M. Madou, L. G. Bachas, and S. Daunert. Investigation into the Applicability of the Centrifugal Microfluidics Platform for the Development of Protein-Ligand Binding Assays Incorporating Enhanced Green Fluorescent Protein as a Fluorescent Reporter. *Analytical Chemistry*, 76:7263–7268, 2004.

[186] L. Pollack, M. W. Tate, N. C. Darnton, J. B. Knight, S. M. Gruner, W. A. Eaton, and R. H. Austin. Compactness of the denatured state of a fast-folding protein measured by submillisecond small-angle x-ray scattering. *Proceedings of the National Academy of Science*, 96:10115–10117, 1999.

[187] M. Cammarata, L. Eybert, F. Ewald, W. Reichenbach, M. Wulff, P. Anfinrud, F. Schotte, A. Plech, Q. Kong, M. Lorenc, B. Lindenau, J. Räbiger, and S. Polachowski. Chopper system for time resolved experiments with synchrotron radiation. *Review of Scientific Instruments*, 80:015101, 2009.

[188] K. Haldrup, M. Christensen, M. Cammarata, Q. Kong, M. Wulff, S. O. Mariager, K. Bechgaard, R. Feidenhans'l, N. Harrit, and M. M. Nielsen. Structural Tracking of a Bimolecular Reaction in Solution by Time-Resolved X-Ray Scattering. *Angewande Chemie Internatiol Edition*, 48:4180–4184, 2009.

Appendix A

List of publications

During the Ph.D. project I was married. In this occasion I changed my name from Asger Vig Larsen to Asger Laurberg Vig, which is why both names occur in the list.

A.1 Journal articles

A. L. Vig, T. Mäkelä, P. Majander, V. Lambertini, J. Ahopelto and A. Kristensen: *Roll-to-roll fabricated lab-on-a-chip devices*, Submitted to Journal of Micromechanics and Microengineering November 2009

A. L. Vig, R. Marie, E. Jensen and A. Kristensen: *Optofluidic microscope with 3 dimensional resolution*, Optics Express, Vol. 18, Issue 5, 4158-4169 (2010)

A. Greve, S. Keller, **A. L. Vig**, A. Kristensen, D. Larsson, K. Yvind, J. Hvam, M. Cerruti, A. Majumdar and A. Boisen: *Thermoplastic microcantilevers fabricated by nanoimprint lithography*, Journal of Micromechanical Microengineering, Vol. 20, 015009 (2010)

A. L. Vig, K. Haldrup, N. Enevoldsen, A. H. Thilsted, J. Eriksen, A. Kristensen, R. Feidenhans'l and M. M. Nielsen: *Windowless microfluidic platform base on capillary burst valves for high intensity x-ray measurements*, Review of Scientific Instruments, Vol. 80, 115114 (2009)

A. L. Vig and A. Kristensen: *Separation Enhancement in pinched flow fractionation*, Applied Physics Letters, Vol. 93, 203507 (2008)

A. V. Larsen, L. Poulsen, H. Birgens, M. Dufva and A. Kristensen: *Pinched Flow Fractionation Devices for Detection of Single Nucleotide Polymorphisms*, Lab On a Chip, Vol. 8, 818-821 (2008)

A.2 International conference contributions

A. Greve, S. Dohn, S. Keller, **A. L. Vig**, A. Kristensen, C. H. Nielsen, N. B. Larsen and A. Boisen: *Wafer Scale Coating Of Polymer Cantilever Fabricated By Nanoim-*

print Lithography, IEEE MEMS (*Poster*), Hong Kong, China (2010)

A. L. Vig, J. H. Rasmussen, P. B. Muller, R. Marie, E. Jensen, R. T. Nielsen and A. Kristensen: *Optofluidic Microscope in Microfluidic Separation*, FFF (*Poster*), Patras, Greece (2009)

R. Pedersen, L. Thamdrup, **A. L. Vig**, A. Kristensen and D. A. Mendels, *Origins of Stamp Bending in Nano-Imprint Lithography*, EIPBN (*Poster*), Marco Island, USA (2009)

R. H. Pedersen, L.H. Thamdrup, **A. V. Larsen**, A. Kristensen and D.-A. Mendels, *Quantitative Strategies to Handle Stamp Bending in NIL*, NNT (*Oral*), Kyoto, Japan (2008)

A. V. Larsen, T. Makela, P. Majander, J. Ahopelto and A. Kristensen, *Roll-to-Roll Thermal Nanoimprinted Microfluidic Separation Devices*, NNT (*Oral*), Kyoto, Japan (2008)

T. Makela, T. Haatainen, P. Majander, J. Ahopelto, **A. V. Larsen** and A. Kristensen: C*Continuous roll-to-roll method to produce fluidics channels on plastic web*, MNE (*Poster*), Athens, Greece (2008)

A. V. Larsen, T. Makela, P. Majander, J. Ahopelto and A. Kristensen: *Roll-to-Roll thermal nanoimprinted microfluidic separation devices based on pinched flow fractionation*, MNE (*Oral*), Athens, Greece (2008)

R. H. Pedersen, L. H. Thamdrup, **A. V. Larsen**, A. Kristensen and D.-A. Mendels: *Quantitative strategies to handle stamp bending in NIL*, MNE (*Poster*), Athens, Greece (2008)

A. V. Larsen, L. Poulsen, H. Birgens, M. Dufva and A. Kristensen: *Genotyping single nucleotide polymorphisms based on pinched flow fractionation*, MNE (*Poster*), Copenhagen, Denmark (2007)

A.3 Patent applications

R. Marie, **A. L. Vig**, M. Christiansen and A. Kristensen, US Patent Application No. 61/247616 and EP Patent Application No. 09171928.6, filed October 1st, 2009

R. Marie, **A. L. Vig** and A. Kristensen, Patent application in progress